

RtEstim: Time-varying reproduction number estimation with trend filtering

Jiapeng Liu^{1*}, Zhenglun Cai², Paul Gustafson¹, Daniel J. McDonald¹

1 Department of Statistics, The University of British Columbia, Vancouver, British Columbia, Canada

2 Centre for Health Evaluation and Outcome Sciences, The University of British Columbia, Vancouver, British Columbia, Canada

* jiapeng.liu@stat.ubc.ca

Abstract

To understand the transmissibility and spread of infectious diseases, epidemiologists turn to estimates of the instantaneous reproduction number. While many estimation approaches exist, their utility may be limited. Challenges of surveillance data collection, model assumptions that are unverifiable with data alone, and computationally inefficient frameworks are critical limitations for many existing approaches. We propose a discrete spline-based approach called **RtEstim** that solves a convex optimization problem—Poisson trend filtering—using the proximal Newton method. It produces a locally adaptive estimator for instantaneous reproduction number estimation with heterogeneous smoothness. **RtEstim** remains accurate even under some process misspecifications and is computationally efficient, even for large-scale data. The implementation is easily accessible in a lightweight R package **rtestim**.

Author summary

Instantaneous reproduction number estimation presents many challenges due to data collection, modelling assumptions, and computational burden. Our motivation is to develop a model that produces accurate estimates, is robust to model misspecification,

is straightforward to use, and is computationally efficient, even for large counts and long time periods. We propose a convex optimization model with an ℓ_1 trend filtering penalty. It couples accurate estimation of the instantaneous reproduction number with desired smoothness. We solve the optimization using the proximal Newton method, which converges rapidly and is numerically stable. Our software, conveniently available in the R package `RtEstim`, can produce estimates in seconds for incidence sequences with hundreds of observations. These estimates are produced for a sequence of tuning parameters and can be selected using a built-in cross validation procedure.

1 Introduction

The effective reproduction number is defined to be the expected number of secondary infections produced by a primary infection where some part of the population is no longer susceptible. The effective reproduction number is a key quantity for understanding infectious disease dynamics including the potential size of an outbreak and the required stringency of control measures [1, 2]. The instantaneous reproduction number is a type of effective reproduction number that tracks the number of secondary infections at time t relative to all preceding primary infections. This contrasts with the case reproduction number at t which indexes a primary infection at time t , tracking the infectiousness of the cohort [3]. Tracking the time series of the effective reproduction number quantity is useful for understanding whether or not future infections are likely to increase or decrease from the current state [4]. Our focus is on the instantaneous reproduction number at time t , which we will denote $\mathcal{R}(t)$. Practically, as long as $\mathcal{R}(t) < 1$, infections will decline gradually, eventually resulting in a disease-free equilibrium, whereas when $\mathcal{R}(t) > 1$, infections will continue to increase, resulting in endemic equilibrium. While $\mathcal{R}(t)$ is fundamentally a continuous time quantity, it can be related to data only at discrete points in time $t = 1, \dots, n$. This sequence of instantaneous reproduction numbers over time is not observable, but, nonetheless, is easily interpretable and describes the course of an epidemic. Therefore, a number of procedures exist to estimate \mathcal{R}_t from different types of observed incidence data such as cases, deaths, or hospitalizations, while relying on various domain-specific assumptions, e.g., [5–8]. Importantly, accurate estimation of instantaneous reproduction numbers

relies heavily on the quality of the available data, and, due to the limitations of data collection, such as underreporting and lack of standardization, estimation methodologies rely on various assumptions to compensate. Because model assumptions may not be easily verifiable from data alone, it is also critical for any estimation procedure to be robust to model misspecification.

Many existing approaches for instantaneous reproduction number estimation are Bayesian: they estimate the posterior distribution of \mathcal{R}_t conditional on the observations. One of the first such approaches is the software **EpiEstim** [9], described by Cori et al. [10]. This method is prospective, focusing on the instantaneous reproduction number, and using only observations available up to time t in order to estimate \mathcal{R}_t for each $i = 1, \dots, t$. An advantage of **EpiEstim** is its straightforward statistical model: new incidence data follows the Poisson distribution conditional on past incidence combined with the conjugate gamma prior distribution for \mathcal{R}_t with fixed hyperparameters. Additionally, the serial interval distribution, the distribution of the period between onsets of primary and secondary infections in a population, is fixed and known. For this reason, **EpiEstim** requires little domain expertise for use, and it is computationally fast. Thompson et al. [11] modified this method to distinguish imported cases from local transmission and simultaneously estimate the serial interval distribution. Nash et al. [12] further extended **EpiEstim** by using “reconstructed” daily incidence data to handle irregularly spaced observations.

Recently, Abbott et al. [13] proposed a Bayesian latent variable framework, **EpiNow2** [14], which leverages incident cases, deaths or other available streams simultaneously along with allowing additional delay distributions (incubation period and onset to reporting delays) in modelling. Lison et al. [15] proposed an extension that handles missing data by imputation followed by a truncation adjustment. These modifications are intended to increase accuracy at the most recent (but most uncertain) timepoints, to aid policymakers. Parag et al. [16] also proposed a Bayesian approach, **EpiFilter**, based on the (discretized) Kalman filter and smoother. **EpiFilter** also estimates the posterior of \mathcal{R}_t given using a Markov model for \mathcal{R}_t and Poisson distributed incident cases. Compared to **EpiEstim**, however, **EpiFilter** estimates \mathcal{R}_t retrospectively using all available incidence data both before and after time t , with the goal of being more robust in low-incidence periods. Gressani et al. [17] proposed a

Bayesian P-splines approach, EpiLPS, that assumes negative binomial distributed
55 observations, allowing for overdispersion in the observed incidence. Trevisin et al. [18]
56 also proposed a Bayesian model estimated with particle filtering to incorporate spatial
57 structures. Bayesian approaches estimate the posterior distribution of the instantaneous
58 reproduction numbers and possess the advantage that credible intervals may be easily
59 computed. They also can incorporate prior knowledge on parameters. Another potential
60 advantage is that a relatively large prior on the mean of \mathcal{R}_t can be used to guard
61 against erroneously concluding that an epidemic is shrinking [11]. However, a downside
62 is that the induced bias can persist for long periods of time. Bayesian approaches that
63 do not use conjugate priors, or that incorporate multilevel modelling, can be
64 computationally expensive, especially when observed data sequences are long or
65 hierarchical structures are complex, e.g., [13].
66

There are also frequentist approaches for \mathcal{R}_t estimation. Abry et al. [19] proposed
67 regularizing the smoothness of \mathcal{R}_t through penalized regression with second-order
68 temporal regularization, additional spatial penalties, and with Poisson loss. Pascal et
69 al. [20] extended this procedure by adding a penalty on outliers. Pircalabelu et al. [21]
70 proposed a spline-based model relying on the assumption of exponential-family
71 distributed incidence. Ho et al. [22] estimates \mathcal{R}_t while monitoring the time-varying
72 level of overdispersion. There are other spline-based approaches such as [23, 24],
73 autoregressive models with random effects [25] that are robust to low incidence, and
74 generalized autoregressive moving average models [26] that are robust to measurement
75 errors in incidence data.
76

We propose an instantaneous reproduction number estimator, called **RtEstim** that
77 requires only incidence data. Our model makes the conditional Poisson assumption,
78 similar to much of the prior work described above, but is empirically more robust to
79 misspecification. This estimator is defined by a convex optimization problem with
80 Poisson loss and ℓ_1 penalty on the temporal evolution of $\log(\mathcal{R}_t)$ to impose smoothness
81 over time. As a result, **RtEstim** generates discrete splines, and the estimated curves (on
82 the logarithmic scale) appear to be piecewise polynomials of an order selected by the
83 user. Importantly, the estimates are locally adaptive, meaning that different time ranges
84 may possess heterogeneous smoothness. Because we penalize the logarithm of \mathcal{R}_t , we
85 naturally accommodate the positivity requirement, in contrast to related
86

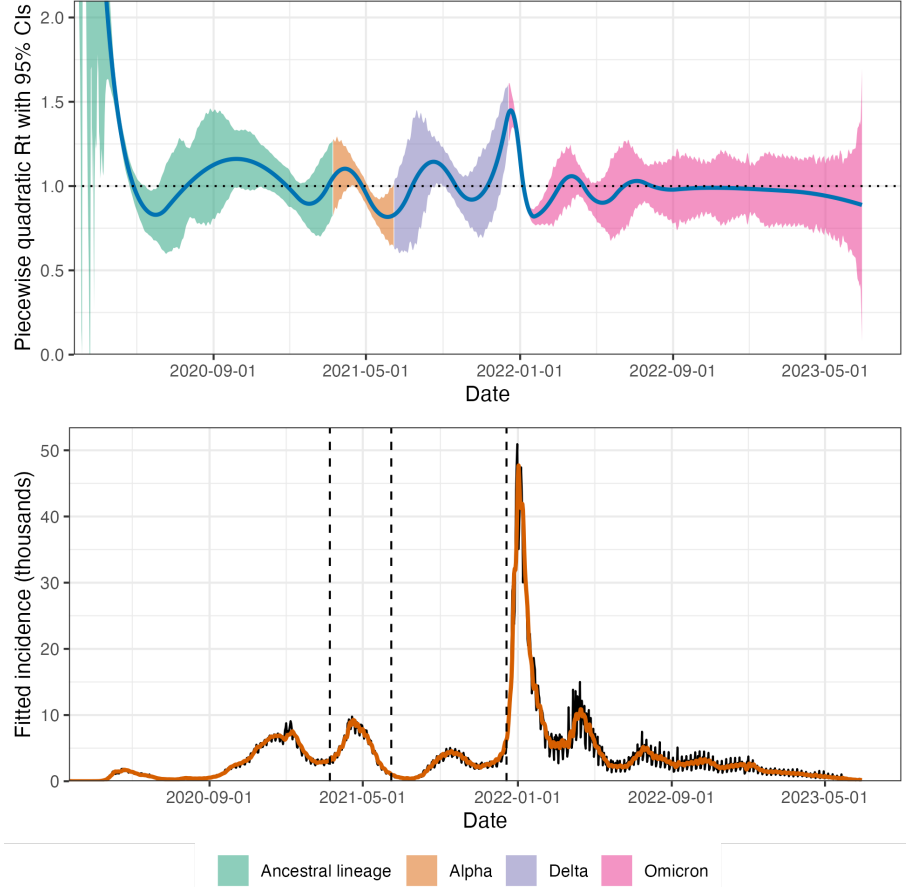


Fig 1. A demonstration of instantaneous reproduction number estimation by RtEstim and the corresponding predicted incident cases for the Covid-19 epidemic in Canada during the period from January 23, 2020 to June 28, 2023. In the top panel, the blue curve is the estimated piecewise quadratic R_t and the colorful ribbon is the corresponding 95% confidence band. The colors represent the variants whose serial interval distributions are used to estimate R_t . The dominant circulating variants are based on a multinomial logistic regression model with variant probabilities from [28]. The time-varying serial interval distributions are based on results from [29]. In the bottom panel, the black curve is the observed Covid-19 daily confirmed cases, and the orange curve on top of it is the predicted incident cases corresponding to the estimated R_t . The three vertical dashed lines represent the beginning of a new dominant variant.

methods [19, 20], can handle large or small incidence measurements, and are automatically (reasonably) robust to outliers without additional constraints (a feature of the ℓ_1 penalty). A small illustration using three years of Covid-19 case data in Canada [27] is shown in Fig 1, where we use a time-varying serial interval distribution.

While our approach is straightforward and requires little domain knowledge for implementation, we also implement a number of refinements:

- the algorithm solves over a range of tuning parameters simultaneously, using

- warm starts to speed up subsequent solutions; 94
- cross-validation is built in (and used in all analyses below) to automatically select 95 tuning parameters;
 - parametric (gamma), non-parametric (any discretized delay), and time-varying 97 delay distributions are allowed; 98
 - irregularly spaced incidence data are easily accommodated; 99
 - approximate confidence intervals for \mathcal{R}_t and the observed incidence are available; 100
 - the estimated log \mathcal{R}_t can be mathematically described as an element of a 101 well-known function space depending on user choice [38]. 102

We use a proximal Newton method to solve the convex optimization problem along with 103 warm starts to produce estimates efficiently, typically in a matter of seconds, even for 104 long sequences of data. In a number of simulation experiments, we show empirically 105 that our approach is more accurate than existing methods at estimating the true 106 instantaneous reproduction numbers and robust to some degrees of misspecification of 107 incidence distribution, serial interval distribution, and the order of graphical curvature. 108

The manuscript proceeds as follows. We first introduce the methodology of `RtEstim` 109 including the renewal equation and the development of Poisson trend filtering estimator. 110 We explain how this method could be interpreted from the Bayesian perspective, 111 connecting it to previous work in this context. We provide illustrative experiments 112 comparing our estimator to other Bayesian alternatives. We then apply our `RtEstim` on 113 the Covid-19 pandemic in Canada and the 1918 influenza pandemic in the United 114 States. Finally, we conclude with a discussion of the advantages and limitations of our 115 approach and describe some practical considerations for instantaneous reproduction 116 number estimation. 117

2 Methods

2.1 Renewal model for incidence data

The instantaneous reproduction number $\mathcal{R}(t)$ is defined to be the expected number of 120 secondary infections at time t produced by a primary infection sometime in the past. To 121 make this precise, denote the number of new infections at time t as $y(t)$. Then the total 122

primary infectiousness can be written as $\eta(t) := \int_0^\infty p(t, i)y(t - i)di$, where $p(t, i)$ is the
 123 probability that a new secondary infection at time t is the result of a primary infection
 124 that occurred i time units in the past. The instantaneous reproduction number is then
 125 given as the value that equates
 126

$$\mathbb{E}[y(t) | y(j), j < t] = \mathcal{R}(t)\eta(t) = \mathcal{R}(t) \int_0^\infty p(t, i)y(t - i)di, \quad (1)$$

otherwise known as the renewal equation. The period between primary and secondary
 127 infections is exactly the generation time of the disease, but given real data, observed at
 128 discrete times (say, daily), this delay distribution must be discretized into contiguous
 129 time intervals, say, $(0, 1], (1, 2], \dots$, resulting in the sequence $\{p_{t,i}\}_{i=0}^\infty$ corresponding to
 130 observations y_t for each t and yields the discretized version of Eq (1),
 131

$$\mathbb{E}[y_t | y_1, \dots, y_{t-1}] = \mathcal{R}_t\eta_t = \mathcal{R}_t \sum_{i=1}^{\infty} p_{t,i}y_{t-i}. \quad (2)$$

Many approaches to estimating \mathcal{R}_t rely on Eq (2) as motivation for their procedures,
 132 among them, EpiEstim [10] and EpiFilter [16].
 133

In most cases, it is safe to assume that infectiousness disappears beyond τ
 134 timepoints ($p(t, i) = 0$ for $i > \tau$), resulting in the truncated integral of the generation
 135 interval distribution $\int_0^\tau p(t, i)di = 1$ for each t . Generation time, however, is usually
 136 unobservable and tricky to estimate, so common practice is to approximate it by the
 137 serial interval: the period between the symptom onsets of primary and secondary
 138 infections. If the infectiousness profile after symptom onset is independent of the
 139 incubation period (the period from the time of infection to the time of symptom onset),
 140 then this approximation is justifiable: the serial interval distribution and the generation
 141 interval distribution share the same mean. However, other properties may not be
 142 similarly shared, and, in general, the generation interval distribution is a convolution of
 143 the serial interval distribution with the distribution of the difference between
 144 independent draws from the delay distribution from infection to symptom onset. See,
 145 for example, [3] for a fuller discussion of the dangers of this approximation. Nonetheless,
 146 treating these as interchangeable is common [10, 30], and doing otherwise is beyond the
 147 scope of this work. We will allow the delay distribution to be either constant over
 148

time—the probability $p(i)$ depends only on the gap between primary and secondary infections and not on the time t when the secondary infection occurs—or to be time-varying: $p(t, i)$ also depends on the time of the secondary infection. For our methods, we assume that the serial interval can be accurately estimated from auxiliary data (say by contact tracing, or previous epidemics) and we take it as fixed, as is common in existing studies, [10, 19, 20].

The renewal equation in Eq (2) relates observable data streams (incident cases) occurring at different timepoints to the instantaneous reproduction number given the serial interval. The fact that it depends only on the observed incident counts makes it reasonable to estimate \mathcal{R}_t . However, data collection idiosyncrasies can obscure this relationship. Diagnostic testing targets symptomatic individuals, omitting asymptomatic primary infections which can lead to future secondary infections. Testing practices, availability, and uptake can vary across space and time [31, 32]. Finally, incident cases as reported to public health are subject to delays due to laboratory confirmation, test turnaround times, and eventual submission to public health [33]. For these reasons, reported cases are lagging indicators of the course of the pandemic. Furthermore, they do not represent the actual number of new infections that occur on a given day, as indicated by exposure to the pathogen. The assumptions described above (homogeneous mixing, similar susceptibility and social behaviours, etc.) are therefore consequential. That said, Eq (2) also provides some comfort about deviations from these assumptions. Under certain conditions, failing to account for the reporting behaviours will minimally impact the accuracy of any \mathcal{R}_t estimator that is based on Eq (2). We discuss three types of deviation here. First, if y_t is scaled by a constant a describing the reporting ratio, then, because it appears on both sides of Eq (2), \mathcal{R}_t will be unchanged. Second, if such a scaling a_t varies in time, as long as it varies slowly relative to p_i —that is, if $a_t / \sum_{i=1}^t a_i p_i \approx 1$ —then \mathcal{R}_t can still be estimated well from reported incidence data. Finally, if a sudden change in reporting ratio occurs at time t_1 , it would only result in large errors in \mathcal{R}_t at times near t_1 (where the size of this neighbourhood is determined indirectly by the effective support of $\{p_{t_1,i}\}$). On the other hand, time-varying reporting delays would be much more detrimental [34, 35].

2.2 Poisson trend filtering estimator

179

We use the daily confirmed incident cases y_t on day t to estimate the observed infectious cases under the model that y_t , given previous incident cases y_{t-1}, \dots, y_1 and a constant serial interval distribution, follows a Poisson distribution with mean Λ_t . That is,

$$y_t \mid y_1, \dots, y_{t-1} \sim \text{Poisson}(\Lambda_t), \text{ where } \Lambda_t = \mathcal{R}_t \sum_{i=1}^{t-1} p_i y_{t-i} = \mathcal{R}_t \eta_t. \quad (3)$$

We will write p_i as constant in time for simplicity, although this is not required. Given a history of n confirmed incident counts $\mathbf{y} = (y_1, \dots, y_n)^\top$, our goal is to estimate \mathcal{R}_t for each $t = 1, \dots, n$. A natural approach is to maximize the likelihood, producing the maximum likelihood estimator (MLE):

$$\begin{aligned} \hat{\mathcal{R}} &= \underset{\mathcal{R} \in \mathbb{R}_+^n}{\operatorname{argmax}} \mathbb{P}(\mathcal{R} \mid \mathbf{y}, \mathbf{p}) = \underset{\mathcal{R} \in \mathbb{R}_+^n}{\operatorname{argmax}} \prod_{t=1, \dots, n} \frac{(\mathcal{R}_t \eta_t)^{y_t} \exp\{-\mathcal{R}_t \eta_t\}}{y_t!} \\ &= \underset{\mathcal{R} \in \mathbb{R}_+^n}{\operatorname{argmin}} \sum_{t=1}^n \mathcal{R}_t \eta_t - y_t \log(\mathcal{R}_t \eta_t). \end{aligned} \quad (4)$$

This optimization problem, however, is easily seen to yield a one-to-one correspondence between the observation and the estimated instantaneous reproduction number, i.e., $\hat{\mathcal{R}}_t = y_t / \eta_t$, so that the estimated sequence $\hat{\mathcal{R}}$ will have no significant smoothness.

The MLE is an unbiased estimator of the true parameter \mathcal{R}_t , but unfortunately has high variance: changes in y_t result in proportional changes in $\hat{\mathcal{R}}_t$. To avoid this behaviour, and to match the intuition that $\mathcal{R}_t \approx \mathcal{R}_{t-1}$, we advocate enforcing smoothness of the instantaneous reproduction numbers. This constraint will decrease the estimation variance, and hopefully lead to more accurate estimation of \mathcal{R} , as long as the smoothness assumption is reasonable. Smoothness assumptions are common (see e.g., [3, 16]), but the type of smoothness assumption is critical. Cori et al. [10] imposes smoothness indirectly by estimating \mathcal{R}_t with moving windows of past observations. The Kalman filter procedure of [16] would enforce ℓ_2 -smoothness ($\int_0^n (\hat{\mathcal{R}}''(t))^2 dt < C$ for some constant C), although the computational implementation results in $\hat{\mathcal{R}}$ taking values over a discrete grid. Pascal et al. [20] produces piecewise linear $\hat{\mathcal{R}}_t$, which turns out to be closely related to a special case of our methodology. Smoother estimated curves will provide high-level information about the entire epidemic, obscuring small

local changes in $\mathcal{R}(t)$, but may also remove the ability to detect large sudden changes,
such as those resulting from lockdowns or other major containment policies.

To enforce smoothness of $\widehat{\mathcal{R}}_t$, we add a trend filtering penalty [36–39] to Eq (5).
Because $\mathcal{R}_t > 0$, we explicitly penalize the divided differences (discrete derivatives) of
neighbouring values of $\log(\mathcal{R}_t)$. Let $\theta := \log(\mathcal{R}) \in \mathbb{R}^n$, so that $\Lambda_t = \eta_t \exp(\theta_t)$, and
 $\log(\eta_t \mathcal{R}_t) = \log(\eta_t) + \theta_t$. For evenly spaced incidence data, we write our estimator as
the solution to the optimization problem

$$\widehat{\mathcal{R}} = \exp(\widehat{\theta}) \quad \text{where} \quad \widehat{\theta} = \underset{\theta \in \mathbb{R}^n}{\operatorname{argmin}} \eta^\top \exp(\theta) - \mathbf{y}^\top \theta + \lambda \|D^{(k+1)}\theta\|_1, \quad (5)$$

where $\exp(\cdot)$ applies elementwise and $\|\mathbf{a}\|_1 := \sum_{i=1}^n |a_i|$ is the ℓ_1 norm. Here,
 $D^{(k+1)} \in \mathbb{Z}^{(n-k-1) \times n}$ is the $(k+1)^{\text{th}}$ order divided difference matrix for any
 $k \in \{0, \dots, n-1\}$ with the convention that $D^{(0)} = \mathbf{0}_{n \times n}$. The divided difference matrix
for $k=0$, $D^{(1)} \in \{-1, 0, 1\}^{(n-1) \times n}$, is a sparse matrix with diagonal band of the form:

$$D^{(1)} = \begin{pmatrix} -1 & 1 & & & \\ & -1 & 1 & & \\ & & \ddots & \ddots & \\ & & & -1 & 1 \end{pmatrix}. \quad (6)$$

For $k \geq 1$, $D^{(k+1)}$ can be defined recursively as $D^{(k+1)} := D^{(1)}D^{(k)}$, where
 $D^{(1)} \in \{-1, 0, 1\}^{(n-k-1) \times (n-k)}$ has the form Eq (6) but with modified dimensions.

The tuning parameter (hyperparameter) λ balances data fidelity with desired
smoothness. When $\lambda = 0$, the problem in Eq (5) reduces to the MLE in Eq (4). Larger
tuning parameters privilege the regularization term and yield smoother estimates.
Finally, there exists λ_{\max} such that any $\lambda \geq \lambda_{\max}$ will result in $D^{(k+1)}\widehat{\theta} = 0$ and $\widehat{\theta}$ will
be the Kullback-Leibler projection of \mathbf{y} onto the null space of $D^{(k+1)}$ (see Section 2.3
for more details).

The solution to Eq (5) will result in piecewise polynomials, specifically called discrete
splines. For example, 0th-degree discrete splines are piecewise constant, 1st-degree
curves are piecewise linear, and 2nd-degree curves are piecewise quadratic. For $k \geq 1$,
 k^{th} -degree discrete splines are continuous and have continuous discrete differences up to
degree $k-1$ at the knots (i.e., changing points between segments). This penalty results

in more flexibility compared to the homogeneous smoothness that is created by the squared ℓ_2 norm. Using different orders of the divided differences results in estimated instantaneous reproduction numbers with different smoothness properties.

For unevenly spaced data, the spacing between neighbouring parameters varies with the time between observations, and thus, the divided differences must be adjusted by the times that the observations occur. Given observation times $\mathbf{x} = (x_1, \dots, x_n)^\top$, for $k \geq 1$, define a k^{th} -order diagonal matrix

$$X^{(k)} = \text{diag} \left(\frac{k}{x_{k+1} - x_1}, \frac{k}{x_{k+2} - x_2}, \dots, \frac{k}{x_n - x_{n-k}} \right). \quad (7)$$

Letting $D^{(\mathbf{x},1)} := D^{(1)}$, then for $k \geq 1$, the $(k+1)^{\text{th}}$ -order divided difference matrix for unevenly spaced data can be created recursively by $D^{(\mathbf{x},k+1)} := D^{(1)} X^{(k)} D^{(\mathbf{x},k)}$. No adjustment is required for $k = 0$.

Due to the penalty structure, this estimator is locally adaptive, meaning that it can potentially capture local changes such as the initiation of control measures, becoming more wiggly in regions that require it. In contrast, Abry et al. and Pascal et al. considered only the 2nd-order ($k = 2$) divided difference of \mathcal{R}_t rather than its logarithm [19, 20]. In comparison to their work, our estimator (i) allows for arbitrary degrees of temporal smoothness and (ii) avoids the potential numerical issues of penalizing/estimating positive real values. Nonetheless, as we will describe below, our procedure is computationally efficient for estimation over an entire sequence of hyperparameters λ and provides methods for choosing how smooth the final estimate should be.

2.3 Solving over a sequence of tuning parameters

We can solve the Poisson trend filtering estimator over an arbitrary sequence of λ that produces different levels of smoothness in the estimated curves. We consider a candidate set of M λ -values, $\boldsymbol{\lambda} = \{\lambda_m\}_{m=1}^M$, that is strictly decreasing.

Let $D := D^{(k+1)}$ for simplicity in the remainder of this section. As $\lambda \rightarrow \infty$, the penalty term $\lambda \|D\theta\|_1$ dominates the Poisson loss, so that minimizing Eq (5) is asymptotically equivalent to minimizing the penalty term, which results in $\|D\theta\|_1 = 0$. In this case, the divided differences of θ with order $k+1$ is always 0, and thus, θ must

lie in the null space of D , that is, $\theta \in \mathcal{N}(D)$. The same happens for any λ beyond this
255 threshold, so define λ_{\max} to be the smallest λ that produces $\theta \in \mathcal{N}(D)$. It turns out
256 that this value can be written explicitly as $\lambda_{\max} = \| (D^\dagger)^\top (\eta - y) \|_\infty$, where D^\dagger is the
257 (left) generalized inverse of D satisfying $D^\dagger D = I$ and $\|a\|_\infty := \max_i |a_i|$ is the infinity
258 norm. Explicitly, for any $\lambda \geq \lambda_{\max}$, the solution to Eq (5) will be identical to the
259 solution with λ_{\max} . Therefore, we use $\lambda_1 = \lambda_{\max}$ and choose the minimum λ_M to be
260 $r\lambda_{\max}$ for some $r \in (0, 1)$ (typically $r = 10^{-4}$). Given any $M \geq 3$, we generate a
261 sequence of λ values to be equally spaced on the log-scale between λ_1 and λ_M .
262

To compute the sequence of solutions efficiently, the model is estimated sequentially
263 by visiting each λ_m in order, from largest to smallest. The estimates produced for a
264 larger λ are used as the initial values (warm starts) for the next smaller λ . By solving
265 through the entire sequence of tuning parameters, we improve computational efficiency
266 and also enable one to trade between bias and variance, resulting in improved accuracy
267 relative to procedures using a single fixed tuning parameter.
268

2.4 Choosing a final λ

We estimate model accuracy over the candidate set through V -fold cross validation
270 (CV) to choose the best tuning parameter. Specifically, we divide \mathbf{y} (except the first and
271 last observations) roughly evenly and randomly into V folds, estimate \mathcal{R}_t for all λ
272 leaving one fold out, and then predict the held-out observations. Alternatively, one could
273 use regular splitting, assigning every v^{th} observation into the same fold. Note that our
274 approach is most closely related to non-parametric regression rather than time series
275 forecasting. That said, under some conditions, one can guarantee that V -fold remains
276 valid for risk estimation in time series. The sufficient conditions are quite strong, but the
277 guarantees are also stronger than would be required for model selection consistency [40].
278

Model accuracy can be measured by multiple metrics such as mean squared error
279 $\text{MSE}(\hat{y}, y) = n^{-1} \|\hat{y} - y\|_2^2$ or mean absolute error $\text{MAE}(\hat{y}, y) = n^{-1} \|\hat{y} - y\|_1$, but we
280 prefer to use the (average) deviance, to mimic the likelihood in Eq (4):
281

$D(y, \hat{y}) = n^{-1} \sum_{i=1}^n 2(y_i \log(y_i) - y_i \log(\hat{y}_i) - y_i + \hat{y}_i)$, with the convention that
282 $0 \log(0) = 0$. Note that for any V and any M , we will end up estimating the model
283 $(V + 1)M$ times rather than once.
284

2.5 Approximate confidence bands

285

We also provide empirical confidence bands of the estimators with approximate coverage. Consider the related estimator $\tilde{\mathcal{R}}_t$ defined as

$$\tilde{\mathcal{R}} = \exp(\tilde{\theta}) \quad \text{where} \quad \tilde{\theta} = \underset{\theta \in \mathbb{R}^n}{\operatorname{argmin}} \eta^\top \exp(\theta) - \mathbf{y}^\top \theta + \lambda \|D\theta\|_2^2. \quad (8)$$

Letting $\tilde{\mathbf{y}} = \eta \circ \tilde{\mathcal{R}}$ (where \circ denotes the elementwise product), it can be shown (for example, Theorem 2 in [41]) that an estimator for $\operatorname{Var}(\tilde{\mathbf{y}})$ is given by $(\operatorname{diag}(\tilde{\mathbf{y}}^{-2}) + \lambda D^\top D)^\dagger$. Finally, an application of the delta method shows that $\operatorname{Var}(\tilde{\mathbf{y}}_t)/\eta_t^2$ is an estimator for $\operatorname{Var}(\tilde{\mathcal{R}}_t)$ for each $t = 1, \dots, n$. We therefore use $(\operatorname{diag}(\hat{\mathbf{y}}^{-2}) + \lambda D^\top D)_t^\dagger/\eta_t^2$ as an estimator for $\operatorname{Var}(\hat{\mathcal{R}}_t)$. An approximate $(1 - \alpha)\%$ confidence interval then can be written as $\hat{\mathcal{R}}_t \pm s_t \times T_{\alpha/2, n-\text{df}}$, where s_t is the square-root of $\operatorname{Var}(\hat{\mathcal{R}}_t)$ for each $t = 1, \dots, n$ and df is the number of changepoints in $\hat{\theta}$ plus $k + 1$ [37]. An approximate confidence interval of $\hat{\mathbf{y}}$ can be computed similarly.

2.6 Bayesian perspective

296

Unlike many other methods for \mathcal{R}_t estimation, our approach is frequentist rather than Bayesian. Nonetheless, it has a corresponding Bayesian interpretation: as a state-space model with Poisson observational noise, autoregressive transition equation of degree $k \geq 0$, e.g., $\theta_{t+1} = 2\theta_t - \theta_{t-1} + \varepsilon_{t+1}$ for $k = 1$, and Laplace transition noise $\varepsilon_{t+1} \sim \text{Laplace}(0, 1/\lambda)$. Compared to **EpiFilter** [16], we share the same observational assumptions, but our approach has a different transition noise. **EpiFilter** estimates the posterior distribution of \mathcal{R}_t , and thus it can provide credible interval estimates as well. Our approach produces the maximum *a posteriori* estimate via an efficient convex optimization, obviating the need for MCMC sampling. But the associated confidence bands are created differently.

3 Results

307

Implementation of our approach is provided in the R package **rtestim**. All computational experiments are conducted on the Cedar cluster provided by the Digital Research Alliance of Canada with R 4.3.1. The R packages used for simulation and

real-data application are EpiEstim 2.2-4 [42], EpiLPS 1.2.0 [43], and rtestim
0.0.4. The R scripts for EpiFilter are used [44].

3.1 Synthetic experiments

3.1.1 Design for the synthetic data

We simulate four scenarios of the instantaneous reproduction number, intended to
mimic different epidemics. The first two scenarios are rapidly controlled by intervention,
where the $\mathcal{R}(t)$ consists of one discontinuity and two segments. Scenario 1 has constant
 $\mathcal{R}(t)$ before and after an intervention, while Scenario 2 grows exponentially, then decays.
The other two scenarios are more complicated, where more waves are involved. Scenario
3 has four linear segments with three discontinuities, which reflect the effect of an
intervention, resurgence to rapid transmission, and finally suppression of the epidemic.
Scenario 4 involves sinusoidal waves throughout the epidemic. The first three scenarios
and the last scenario are motivated by [16] and [17] respectively. We name the four
scenarios as (1) piecewise constant, (2) piecewise exponential, (3) piecewise linear, and
(4) periodic.

In all cases, the times of observation are regular, and epidemics are of length
 $n = 300$. Specifically, in Scenario 1, $\mathcal{R}_t = 2$ before $t = 120$ and 0.8. In Scenario 2, \mathcal{R}_t
increases and decreases exponentially with rates 0.01 before $t = 100$ and 0.005 after. In
Scenario 3, \mathcal{R}_t is piecewise linear with four discontinuous segments,

$$\begin{aligned} \mathcal{R}(t) = & \left(2.5 - \frac{0.5}{74} (t - 1) \right) \mathbf{1}_{[1,76)}(t) + \left(0.8 - \frac{0.2}{74} (t - 76) \right) \mathbf{1}_{[76,151)}(t) \\ & + \left(1.7 + \frac{0.3}{74} (t - 151) \right) \mathbf{1}_{[151,226)}(t) + \left(0.9 - \frac{0.4}{74} (t - 226) \right) \mathbf{1}_{[226,300]}(t), \end{aligned} \quad (9)$$

where $\mathbf{1}_A(t) = 1$, if $t \in A$, and $\mathbf{1}_A(t) = 0$ otherwise. In Scenario 4, \mathcal{R}_t is realization of
the continuous, periodic curve generated by the function

$$\mathcal{R}(t) = 0.2 \left((\sin(\pi t/12) + 1) + (2 \sin(5\pi t/12) + 2) + (3 \sin(5\pi t/6) + 3) \right), \quad (10)$$

evaluated at equally spaced points $t \in [0, 10]$. These \mathcal{R}_t scenarios are illustrated in Fig 2.
We compute the expected incidence Λ_t using the renewal equation, and generate the
incident infections from the Poisson distribution with mean $\mathbb{E}[y_t | y_s, s < t] = \Lambda_t$. To

verify the performance of our model under violations of the model's distributional
assumptions, we also generate incident cases using the negative binomial distribution
with dispersion parameter $\rho = 5$. Here, the negative binomial is parameterized such that
the mean is $\mathbb{E}[y_t | y_s, s < t] = \Lambda_t$ and the variance is $\text{Var}[y_t | y_s, s < t] = \Lambda_t(1 + \Lambda_t/\rho)$
(following, for example, [17]). Because $(1 + \Lambda_t/\rho) > 1$ for $0 \leq \rho < \infty$, this
parameterization results in overdispersion relative to the Poisson distribution, with
smaller values of ρ leading to greater overdispersion. For context on the observed
dispersion of these synthetic experiments, Figure A.2.1 in the Supplement displays the
ratio of the time-varying standard deviation to the mean.

We use serial interval (SI) distributions of measles (with mean 14.9 and standard
deviation 3.9) in Hagelloch, Germany in 1861 [45] and SARS (with mean 8.4 and
standard deviation 3.8) in Hong Kong in 2003 [46], inspired by [10], to generate
synthetic epidemics. We initialize all epidemics with $y_1 = 2$ cases and generate for
 $t = 2, \dots, 300$. The synthetic measles epidemics have smaller incident cases in general,
and the SARS epidemics have larger incidence. Essentially, the smaller mean of the
serial interval for SARS with a similar standard deviation leads to shorter expected
delays between onsets of primary and secondary infections, resulting in faster growth of
incidence within the same period of time. We also consider shorter flu epidemics with
50 timepoints with piecewise linear \mathcal{R}_t (Scenario 3) considering both incidence
distributional assumptions. The motivation is to compare our method and other
alternatives with EpiNow2 which takes much longer to compute for long epidemics
(nearly 2 hours to converge for a measles epidemic with 300 timepoints) than other
methods. Besides using the correct SI distributions to estimate \mathcal{R}_t , we also consider the
scenarios where the SI is misspecified. More details on experimental settings and results
for shorter epidemics and misspecification of SI distributions are given in Sections A.2.1
and A.3 in the supplementary document respectively.

For each problem setting (including SI distribution, an \mathcal{R}_t scenario, and an incidence
distribution), we generate 50 random samples, resulting in 800 total synthetic epidemics.
Example realizations for measles and SARS with each instantaneous reproduction
number scenario is displayed in Fig 2.

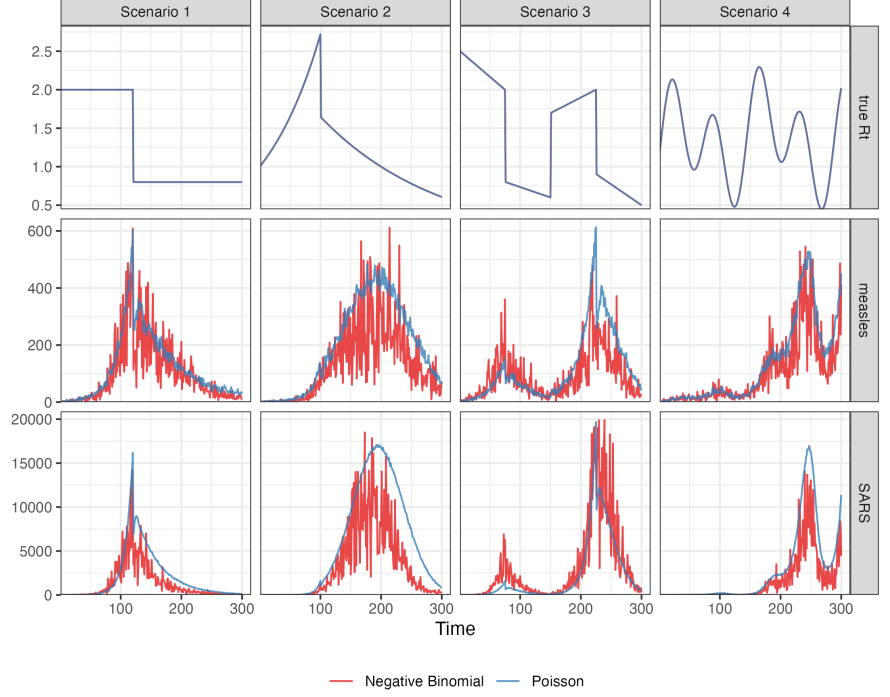


Fig 2. This figure displays example realizations for each \mathcal{R}_t setting. Top row: the instantaneous reproduction numbers. Middle row: synthetic measles incidence (Poisson in blue, negative binomial in red) incidence. Bottom row: synthetic SARS incidence. The 4 4 \mathcal{R}_t scenarios are shown in the columns.

3.1.2 Algorithmic choices

We compare **RtEstim** to **EpiEstim**, **EpiLPS**, and **EpiFilter**. **EpiEstim** estimates the posterior distribution of the instantaneous reproduction number given a Gamma prior and Poisson distributed observations over a trailing window, under the assumption that the instantaneous reproduction number is constant during that window. A larger window averages out more fluctuations, leading to smoother estimates, whereas a shorter window is more responsive to sudden spikes or declines. We used weekly sliding and monthly windows, however, since neither considerably outperforms the other across all scenarios, we defer the monthly results to the supplementary document. **EpiLPS** is another Bayesian approach that estimates P-splines based on the Laplace approximation to the conditional posterior with negative binomial likelihood. It should more easily handle the negative binomial scenarios as it matches the data generating process. **EpiFilter** uses a particle filtering procedure on a discrete grid of possible \mathcal{R}_t values.

In each setting, we apply **RtEstim** with four choices of $k = 0, 1, 2, 3$ resulting in

different shapes of the estimated \mathcal{R}_t —piecewise constant, piecewise linear, piecewise quadratic, and piecewise cubic—respectively. We use 10-fold cross validation (CV) to choose the parameter λ that minimizes out-of-sample prediction risk from a candidate set of size 50, i.e., $\boldsymbol{\lambda} = \{\lambda_1, \dots, \lambda_{50}\}$, for long epidemics, and 5-fold CV for short epidemics (results for this case are deferred to Sections A.3.2 and A.4.2 in the Supplement). We select the tuning parameter that gives the lowest deviance between the estimated incidence and the held-out samples averaged over all folds.

For the alternative methods, we generally use the set of tuning parameters that were applied to their own experimental settings. We consider both weekly and monthly sliding windows in **EpiEstim**. **EpiLPS** uses 40 P -spline basis functions and optimizes using the Nelder-Mead procedure. For **EpiFilter**, we specify a grid with 2000 cells, use 0.1 for the size of the diffusion noise, and use the “smoothed” \mathcal{R}_t (conditional on all data) as the final estimate.

For the \mathcal{R}_t estimation using all models for each problem, we use the same serial interval distribution, that was used to generate synthetic data. Taking different hyperparameters into consideration, we solve each problem using 8 methods including **EpiEstim** with weekly or monthly sliding windows, **EpiLPS**, **EpiFilter**, and **RtEstim** with piecewise constant, linear, quadratic, or cubic curves. We have not made any effort to tune these (and other choices) more carefully.

For **RtEstim**, The choice of k explicitly controls the function space to which the solution will belong [38], providing the analyst with a mathematical understanding of the result. When faced with real data, the choice of k for **RtEstim** should be done either (1) based on the analyst’s preference for the resulting structure (e.g., “I want to find large jumps, so $k = 0$ ”) or (2) in a data-driven manner, as a component of the estimation process. Our software enables both cases: the second case can be implemented by simply fitting different k and choosing the set k, λ that has smallest CV score. Thus, all necessary choices can be accomplished based solely on the data, a departure from existing methods in that we both allow this choice and provide simple data-driven methods to accomplish it.

3.1.3 Accuracy measurement

408

To measure estimation accuracy, we compare the estimated $\widehat{\mathcal{R}}$ to the true \mathcal{R} using the Kullback-Leibler (KL) divergence. KL is useful in this context for a few reasons. First, it correctly handles the non-negativity constraint on \mathcal{R} . Second, KL matches the negative log-likelihood used in Eq (4). Third, it captures the curved geometry of the probability spaces implied by the Poisson distribution accurately. And fourth, as in the equation below, it has a convenient functional form depending only on \mathcal{R} and η . For the Poisson distribution the KL divergence is defined as

409

410

411

412

413

414

415

$$D_{KL}(\mathcal{R} \parallel \widehat{\mathcal{R}}) = \sum_{t=1}^n \eta_t \left(\mathcal{R}_t \log \left(\frac{\mathcal{R}_t}{\widehat{\mathcal{R}}_t} \right) + \widehat{\mathcal{R}}_t - \mathcal{R}_t \right). \quad (11)$$

We use the average KL divergence: $\overline{D}_{KL}(\mathcal{R} \parallel \widehat{\mathcal{R}}) := D_{KL}(\mathcal{R} \parallel \widehat{\mathcal{R}})/n$. Details on the derivation of Eq (11) is provided in Section A.1 of the Supplement. KL divergence is more appropriate for measuring accuracy because it connects directly to the Poisson likelihood used to generate the data, whereas standard measures like the mean-squared error correspond to Gaussian likelihood. Using Poisson likelihood has the effect of increasing the relative cost of mistakes when Λ_t is small.

416

417

418

419

420

421

422

423

424

425

426

427

428

To fairly compare across methods, we omit the first week of data (and estimates) for a few reasons. Estimates from **EpiEstim** are not available until $t = 8$ when using a weekly sliding window. Additionally, some procedures purposely impose strong priors that \mathcal{R}_1 is much larger than 1 to avoid over confidently asserting that an epidemic is under control. The effect of these priors will persist for days or weeks, but one would hope for accurate estimates as early in the outbreak as possible. Other details of the experimental settings are deferred to the supplementary document.

429

3.2 Results for synthetic data

429

RtEstim generally performs at least as well as the other competitors in the experimental study. Fig 3 and Fig 4 visualize the KL divergence across the seven methods. For low incidence in measles epidemics, **RtEstim** is the most accurate for all \mathcal{R}_t scenarios given both Poisson and negative binomial incidence. The best performance of **RtEstim** has the lowest median and has low or no overlap with other methods. For

430

431

432

433

434

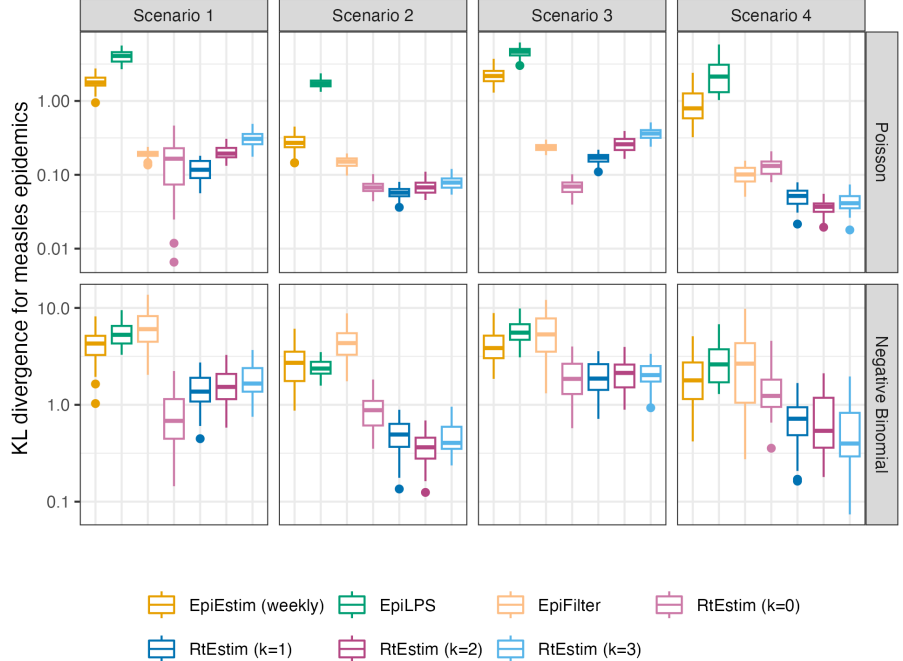


Fig 3. Boxplot of mean KL divergence between $\hat{\mathcal{R}}_t$ and the true \mathcal{R}_t across 50 synthetic measles epidemics for each approach given Poisson incidence (top panels) and negative binomial incidence (bottom panels). The average excludes the first week in all settings, since **EpiEstim** with a weekly sliding window does not provide estimates for the first week. Outliers beyond $1.5 \times \text{IQR}$ of each box are excluded for the sake of comparison with full range of the y -axis deferred to Figure A.3.1 in the Supplement.

Scenario 1, **EpiFilter** is a competitive alternative given Poisson incidence, which has similar median to the best performance of our **RtEstim** and with a small variation, however for negative binomial incidence, **EpiFilter** loses its advantage and has the largest medians of any method in Scenarios 1 and 2. The large incidence in SARS epidemics is more difficult for all methods. For Poisson incidence, results are similar to the previous setting. However, for negative binomial incidence, **EpiLPS** performs at least as well if not better than **RtEstim**, especially in Scenarios 2 and 4. Nonetheless, **RtEstim** is largely similar, with simulation uncertainty suggesting comparable performance. We will examine a single realization of each experiment to investigate these global conclusions in more detail.

Fig 5 shows one realization for the estimated instantaneous reproduction number under the Poisson generative model in measles synthetic epidemics for all four scenarios. An expanded visualization with each estimated \mathcal{R}_t curve displayed in a separate panel is provided in Figure A.6.1 in the Supplement. Ignoring the start of the epidemics, all

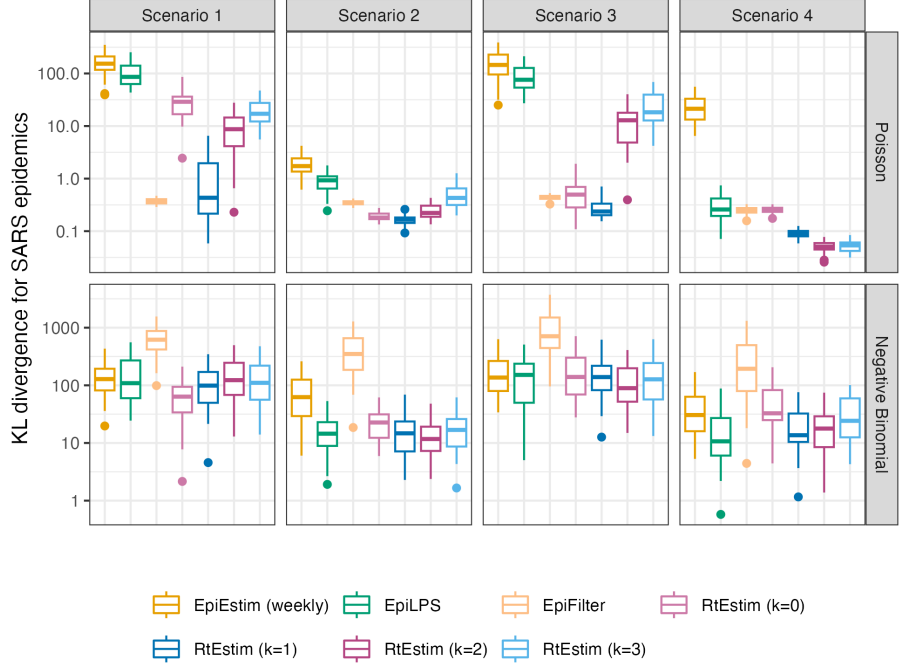


Fig 4. Boxplot of mean KL divergence between $\hat{\mathcal{R}}_t$ and the true \mathcal{R}_t across 50 synthetic SARS epidemics for each approach given Poisson incidence (top panels) and negative binomial incidence (bottom panels). The average excludes the first week in all settings, since **EpiEstim** with a weekly sliding window does not provide estimates for the first week. Outliers beyond $1.5 \times \text{IQR}$ of each box are excluded for the sake of comparison with full range of the y -axis deferred to Figure A.3.1 in the Supplement.

methods look accurate and recover the underlying curves well, except **EpiEstim** with monthly sliding windows, where the trajectories are shifted to the right. Compared to **EpiEstim** and **EpiLPS**, which have rather severe difficulties at the beginning of the period, **RtEstim** and **EpiFilter** estimates are more accurate without suffering from the initialization problem. The edge problem in **EpiEstim** and **EpiLPS** may be due to their priors, with the bias persisting for many days. **RtEstim** can also have edge problem though, it is less severe for smaller k . Besides the edge problem, **EpiEstim** (especially, with the monthly sliding window) and **EpiLPS** produce “smooth” estimated curves that are continuous at the changepoints in Scenarios 1–3, resulting in large errors for a long period. Since the piecewise constant **RtEstim** estimator does not force any smoothness in \mathcal{R}_t , it easily captures the sharp change and nearly overlaps with the true values in Scenario 1. **RtEstim** with higher k can work nearly as well due to the ℓ_1 penalty’s ability to allow heterogenous smoothness. However, similar to other methods, **RtEstim** has some difficulty with the first few timepoints, especially in the periodic scenario,

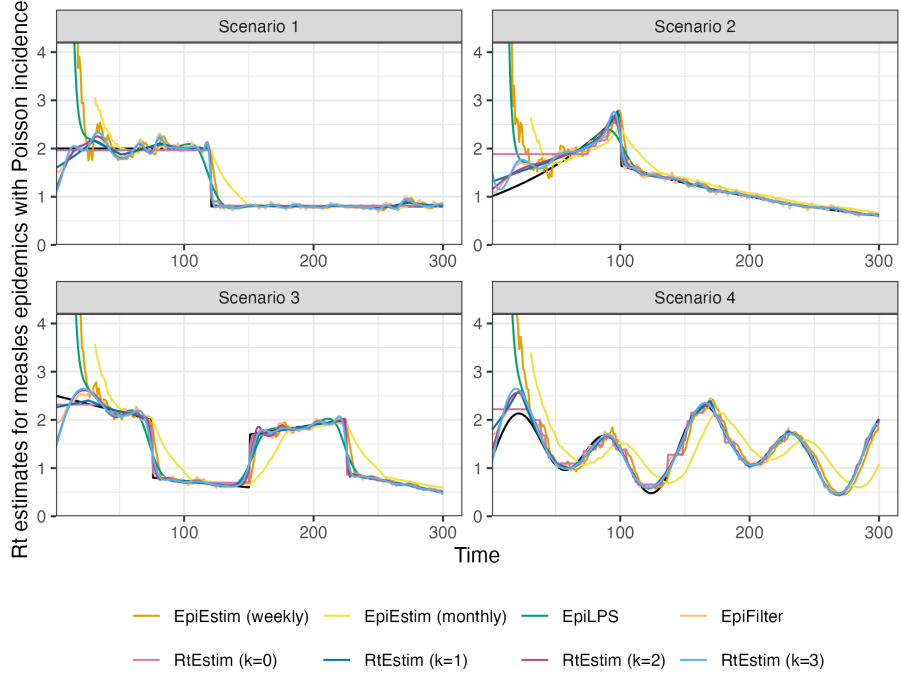


Fig 5. \mathcal{R}_t estimates for realizations of a measles epidemic with Poisson observations. An expanded visualization with each estimated \mathcal{R}_t curve displayed in a separate panel is provided in Figure A.6.1 in the Supplement.

where all methods fail to capture the first peak with an accurately. **EpiFilter** recovers the \mathcal{R}_t curves well in general, but tends to be more wiggly than other methods.

Fig 6 is similar to **Fig 5** but shows estimated \mathcal{R}_t given negative binomial incidence in SARS epidemics for each setting. An expanded visualization with each estimated \mathcal{R}_t curve displayed in a separate panel is provided in Figure A.6.4 in the Supplement. Compared to the **Fig 5**, all methods perform worse overall due to two main reasons: larger incidence and overdispersed data. All methods are worse at the start of the epidemics. **EpiFilter** is dramatically wiggly. Our **RtEstim** estimates are close to the best performance in the first three \mathcal{R}_t scenarios, though they have significant difficulties in the periodic scenario.

Finally, it is important to provide a brief comparison of the running times of all three models across the 8 experimental settings. We find that almost all models across all experiments complete within 10 seconds. **RtEstim** generally takes the longest, due to a relatively large number of estimates—50 values of λ and 10 folds of cross validation require 550 estimates—while other models run only a single time for a fixed setting of hyperparameters per experiment.

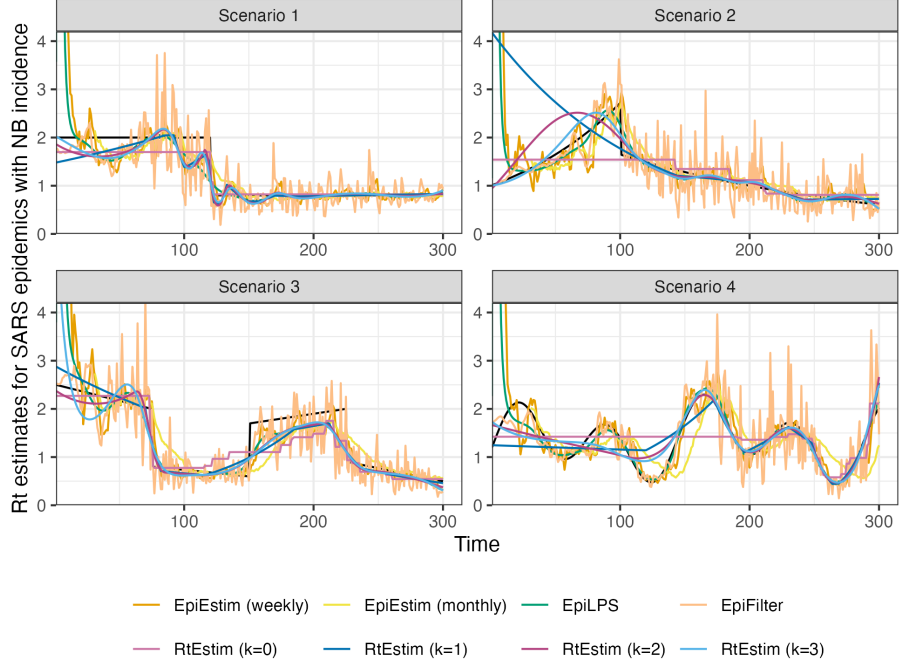


Fig 6. \mathcal{R}_t estimates for realizations of a SARS epidemic with negative binomial observations. An expanded visualization with each estimated \mathcal{R}_t curve displayed in a separate panel is provided in Figure A.6.4 in the Supplement.

3.3 Real-data results: Covid-19 incident cases in Canada

We return to the data for Covid-19 confirmed incident cases in Canada examined in Section 1. In this section, we use the weighted average of the serial interval distributions for the four dominant variants (shown in Fig 1) for the purposes of comparison with other methods, none of which allow time-varying delays. The estimates for RtEstim are displayed in Fig 7 while the estimates of all competitors are deferred to Figures A.8.1 and A.8.2 in the Supplement.

Considering $k = 1, 2$ and 3 , $\widehat{\mathcal{R}}_t$ for Covid-19 in Canada is always less than 2 except at the very early stage, which means that one distinct infected individual on average infects less than two other individuals in the population. Examining three different settings for k , the temporal evolution of $\widehat{\mathcal{R}}$ (across all regularization levels λ) are similar near the highest peak around the end of 2021 before dropping shortly thereafter. Throughout the estimated curves, the peaks and troughs of the instantaneous reproduction numbers precede the growth and decay cycles of confirmed cases, as expected. We also visualize 95% confidence bands for the point estimates with λ chosen

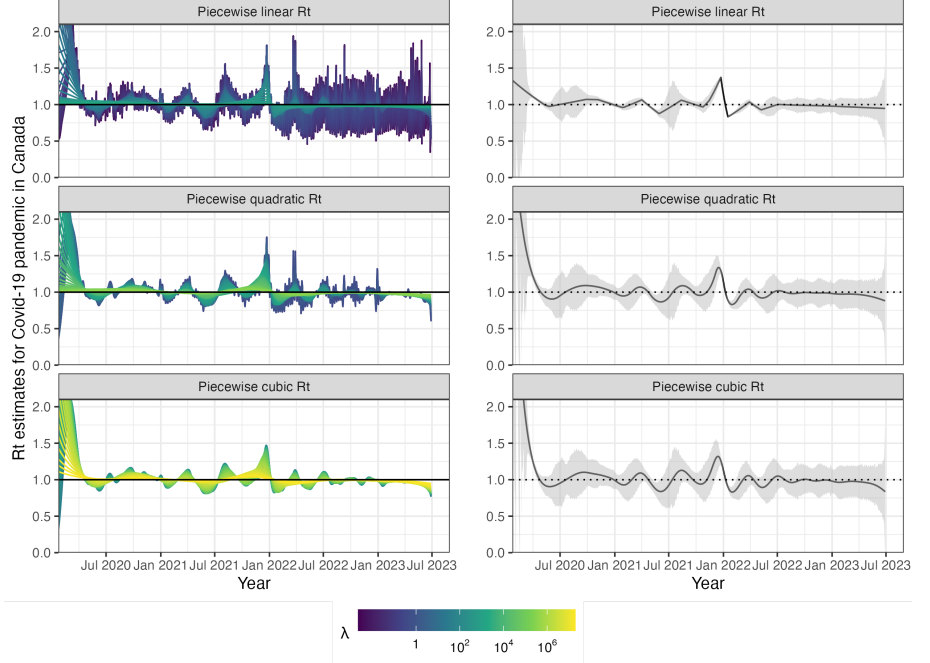


Fig 7. Estimated instantaneous reproduction number based on Covid-19 daily confirmed incident cases between January 23rd, 2020 and June 28th, 2023 in Canada. The left panels show estimates corresponding to 50 tuning parameters. The right panels show the CV-tuned estimate along with approximate 95% confidence bands. The top, middle and bottom panels show the estimated \mathcal{R}_t using the Poisson trend filtering in Eq (5) with degrees $k = 1, 2, 3$ respectively. All estimates use a constant serial interval distribution, which is the weighted sum of probabilities of the 4 dominant variants used in Fig 1.

by minimizing cross-validated KL divergence in Fig 7.

The estimated instantaneous reproduction numbers are relatively unstable before April, 2022. The highest peak coincides with the emergence and global spread of the Omicron variant. The estimated instantaneous reproduction numbers fall below 1 during a few time periods, where the most obvious troughs are roughly from April 2021 to July 2021 and from January, 2022 to April 2022. The first trough coincides with the introduction of Covid-19 vaccines in Canada. The second trough, shortly after the largest peak may be due to variety of factors resulting in the depletion of the susceptible population such as increased self-isolation in response to media coverage of the peak or immunity incurred via recent infection. Since April 2022, the estimated instantaneous reproduction number has remained relatively stable (fluctuating around one) corresponding to low reported cases, though reporting behaviours also changed significantly since the Omicron wave.

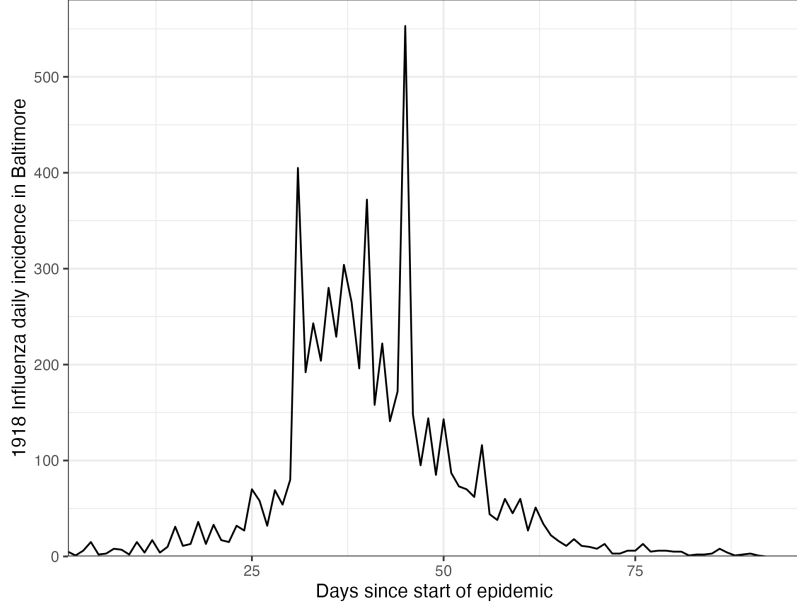


Fig 8. Daily incident influenza cases in Baltimore, Maryland between September and November 1918.

3.4 Real-data results: influenza in Baltimore, Maryland, 1918

We also apply `RtEstim` to daily reported influenza cases in Baltimore, Maryland occurring during the world-wide pandemic of 1918 from September to November [47]. The data, shown in Fig 8, is included in the `EpiEstim` R package, along with the serial interval distribution. The 1918 influenza outbreak, caused by the H1N1 influenza A virus, was unprecedentedly deadly with case fatality rate over 2.5%, infecting almost one-third of the population across the world [48]. The CV-tuned piecewise cubic estimates in Fig 9 better capture the growth at the beginning of the pandemic in Fig 8. The estimated \mathcal{R}_t curve suggests that the transmissibility of the pandemic grew rapidly over the first 30 days before declining below one after 50 days. However, it also suggests an increase in infectiousness toward the end of the period. With this data, it is difficult to determine if there is a second wave or a steady decline ahead. The CV-tuned piecewise constant and linear estimates in Fig 9 both suggest a steady decline. This conclusion is supported by the fact that incident cases decline to zero at the end of the period, matching \mathcal{R}_t estimates in [10], which are all lower than one. Results from alternative software is deferred to Figures A.8.3 and A.8.4 in the Supplement.

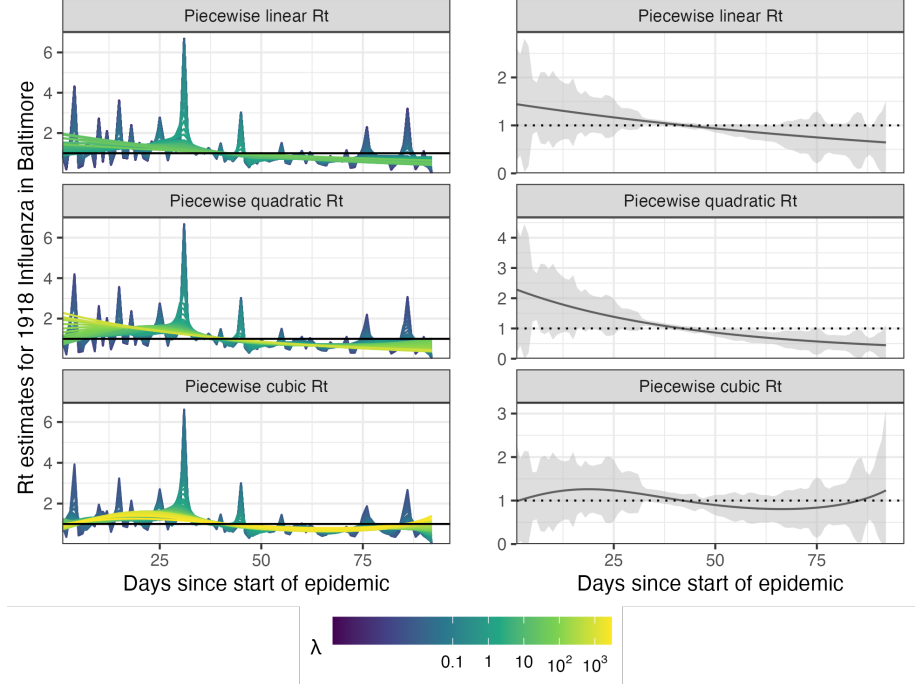


Fig 9. Estimated instantaneous reproduction numbers for influenza in Baltimore, Maryland in 1918. The left panels show estimates for a set of 50 tuning parameters. The right column displays the CV-tuned estimates with approximate 95% confidence bands. The rows (top to bottom) show \hat{R}_t using Poisson trend filtering with $k = 1, 2, 3$ respectively.

4 Discussion

The `RtEstim` methodology provides a locally adaptive estimator using Poisson trend filtering. It captures the heterogeneous smoothness of instantaneous reproduction numbers given observed incidence data rather than resulting in global smoothness. This is a nonparametric regression model which can be written as a convex optimization problem. Minimizing the negative logliklihood of observations guarantees data fidelity while the penalty on divided differences between pairs of neighbouring parameters imposes smoothness. The ℓ_1 -regularization results in sparsity of the divided differences, leading to heterogeneous smoothness across time.

The property of local adaptivity (heterogenous smoothness) is useful to automatically distinguish, for example, seasonal outbreaks from outbreaks driven by other factors (behavioural changes, foreign introduction, etc.). Given a well-chosen polynomial degree, the growth rates can be quickly detected, potentially advising public health authorities to implement policy changes. The instantaneous reproduction numbers can be

estimated retrospectively to examine the efficacy of such policies, whether they result in
537
 \mathcal{R}_t falling below 1 or the speed of their effects. The smoothness of \mathcal{R}_t curves (including
538
the polynomial degrees and tuning parameters) should be chosen based on the purpose
539
of the study in practice or with data-driven risk estimation by cross validation.
540

Our method provides a natural way to deal with missing data, for example, on
541
weekends and holidays or due to changes in reporting frequency. While solving the
542
convex optimization problem, our method can easily handle uneven spacing or irregular
543
reporting. Computing the total primary infectiousness is also easily generalized to
544
irregular reporting through automatic modifications of the discretization of the serial
545
interval distribution. However, there are many other aspects to be considered in
546
choosing the delay distribution to improve accuracy [35]. Additionally, because the ℓ_1
547
penalty introduces sparsity (operating like a median rather than a mean), this
548
procedure is relatively insensitive to spurious outliers compared to ℓ_2 regularization.
549

There are a number of limitations that may influence the quality of \mathcal{R}_t estimation.
550
While our model is generic for incidence data rather than tailored to any specific
551
disease, it does assume that the generation interval is short relative to the period of
552
data collection. More specialized methodologies would be required for diseases with long
553
incubation periods such as HIV or Hepatitis. Our approach, does not explicitly model
554
imported cases, nor distinguish between subpopulations that may have different mixing
555
behaviour. However, a natural extension to handle imported cases is to follow the
556
suggested procedure of [11]. By including imported cases only in η_t rather than in both
557
 y_t and η_t , we exclude individuals who were infected elsewhere, lowering \mathcal{R}_t , but
558
correctly reflecting the number of new primary infectees.
559

While the Poisson assumption is common, it does not handle overdispersion
560
(observation variance larger than the mean). The negative binomial distribution is a
561
good alternative, but more difficult to estimate in this context. As described in
562
[Section 1](#), the expression for \mathcal{R} assumes that a relatively constant proportion of true
563
infections is reported. However, if this proportion varies with time (say, due to changes
564
in surveillance practices or testing recommendations), the estimates may be biased over
565
this window. A good example is in early January 2022, during the height of the
566
Omicron wave, Canada moved from testing all symptomatic individuals to testing only
567
those in at-risk groups. The result was a sudden change that would render \mathcal{R}_t estimates
568

on either side of this timepoint incommensurable.

Our **RtEstim** implementation can take a fixed serial interval throughout the period of study (as implemented in simulation and in the real epidemics) or use time-varying serial interval distributions (as implemented in Fig 1 for Covid-19 data in Canada). In reality, the serial interval may vary due to changes in the factors such as population immunity [12]. One issue regarding the serial interval distribution relates to equating serial and generation intervals (also mentioned above). The serial interval distribution is generally wider than that of the generation interval, because the serial interval involves the convolution of two distributions, and is unlikely to actually follow a named distribution like gamma, though it may be reasonably well approximated by one. Our implementation allows for an arbitrary distribution to be used, but requires the user to specify the discretization explicitly, requiring more nuanced knowledge than is typically available. Pushing this analysis further, to accommodate other types of incidence data (hospitalizations or deaths), a modified generation interval distribution would be necessary, and further assumptions would be required as well. Or else, one would first need to deconvolve deaths to infection onset before using our software.

Accurate statistical coverage of a function is a difficult problem, and the types of (frequentist) guarantees that can be made are not always what one would want [49]. We examine the coverage of our approximate confidence interval in simulation, with details are deferred to Section A.6 in the Supplement. Empirically, our observations for our method, as well as all others we have seen, follow a similar (undesirable) pattern: when \mathcal{R}_t is stable, they over cover dramatically (even implausibly narrow intervals have 100% coverage); but when \mathcal{R}_t changes abruptly, they under cover. Theoretically, whether these intervals should be expected to provide $(1 - \alpha)\%$ coverage simultaneously over all time while being narrow enough to provide useful uncertainty quantification is neither easy nor settled. An alternative to our approximation in Section 2.5, which we defer to future work, is to use the data fission method proposed by [50], which provides post-selection inference for trend filtering.

Nonetheless, our methodology is implemented in a lightweight R package **rtestim** and computed efficiently, especially for large-scale data, with a proximal Newton solver coded in C++. Given available incident case data, prespecified serial interval distribution, and a choice of degree k , **RtEstim** is able to produce accurate estimates of

instantaneous reproduction number and provide efficient tuning parameter selection via
601 cross validation.
602

Acknowledgments

This research was enabled in part by support provided by BC DRI group who manages
604 Cedar cloud (<https://docs.alliancecan.ca/wiki/Cedar>) and the Digital Research Alliance
605 of Canada (alliancecan.ca).
606

References

1. Nishiura H, Chowell G. The effective reproduction number as a prelude to statistical estimation of time-dependent epidemic trends. Mathematical and statistical estimation approaches in epidemiology. 2009; p. 103–121.
2. Fraser C. Estimating individual and household reproduction numbers in an emerging epidemic. PloS one. 2007;2(8):e758.
3. Gostic KM, McGough L, Baskerville EB, Abbott S, Joshi K, Tedijanto C, et al. Practical considerations for measuring the effective reproductive number, R_t . PLoS Computational Biology. 2020;16(12):e1008409.
4. Anderson RM, May RM. Infectious diseases of humans: dynamics and control. Oxford university press; 1991.
5. Wallinga J, Teunis P. Different epidemic curves for severe acute respiratory syndrome reveal similar impacts of control measures. American Journal of epidemiology. 2004;160(6):509–516.
6. Hao X, Cheng S, Wu D, Wu T, Lin X, Wang C. Reconstruction of the full transmission dynamics of COVID-19 in Wuhan. Nature. 2020;584(7821):420–424.
7. Goldstein IH, Parker DM, Jiang S, Minin VM. Semiparametric inference of effective reproduction number dynamics from wastewater pathogen surveillance data. arXiv preprint arXiv:230815770. 2023;.

8. Goldstein IH, Wakefield J, Minin VM. Incorporating testing volume into estimation of effective reproduction number dynamics. *Journal of the Royal Statistical Society Series A: Statistics in Society*. 2024;187(2):436–453.
9. Cori A, Cauchemez S, Ferguson NM, Fraser C, Dahlqwist E, Demarsh PA, et al.. EpiEstim: estimate time varying reproduction numbers from epidemic curves; 2020.
10. Cori A, Ferguson NM, Fraser C, Cauchemez S. A new framework and software to estimate time-varying reproduction numbers during epidemics. *American Journal of Epidemiology*. 2013;178(9):1505–1512.
11. Thompson RN, Stockwin JE, van Gaalen RD, Polonsky JA, Kamvar ZN, Demarsh PA, et al. Improved inference of time-varying reproduction numbers during infectious disease outbreaks. *Epidemics*. 2019;29:100356.
12. Nash RK, Bhatt S, Cori A, Nouvellet P. Estimating the epidemic reproduction number from temporally aggregated incidence data: A statistical modelling approach and software tool. *PLoS Computational Biology*. 2023;19(8):e1011439.
13. Abbott S, Hellewell J, Thompson RN, Sherratt K, Gibbs HP, Bosse NI, et al. Estimating the time-varying reproduction number of SARS-CoV-2 using national and subnational case counts. *Wellcome Open Research*. 2020;5:112.
14. Abbott S, Funk S, Hickson J, Badr HS, Monticone P, Ellis P, et al.. epiforecasts/EpiNow2: 1.4.0 release; 2023.
15. Lison A, Abbott S, Huisman J, Stadler T. Generative Bayesian modeling to nowcast the effective reproduction number from line list data with missing symptom onset dates. *PLoS Computational Biology*. 2024;20(4):e1012021.
16. Parag KV. Improved estimation of time-varying reproduction numbers at low case incidence and between epidemic waves. *PLoS Computational Biology*. 2021;17(9):e1009347.
17. Gressani O, Wallinga J, Althaus CL, Hens N, Faes C. EpiLPS: A fast and flexible Bayesian tool for estimation of the time-varying reproduction number. *PLoS Computational Biology*. 2022;18(10):e1010618.

18. Trevisin C, Bertuzzo E, Pasetto D, Mari L, Miccoli S, Casagrandi R, et al. Spatially explicit effective reproduction numbers from incidence and mobility data. *Proceedings of the National Academy of Sciences*. 2023;120(20):e2219816120.
19. Abry P, Pustelnik N, Roux S, Jensen P, Flandrin P, Gribonval R, et al. Spatial and temporal regularization to estimate COVID-19 reproduction number $R(t)$: Promoting piecewise smoothness via convex optimization. *PLoS ONE*. 2020;15(8):e0237901.
20. Pascal B, Abry P, Pustelnik N, Roux S, Gribonval R, Flandrin P. Nonsmooth convex optimization to estimate the Covid-19 reproduction number space-time evolution with robustness against low quality data. *IEEE Transactions on Signal Processing*. 2022;70:2859–2868.
21. Pircalabelu E. A spline-based time-varying reproduction number for modelling epidemiological outbreaks. *Journal of the Royal Statistical Society Series C: Applied Statistics*. 2023;72(3):688–702.
22. Ho F, Parag KV, Adam DC, Lau EH, Cowling BJ, Tsang TK. Accounting for the Potential of Overdispersion in Estimation of the Time-varying Reproduction Number. *Epidemiology*. 2023;34(2):201–205.
23. Azmon A, Faes C, Hens N. On the estimation of the reproduction number based on misreported epidemic data. *Statistics in Medicine*. 2014;33(7):1176–1192.
24. Gressani O, Faes C, Hens N. An approximate Bayesian approach for estimation of the instantaneous reproduction number under misreported epidemic data. *Biometrical Journal*. 2022;65(6):2200024.
25. Jin S, Dickens BL, Lim JT, Cook AR. EpiMix: A novel method to estimate effective reproduction number. *Infectious Disease Modelling*. 2023;8(3):704–716.
26. Hettinger G, Rubin D, Huang J. Estimating the instantaneous reproduction number with imperfect data: a method to account for case-reporting variation and serial interval uncertainty. *arXiv preprint arXiv:230212078*. 2023;.
27. Berry I, O'Neill M, Sturrock SL, Wright JE, Acharya K, Brankston G, et al. A sub-national real-time epidemiological and vaccination database for the

COVID-19 pandemic in Canada. *Scientific Data*. 2021;8(1).
doi:10.1038/s41597-021-00955-2.

28. Coronavirus Variants Rapid Response Network Computational Analysis M, Group EOC. CoVaRR-NET/duotang: Release for Zenodo Archive; 2023. Available from: <https://doi.org/10.5281/zenodo.10367461>.
29. Xu X, Wu Y, Kummer AG, Zhao Y, Hu Z, Wang Y, et al. Assessing changes in incubation period, serial interval, and generation time of SARS-CoV-2 variants of concern: a systematic review and meta-analysis. *BMC medicine*. 2023;21(1):374.
30. Park SW, Sun K, Champredon D, Li M, Bolker BM, Earn DJ, et al. Forward-looking serial intervals correctly link epidemic growth to reproduction numbers. *Proceedings of the National Academy of Sciences*. 2021;118(2):e2011548118.
31. Pitzer VE, Chitwood M, Havumaki J, Menzies NA, Perniciaro S, Warren JL, et al. The impact of changes in diagnostic testing practices on estimates of COVID-19 transmission in the United States. *American Journal of Epidemiology*. 2021;190(9):1908–1917.
32. Hitchings MD, Dean NE, García-Carreras B, Hladish TJ, Huang AT, Yang B, et al. The usefulness of the test-positive proportion of severe acute respiratory syndrome coronavirus 2 as a surveillance tool. *American Journal of Epidemiology*. 2021;190(7):1396–1405.
33. Pellis L, Scarabel F, Stage HB, Overton CE, Chappell LH, Fearon E, et al. Challenges in control of COVID-19: short doubling time and long delay to effect of interventions. *Philosophical Transactions of the Royal Society B*. 2021;376(1829):20200264.
34. Eales O, Riley S. Differences between the true reproduction number and the apparent reproduction number of an epidemic time series. *Epidemics*. 2024;46:100742. doi:<https://doi.org/10.1016/j.epidem.2024.100742>.

35. Park SW, Akhmetzhanov AR, Charniga K, Cori A, Davies NG, Dushoff J, et al. Estimating epidemiological delay distributions for infectious diseases. medRxiv. 2024; p. 2024–01.
36. Kim SJ, Koh K, Boyd S, Gorinevsky D. ℓ_1 trend filtering. SIAM Review. 2009;51(2):339–360.
37. Tibshirani RJ. Adaptive piecewise polynomial estimation via trend filtering. The Annals of Statistics. 2014;42(1):285–323.
38. Tibshirani RJ. Divided differences, falling factorials, and discrete splines: Another look at trend filtering and related problems. Foundations and Trends® in Machine Learning. 2022;15(6):694–846.
39. Sadhanala V, Bassett R, Sharpnack J, McDonald DJ. Exponential family trend filtering on lattices. Electronic Journal of Statistics. 2024;18(1):1749–1814.
40. Bergmeir C, Hyndman RJ, Koo B. A note on the validity of cross-validation for evaluating autoregressive time series prediction. Computational Statistics & Data Analysis. 2018;120:70–83. doi:<https://doi.org/10.1016/j.csda.2017.11.003>.
41. Vaiter S, Deledalle C, Fadili J, Peyré G, Dossal C. The degrees of freedom of partly smooth regularizers. Annals of the Institute of Statistical Mathematics. 2017;69:791–832.
42. Cori A, Kamvar Z, Stockwin J, Jombart T, Dahlqwist E, FitzJohn R, et al.. EpiEstim v2.2-4: A tool to estimate time varying instantaneous reproduction number during epidemics; 2022. <https://github.com/mrc-ide/EpiEstim>.
43. Gressani O. EpiLPS: A Fast and Flexible Bayesian Tool for Estimating Epidemiological Parameters.; 2021. <https://epilps.com/>.
44. Parag KV. EpiFilter; 2020.
<https://github.com/kpzoo/EpiFilter?tab=readme-ov-file>.
45. Groendyke C, Welch D, Hunter DR. Bayesian inference for contact networks given epidemic data. Scandinavian Journal of Statistics. 2011;38(3):600–616.

46. Lipsitch M, Cohen T, Cooper B, Robins JM, Ma S, James L, et al. Transmission dynamics and control of severe acute respiratory syndrome. *science*. 2003;300(5627):1966–1970.
47. Frost WH, Sydenstricker E. Influenza in Maryland: preliminary statistics of certain localities. *Public Health Reports (1896-1970)*. 1919; p. 491–504.
48. Taubenberger JK, Morens DM. 1918 Influenza: the mother of all pandemics. *Emerging Infectious Diseases*. 2006;17(1):69–79.
49. Genovese C, Wasserman L. Adaptive confidence bands. *The Annals of Statistics*. 2008;36(2):875 – 905. doi:10.1214/07-AOS500.
50. Leiner J, Duan B, Wasserman L, Ramdas A. Data fission: splitting a single data point. *Journal of the American Statistical Association*. 2023; p. 1–12.

Supplement for

RtEstim: Time-varying reproduction number estimation with trend filtering

Jiapeng Liu, Zhenglun Cai, Paul Gustafson, and Daniel J. McDonald

Contents

A.1 Derivation of Kullback Leibler divergence for accuracy comparison	1
A.2 Supplmentary details on experimental settings	2
A.3 Supplementary experimental results on accuracy comparison	5
A.3.1 Long epidemics	5
A.3.2 Short epidemics	8
A.4 Experimental results on accuracy under misspecification of serial interval distributions	10
A.4.1 SI misspecification for long epidemics	10
A.4.2 SI misspecification for short epidemics	13
A.5 Time comparisons of all methods	15
A.6 Confidence interval coverage	20
A.6.1 Estimates and confidence intervals for sample epidemics	20
A.6.2 Experimental settings for coverage comparisons of confidence intervals	25
A.6.3 Experimental results on interval coverage comparison	26
A.7 Data examples and alternative visualizations of Figs 5 and 6	33
A.7.1 More visualization of example epidemics	33
A.7.2 Alternative view of the difference between fitted and true Rt estimates	35
A.8 Application of RtEstim and all competitors on real epidemics	38
References	44

A.1 Derivation of Kullback Leibler divergence for accuracy comparison

We provide the detailed derivation of the Kullback Leibler (KL) divergence in Eq. (11) in the manuscript that is used to compare the accuracy of the estimated time-varying instantaneous reproduction number with the true ones. Given the total infectiousness η , we compare the distance between the Poisson distributions

$y \sim \text{Pois}(\eta\widehat{\mathcal{R}})$ and $y \sim \text{Pois}(\eta\mathcal{R})$, where $y, \mathcal{R} \in \mathbb{N}_0^n$ are natural numbers including 0, $\eta \in \mathbb{R}^n$, and $f_0(y; \eta, \mathcal{R}) = \prod_{t=1}^n \frac{(\eta_t \mathcal{R}_t)^{y_t} e^{-\eta_t \mathcal{R}_t}}{y_t!}$, $f_1(y; \eta, \widehat{\mathcal{R}}) = \prod_{t=1}^n \frac{(\eta_t \widehat{\mathcal{R}}_t)^{y_t} e^{-\eta_t \widehat{\mathcal{R}}_t}}{y_t!}$ are the corresponding density mass functions for independent $y_t, t = 1, \dots, n$. Because this is a natural exponential family with log-partition function $\exp(\cdot)$ and parameter $\log(\eta_t \mathcal{R}_t)$, then, the KL divergence between them can be written in terms of the Bregman divergence for \exp , e.g. Wainwright and Jordan (2008),

$$\begin{aligned}
D_{KL}(\mathcal{R} \parallel \widehat{\mathcal{R}}) &= D_{KL}(f_0(y; \eta, \mathcal{R}) \parallel f_1(y; \eta, \widehat{\mathcal{R}})) \\
&= D_{KL}\left(\prod_{t=1}^n f_0(y_t; \eta_t, \mathcal{R}_t) \parallel \prod_{t=1}^n f_1(y_t; \eta_t, \widehat{\mathcal{R}}_t)\right) \\
&= \sum_{t=1}^n D_{KL}\left(f_0(y_t; \eta_t, \mathcal{R}_t) \parallel f_1(y_t; \eta_t, \widehat{\mathcal{R}}_t)\right), \quad (\text{y_t are independent, conditional on $\mathcal{R}_t, \widehat{\mathcal{R}}_t, \eta_t$}) \\
&= \sum_{t=1}^n \exp(\log(\eta_t \widehat{\mathcal{R}}_t)) - \exp(\log(\eta_t \mathcal{R}_t)) + \exp(\log(\eta_t \mathcal{R}_t)) \log \frac{\eta_t \mathcal{R}_t}{\eta_t \widehat{\mathcal{R}}_t}, \quad (\text{definition of Bregman divergence}) \\
&= \sum_{t=1}^n \eta_t \widehat{\mathcal{R}}_t - \eta_t \mathcal{R}_t + \eta_t \mathcal{R}_t \log \frac{\mathcal{R}_t}{\widehat{\mathcal{R}}_t} \\
&= \sum_{t=1}^n \eta_t \left(\mathcal{R}_t \log \frac{\mathcal{R}_t}{\widehat{\mathcal{R}}_t} + \widehat{\mathcal{R}}_t - \mathcal{R}_t \right).
\end{aligned}$$

We use mean KL divergence (denoted, $\overline{D}_{KL}(\mathcal{R} \parallel \widehat{\mathcal{R}}) := D_{KL}(\mathcal{R} \parallel \widehat{\mathcal{R}})/N$, which is the KL divergence divided by the sequence length) in experiments for accuracy comparison.

A.2 Supplementary details on experimental settings

We compare the accuracy of the estimated instantaneous reproduction numbers using the mean Kullback Leibler (KL) divergence with Poisson distributional assumption on incidence (we say (mean) KL divergence for short in the following) in (11) across our **RtEstim** and several alternative methods, including **EpiEstim** with weekly and monthly sliding windows, **EpiLPS**, **EpiFilter**, **EpiNow2**, and **RtEstim** with degrees $k=0,1,2,3$, which yields 9 methods in total. We consider two lengths of epidemics with $n = 50$ or $n = 300$ timepoints respectively. Since **EpiNow2** takes too long to converge (e.g., for a long **measles** epidemic, it takes almost 2 hours on the Cedar cluster provided by Digital Research Alliance of Canada), we only compare it with other methods for short **flu** epidemics.

We consider the serial interval (SI) distributions of **measles** and **SARS** to generate long synthetic epidemics, and **flu** for short epidemics, inspired by Cori et al. (2013) which used SI from real epidemics to illustrate the performance of their method. The means and standard deviations of SI distributions are estimated by existing studies; specifically, (14.9, 3.9) for **measles** (Groendyke, Welch, and Hunter (2011)), (8.4, 3.8) for **SARS** (Lipsitch et al. (2003)), and (2.6, 1.5) for **flu** (Ferguson et al. (2005), Boëlle et al. (2011)). Incident cases in synthetic **measles** epidemics are relatively low (within 1000 at the peak overall), and **SARS** incident cases are relatively large (between 15000 and 20000 at the peak overall).

We consider a reasonably large overdispersion level of negative binomial incidence with size 5. Figure A.2.1

displays the ratio of the variance over mean across different settings using the same set of sample epidemics in Fig 5 and Fig 6, and all figures in Section A.6.1. For Poisson, this ratio is constant at 1. However, the negative binomial incidence appears results in significant overdispersion.

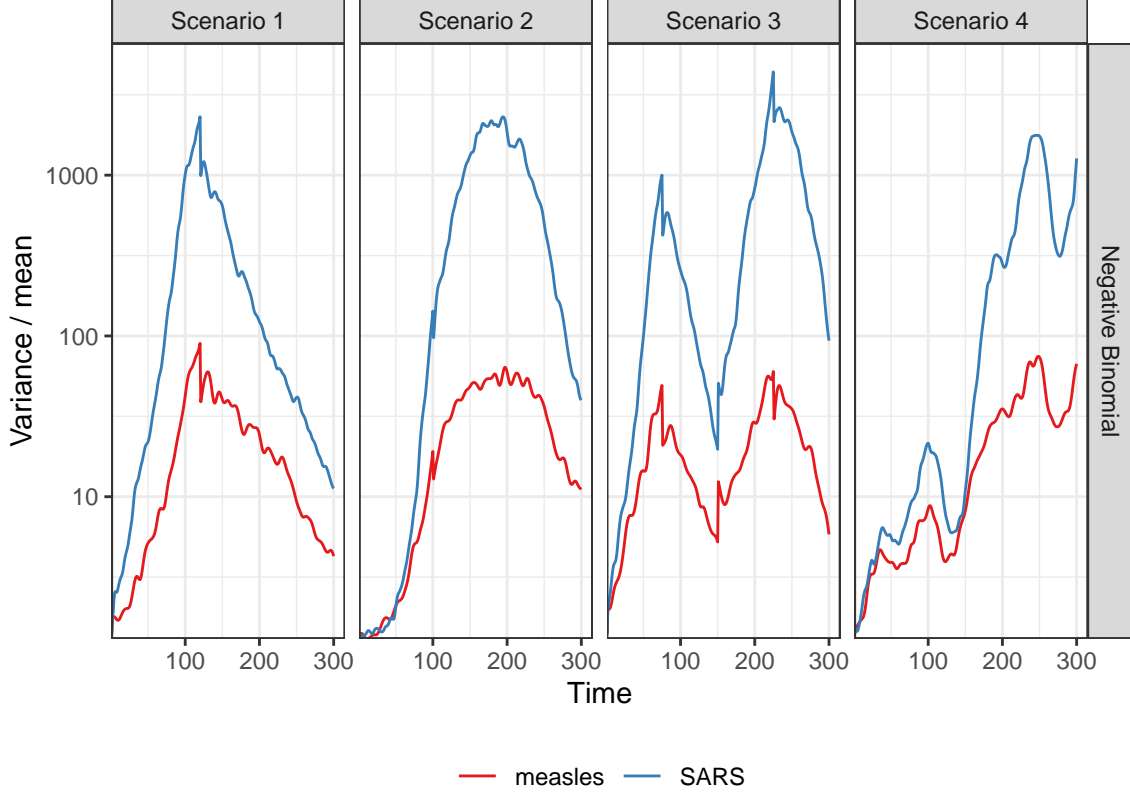


Figure A.2.1: Dispersion level of incidence of sample negative binomial epidemics.

In model fitting, we use both true and misspecified serial interval (SI) distributions to test the robustness of our method, compared to other alternatives. The misspecification of serial interval distributions are either “mild” or “major”, where, in the major misspecification, we use a completely different pair of SI parameters, e.g., we use the SI of **SARS** for generated **measles** epidemics, and the SI of **measles** for generated **flu** epidemics. In the mild SI misspecification, we consider slightly adjusted parameters for both **measles** and **flu** epidemics, where the mean is decreased by 2 for **measles** and increased by 2 for **flu** and the standard deviation is increased by 10%, denoted as **adj_flu** and **adj_measles** respectively. These settings result in 7 pairs of SI distributions (for epidemic generating, model fitting), i.e., (**measles**, **measles**), (**SARS**, **SARS**), (**measles**, **adj_measles**), (**measles**, **SARS**) for long epidemics and (**flu**, **flu**), (**flu**, **adj_flu**), (**flu**, **measles**) for short epidemics. Figure A.2.2 displays all SI distributions (**measles**, **adj_measles**, **SARS**, **flu**, and **adj_flu**) used in the experiments.

Table 1 summarizes the aforementioned experimental setting for accuracy comparison: Poisson and negative binomial (NB) distributions for incidence and four \mathcal{R}_t scenarios are used for all long epidemics. We only consider one \mathcal{R}_t scenario (Scenario 3: piecewise linear \mathcal{R}_t) for short epidemics. Each experimental setting is replicated 50 times, which yields 12800 experiments for long epidemics and 2700 for short epidemics.

We visualize the selected key results of the accuracy comparison using long synthetic epidemics in Section 3.2 in the manuscript. Other main experimental results are displayed in Section A.3.

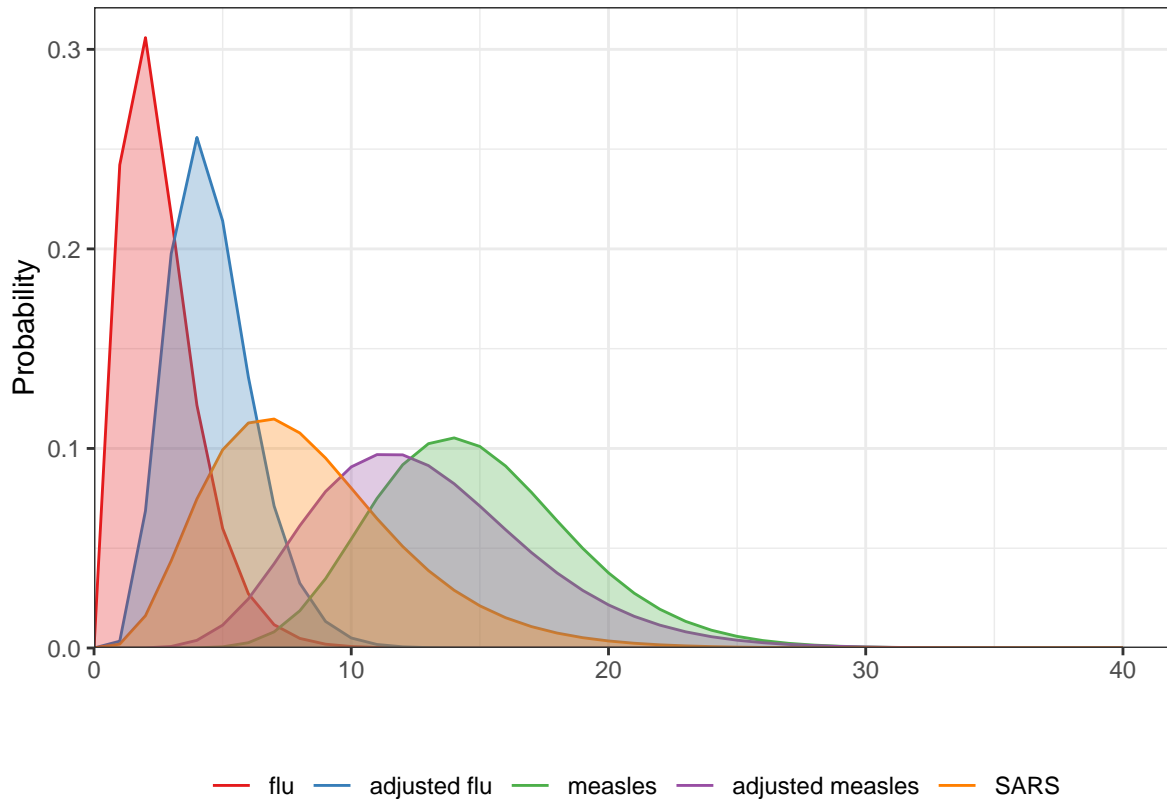


Figure A.2.2: Density curves of serial interval distributions used in the experiments.

Table 1: Summary of experimental settings on accuracy comparison.

Length	SI	Rt scenario	Incidence	SI for modelling	Method
300	measles	1-4	Poisson, NB	measles, adj-measles, SARS	8 methods
300	SARS	1-4	Poisson, NB	SARS	8 methods
50	flu	3	Poisson, NB	flu, adj-flu, measles	9 methods

A.3 Supplementary experimental results on accuracy comparison

A.3.1 Long epidemics

We have displayed the accuracy of all methods (where EpiEstim uses weekly sliding window) for `measles` and `SARS` sample epidemics using KL divergence excluding the first week since EpiEstim does not provide estimates in the first week in Fig 3 and Fig 4 in the manuscript, where we exclude the outliers. A full visualization including the outliers is in Figure A.3.1.

Figure A.3.2 compares `EpiEstim` with *monthly* sliding windows with other methods. We average the KL divergence per coordinate excluding the timepoints in the first month for all approaches, since `EpiEstim` estimates with the monthly sliding windows are not available until the second month. The y -axis is displayed on a logarithmic scale for a better visualization.

The relative performance of `EpiEstim` with monthly sliding windows, in general, is not as good as its weekly sliding window based on the relative positions of its boxes and the counterparts of the other methods. It can be explained that `EpiEstim` with longer sliding windows assume similarity of neighbouring \mathcal{R}_t across longer periods, and thus, is smoother and less accurate compared to the one with shorter sliding windows.

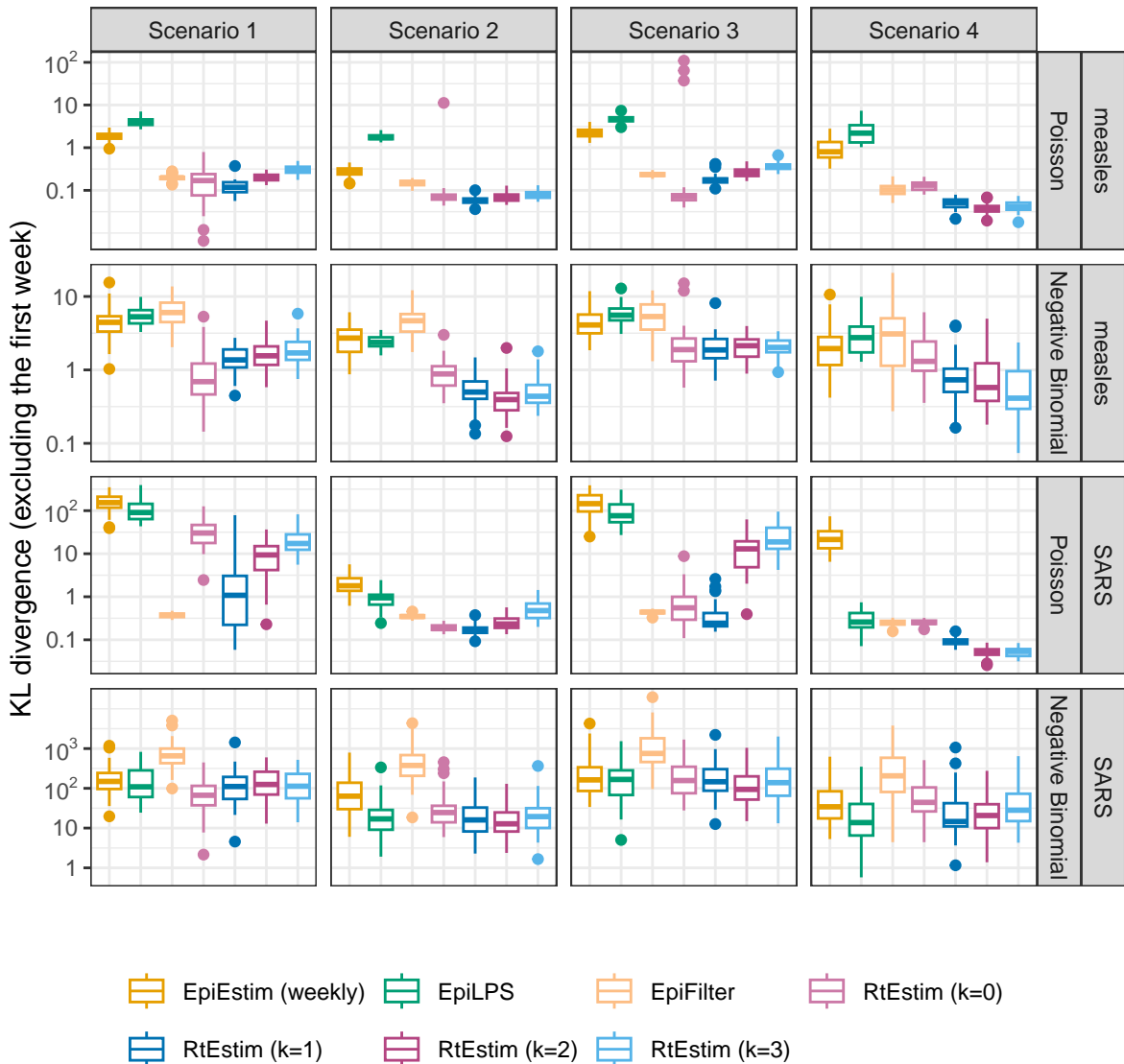


Figure A.3.1: The mean KL divergence excluding the first week for measles and SARS epidemics, since EpiEstim with the weekly sliding window does not provide estimates for the first week. Y-axes are on a logarithmic scale.

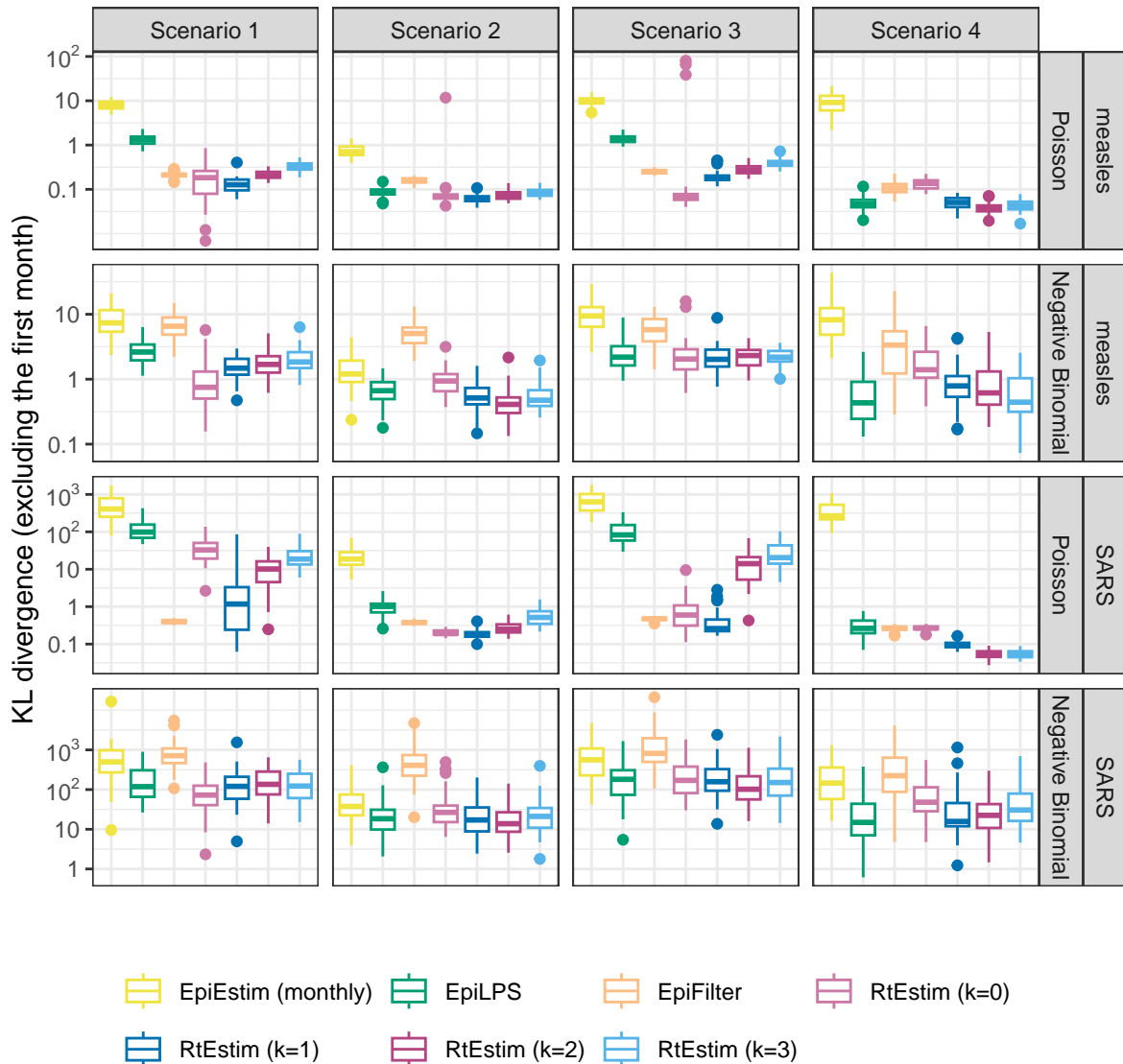


Figure A.3.2: The mean KL divergence excluding the first month for measles and SARS epidemics, since EpiEstim with the monthly sliding window does not provide estimates for the first month. Y-axes are on a logarithmic scale.

A.3.2 Short epidemics

Figures A.3.3 and A.3.4 display the KL divergence for short epidemics aggregated over time excluding the first week and month respectively to compare EpiEstim with weekly and monthly sliding windows with other methods including EpiNow2. The difference in accuracy is more obvious given Poisson distributional assumption in incidence. To estimate “true” piecewise linear \mathcal{R}_t , piecewise constant and linear RtEstim (with $k = 0, 1$) are the most accurate for Poisson incidence, RtEstim ($k = 2, 3$), EpiLPS and EpiFilter are accurate as well with median KL estimates around 1. For negative binomial incidence, the advantage of RtEstim is less obvious, but RtEstim with all degrees still has the lowest median with a small IQR.

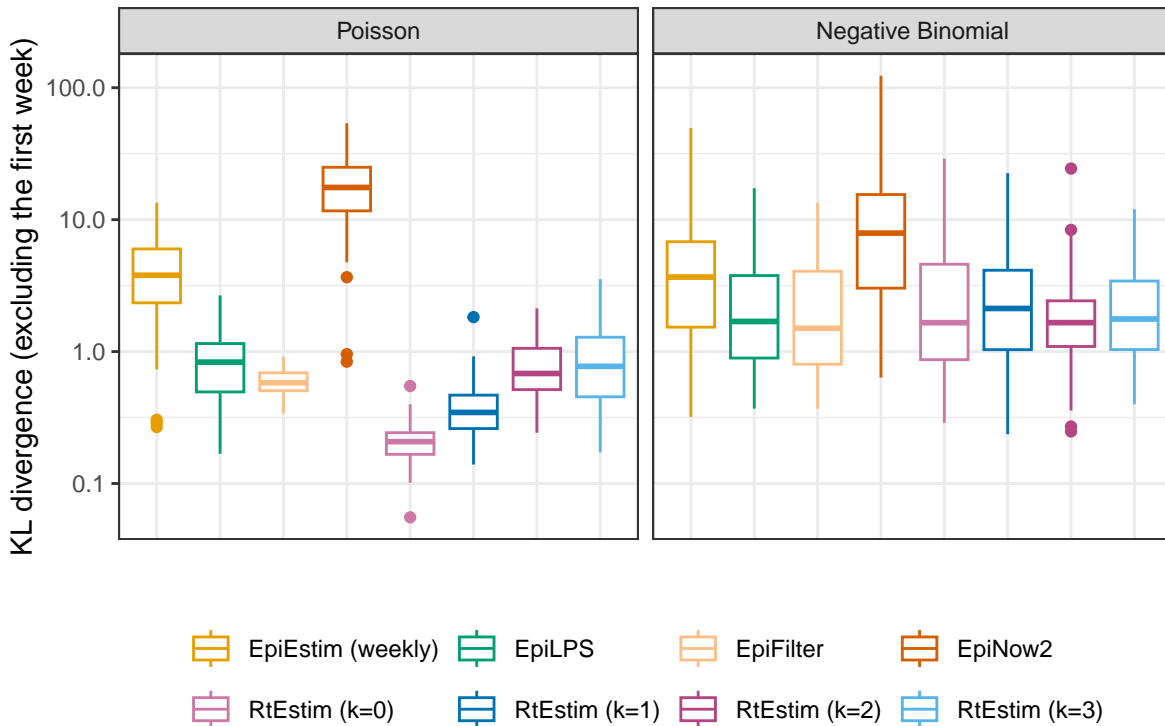


Figure A.3.3: The average KL divergence excluding the first week for flu epidemics, since EpiEstim with the weekly sliding window does not provide estimates for the first week. Y-axes are on a logarithmic scale.

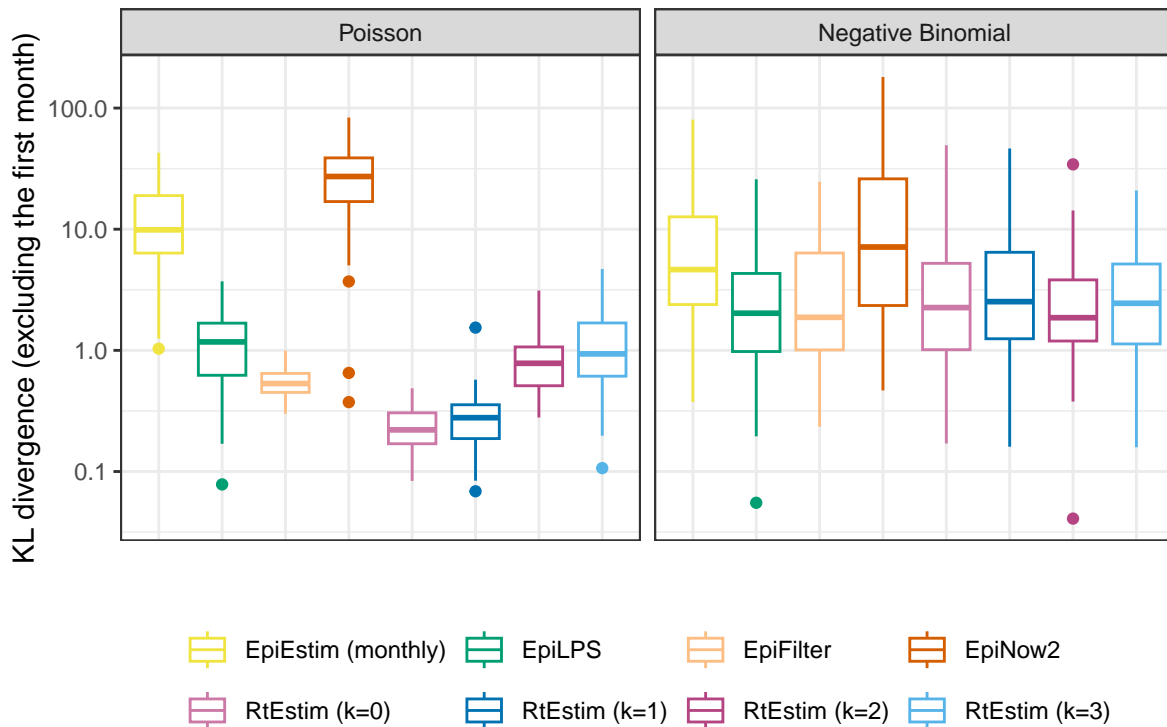


Figure A.3.4: The mean KL divergence excluding the first month for flu epidemics, since EpiEstim with the monthly sliding window does not provide estimates for the first month. Y-axes are on a logarithmic scale.

A.4 Experimental results on accuracy under misspecification of serial interval distributions

A.4.1 SI misspecification for long epidemics

Figures A.4.1 and A.4.2 display KL divergence (excluding the first week and the first month respectively) for all 8 methods with “mild” misspecification (using shaped and scaled `measles` SI parameters) and “major” misspecification (using `SARS` SI parameters) for long `measles` epidemics across all settings. `RtEstim` is reasonably robust to misspecification of SI parameters: median KL error for each problem design is almost always the lowest with the lowest IQR. `EpiLPS` is a strong competitor given negative binomial incidence, since it assumes incidence to follow negative binomial distributions. `EpiFilter` is also quite robust to SI misspecification under Poisson incidence.

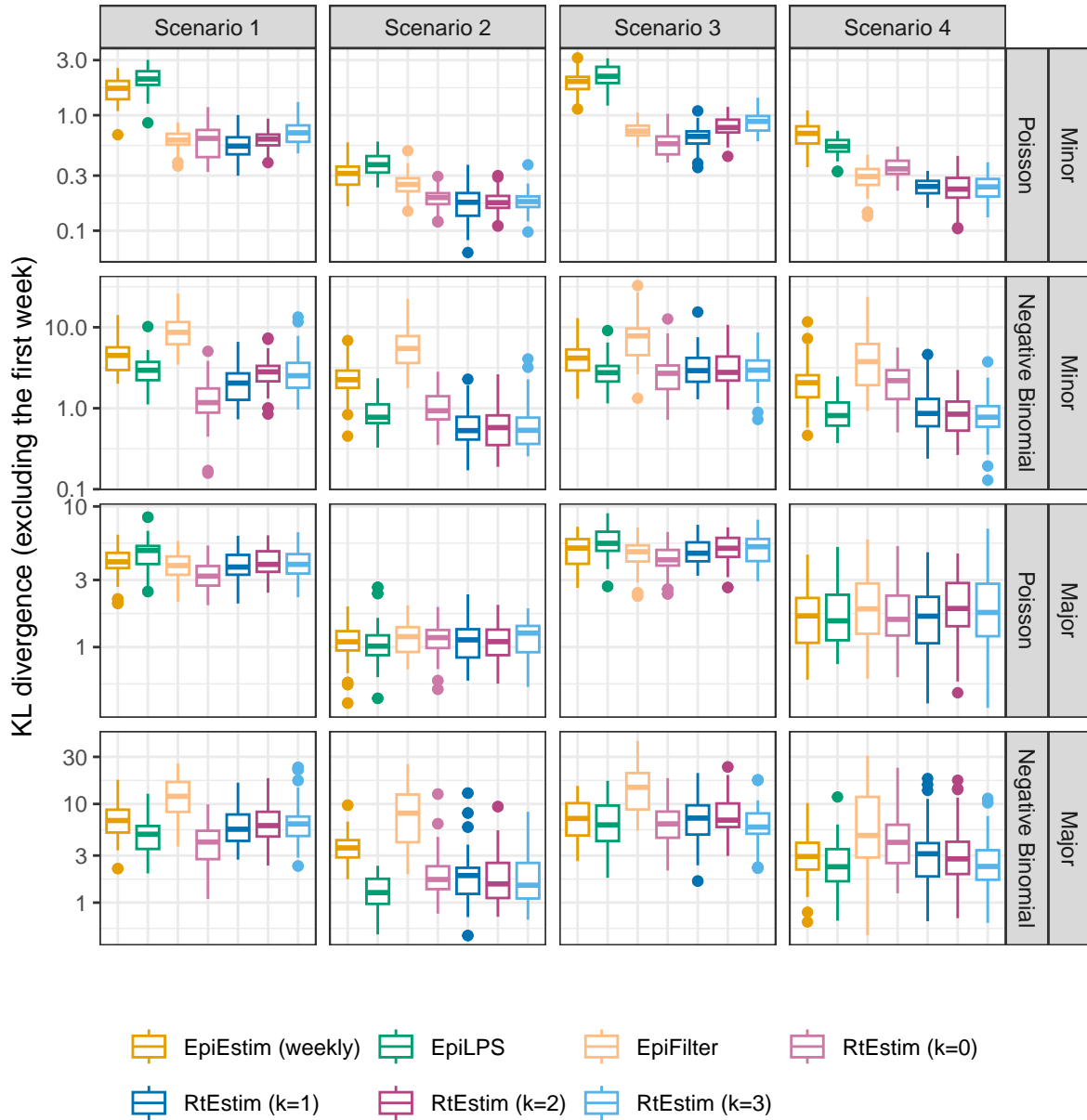


Figure A.4.1: The mean KL divergence excluding the first week for measles epidemics with SI misspecification, since EpiEstim with the weekly sliding window does not provide estimates for the first week. Y-axes are on a logarithmic scale.

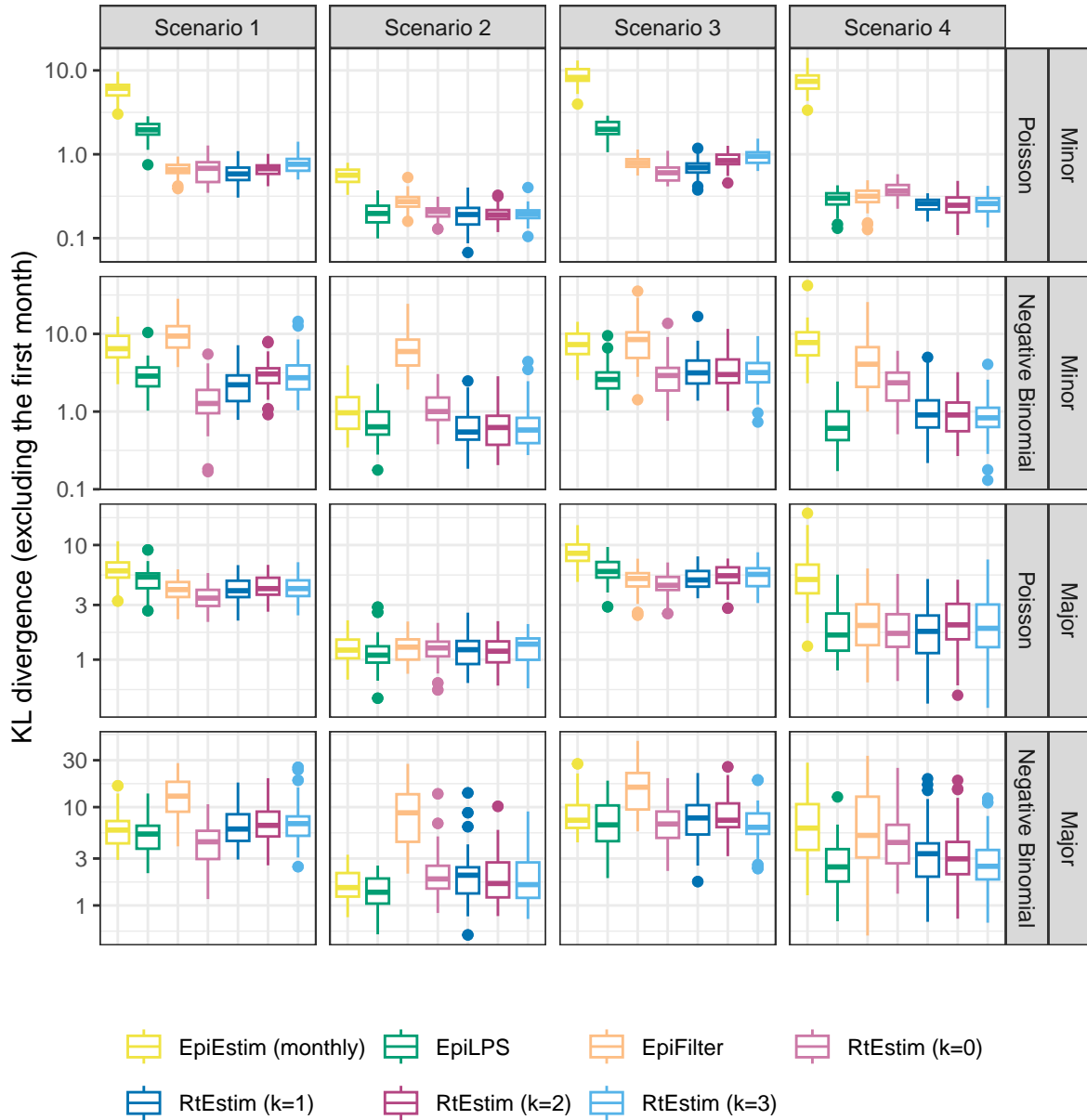


Figure A.4.2: The mean KL divergence excluding the first month for measles epidemics with SI misspecification, since EpiEstim with the monthly sliding window does not provide estimates for the first month. Y-axes are on a logarithmic scale.

A.4.2 SI misspecification for short epidemics

Figures A.4.3 and A.4.4 display KL divergence (excluding the first week and the first month respectively) for all 9 methods with “minor” misspecification (using slightly modified f1u SI parameters) and “major” misspecification (using measles parameters) for short f1u epidemics across all settings, yielding similar conclusions as in short epidemics. We also note that EpiNow2 is quite robust to major misspecification in SI parameters, while EpiLPS is less satisfactory in major misspecification excluding the first week in KL computation. It might be due to the large estimates at the beginning of the epidemics beyond the first week, but eliminated within the first month.

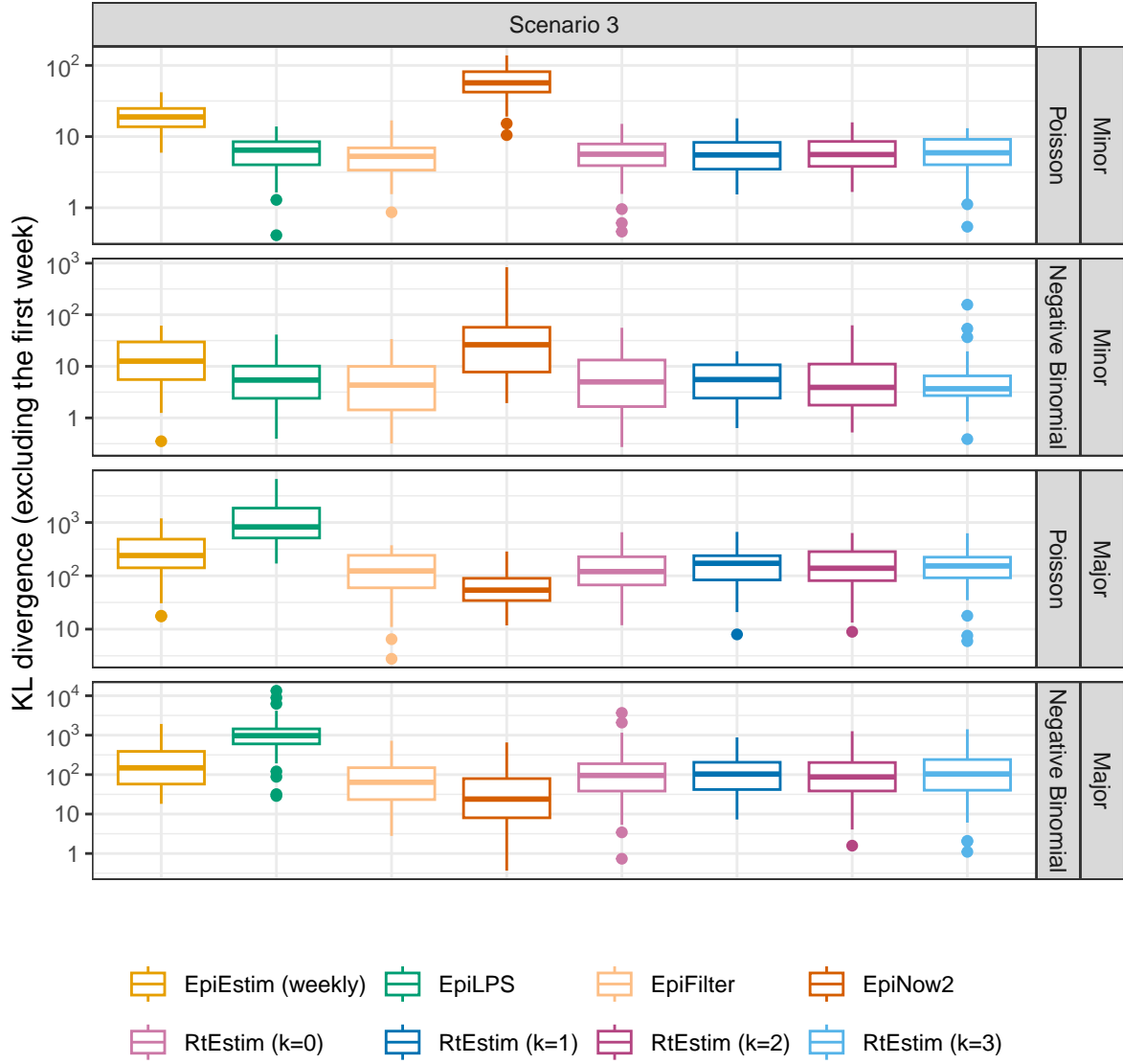


Figure A.4.3: The mean KL divergence excluding the first week for flu epidemics with SI misspecification, since EpiEstim with the weekly sliding window does not provide estimates for the first week. Y-axes are on a logarithmic scale.

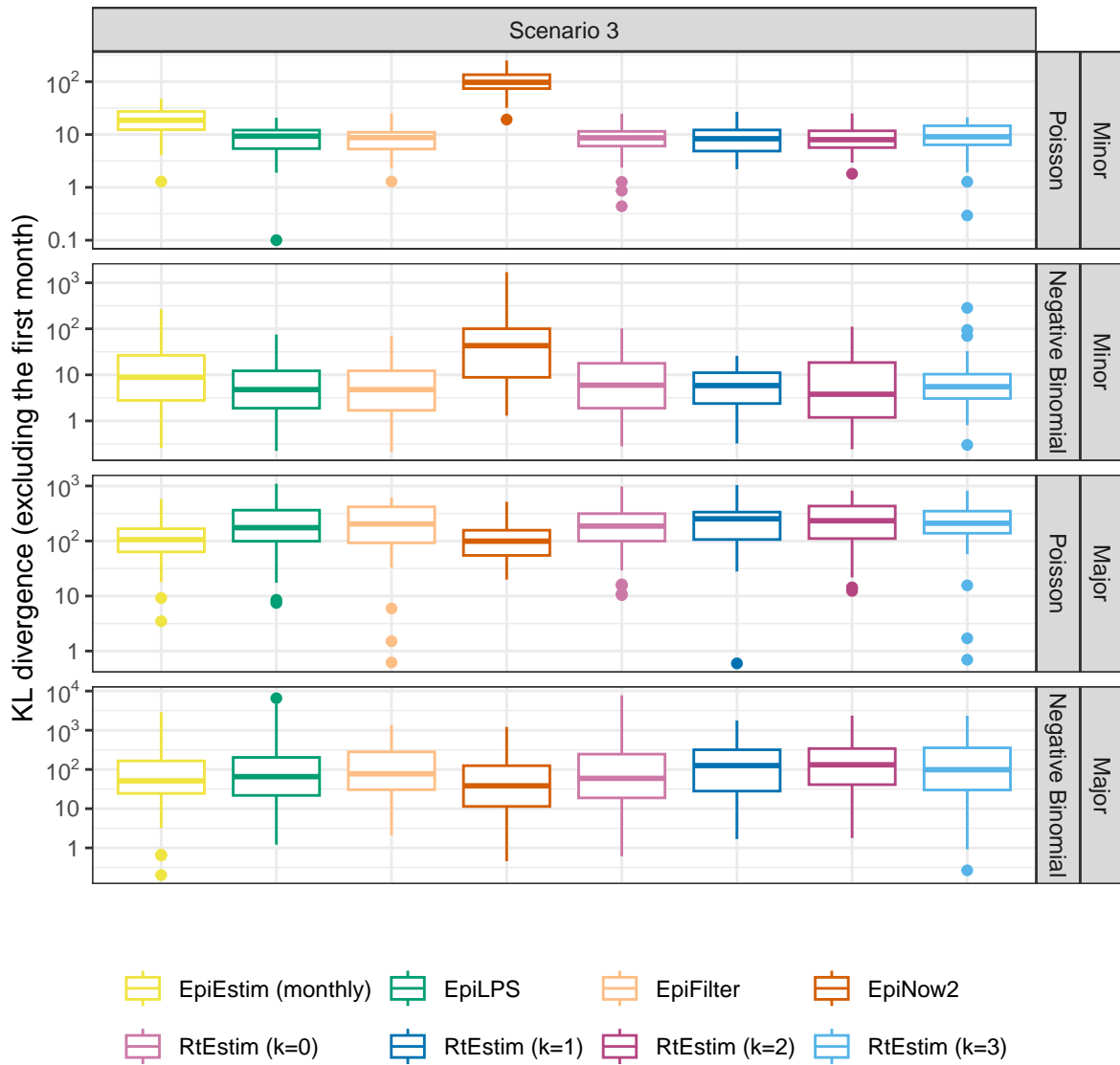


Figure A.4.4: The mean KL divergence excluding the first month for flu epidemics with SI misspecification, since EpiEstim with the monthly sliding window does not provide estimates for the first month. Y-axes are on a logarithmic scale.

A.5 Time comparisons of all methods

Figures A.5.1 show the time comparisons across all methods for long (`measles` and `SARS`) epidemics. `EpiEstim` with both sliding windows are very fast and converge in less than 0.1 seconds. Piecewise constant `RtEstim` (with $k=0$) estimates can be generated within 0.1 seconds as well. `EpiLPS` is slightly slower, but still very fast and within 1 second for all experiments. `EpiFilter` is in a similar scale of our method with higher than 0 degrees. Piecewise linear and cubic `RtEstim` (with $k = 1$ and $k = 3$ respectively) are slower, but mostly within 10 seconds. We also provide an alternative view with the running time of each case in a separate panel in Figures A.5.2 and A.5.3 for `measles` and `SARS` epidemics respectively. We find similar results as in Figure A.5.1 in all panels.

It is remarkable that our `RtEstim` computes 50 lambda values with 10-fold CV for each experiment, which results in $550 \times$ the number of models estimated per experiment (including modelling for all folds). The running times are no more than 10 seconds for most of the experiments, which means the running time for each time of estimate is very fast, and on average can be less than 0.02 seconds. The other methods only run once for a fixed set of hyperparameters for each experiment.

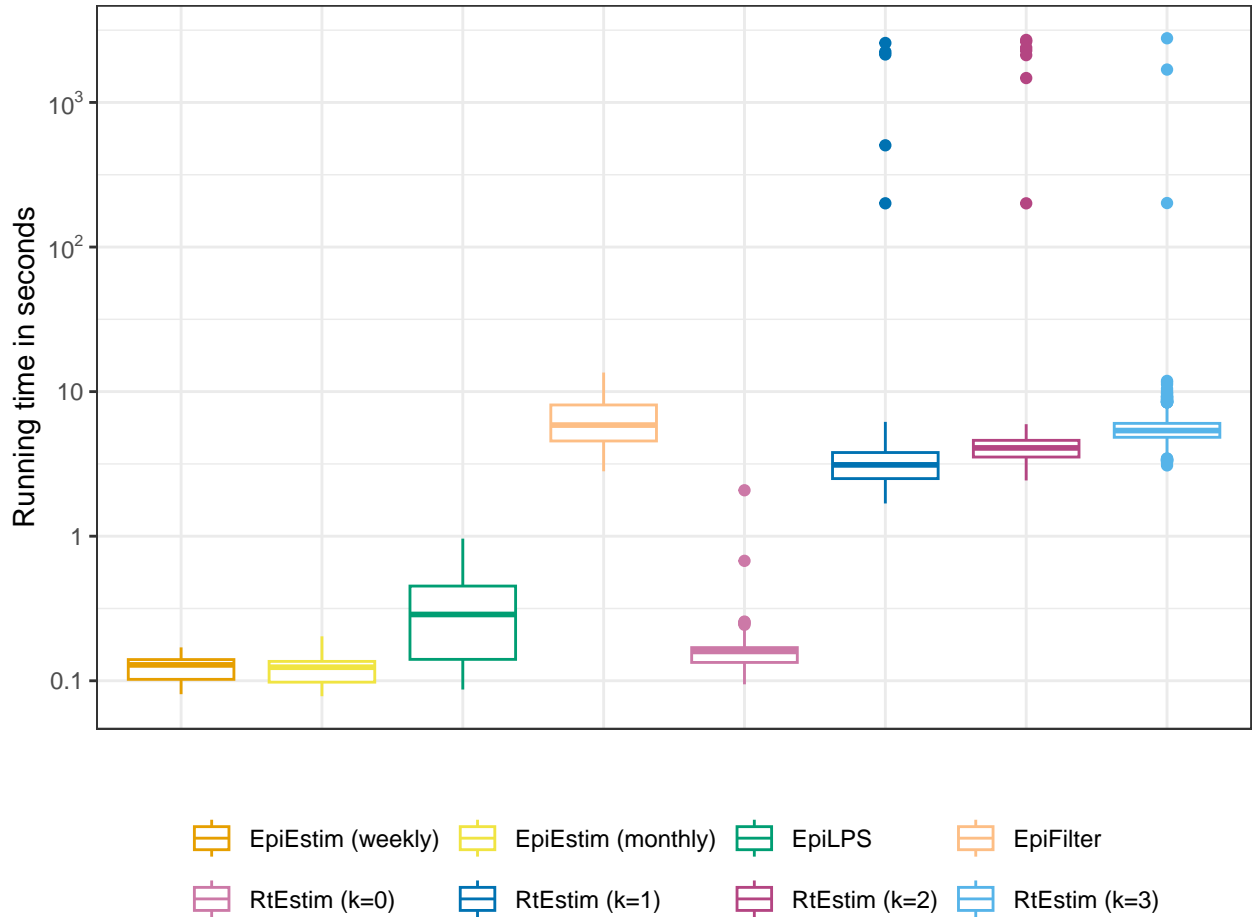


Figure A.5.1: Running time comparison of all methods for long (`measles` and `SARS`) epidemics across all cases. Y-axis is on a logarithmic scale.

Figure A.5.4 displays the running time of all methods for short (`flu`) epidemics. All methods except `EpiNow2`

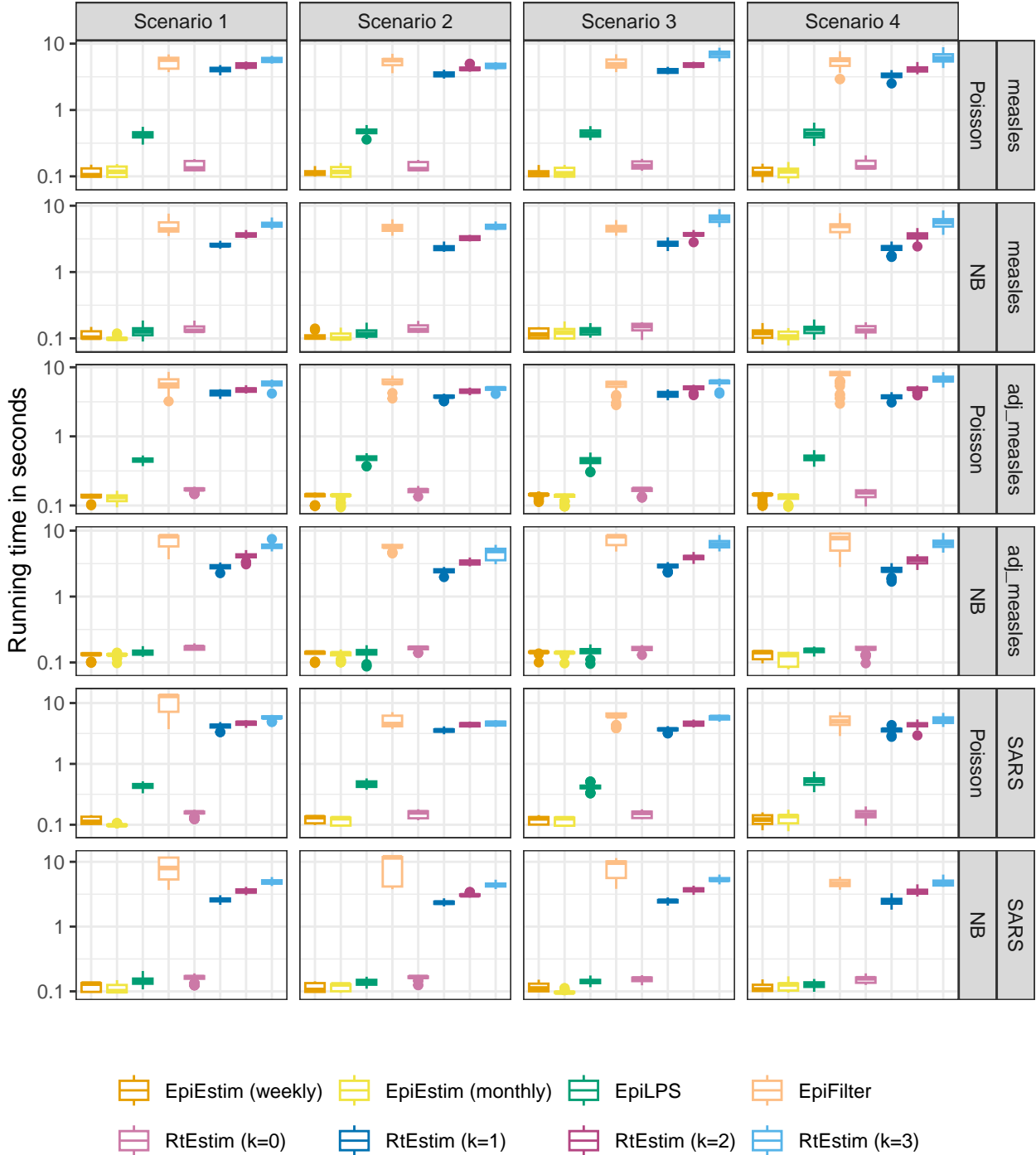


Figure A.5.2: Running time comparison of all methods for measles epidemics with each pair of SI parameters (measles, adjusted measles, and SARS) for modelling per incidence distribution per Rt scenario (excluding outliers for better illustration). Y-axes are on a logarithmic scale.

can converge with in around 1 second. Figure A.5.5 displays the running times for each setting separately, and finds similar results as in the overall running time comparison.

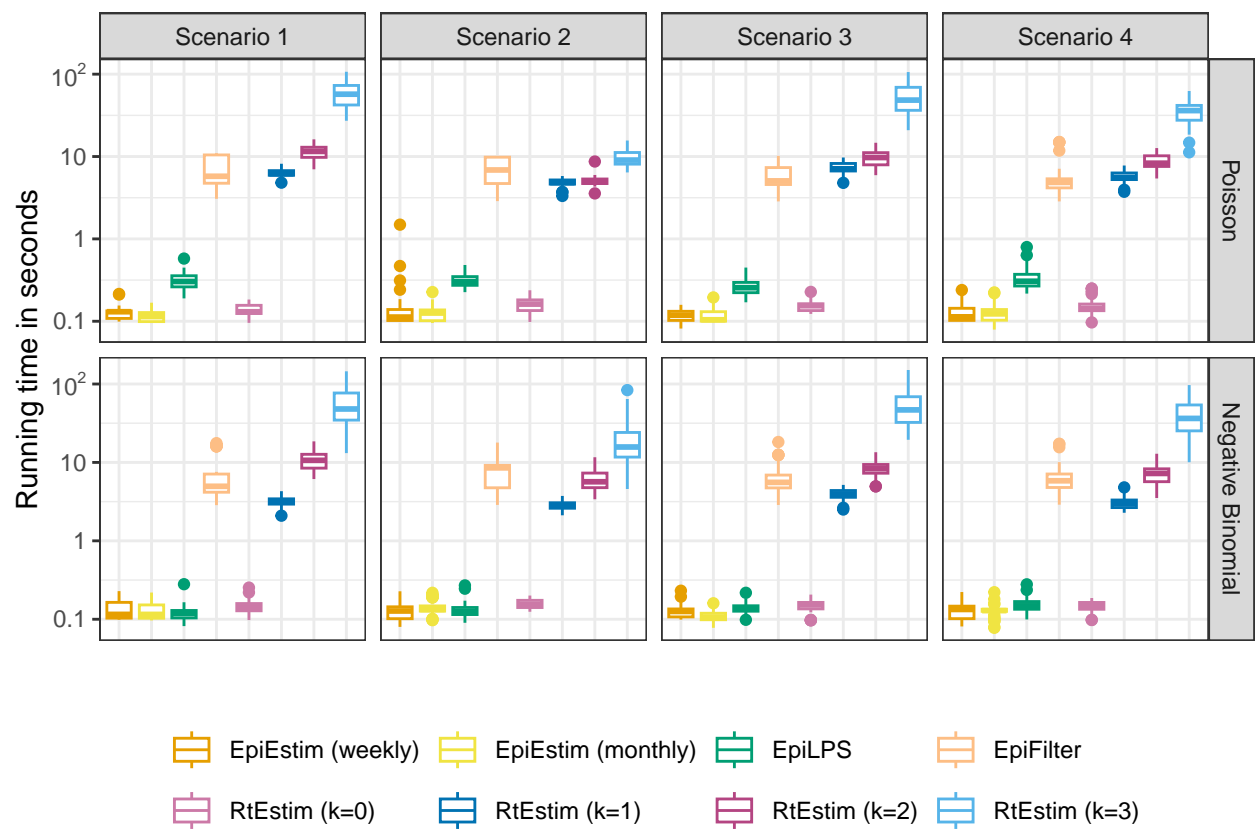


Figure A.5.3: Running time comparison of all methods for SARS epidemics with each choice of SI parameter for modelling per incidence distribution per Rt scenario. Y-axes are on a logarithmic scale.

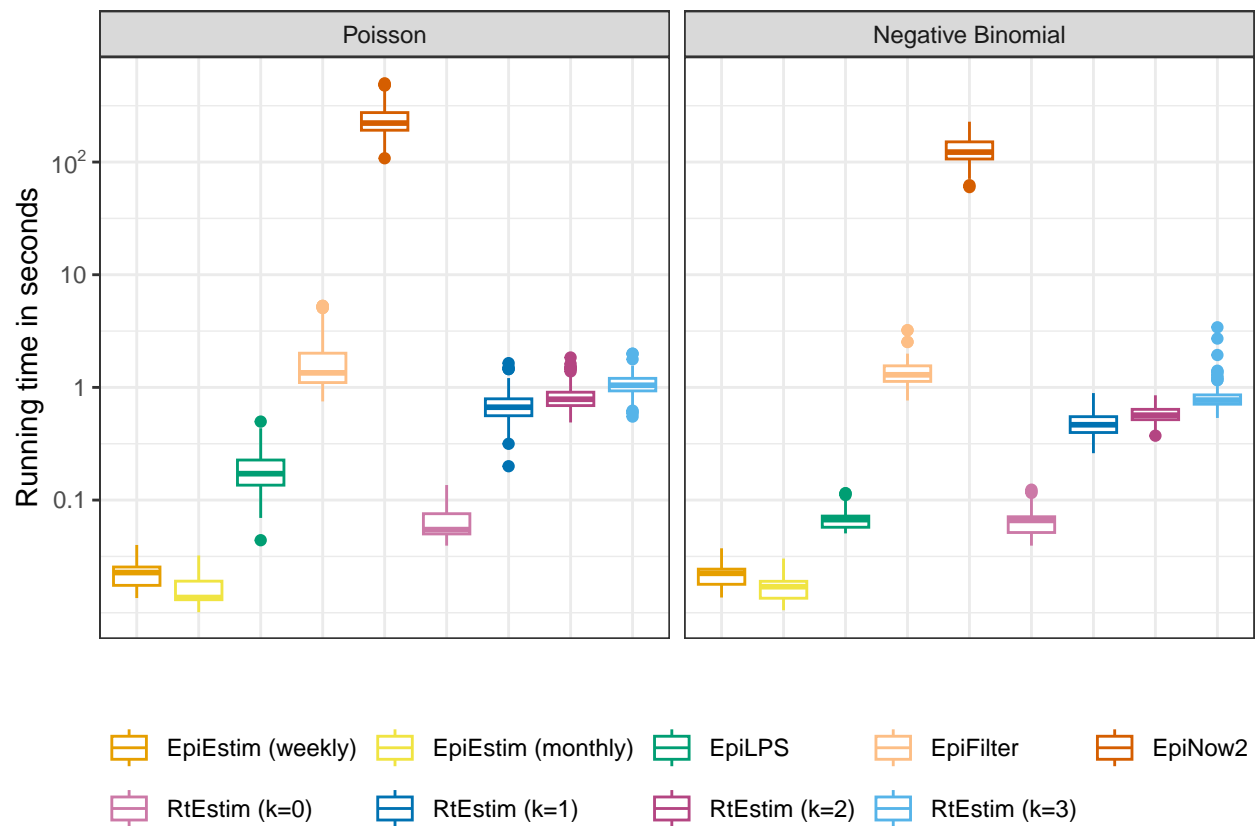


Figure A.5.4: Time comparisons of methods for short (flu) epidemics across all pairs of SI parameters per incidence distribution. Y-axes are on a logarithmic scale.

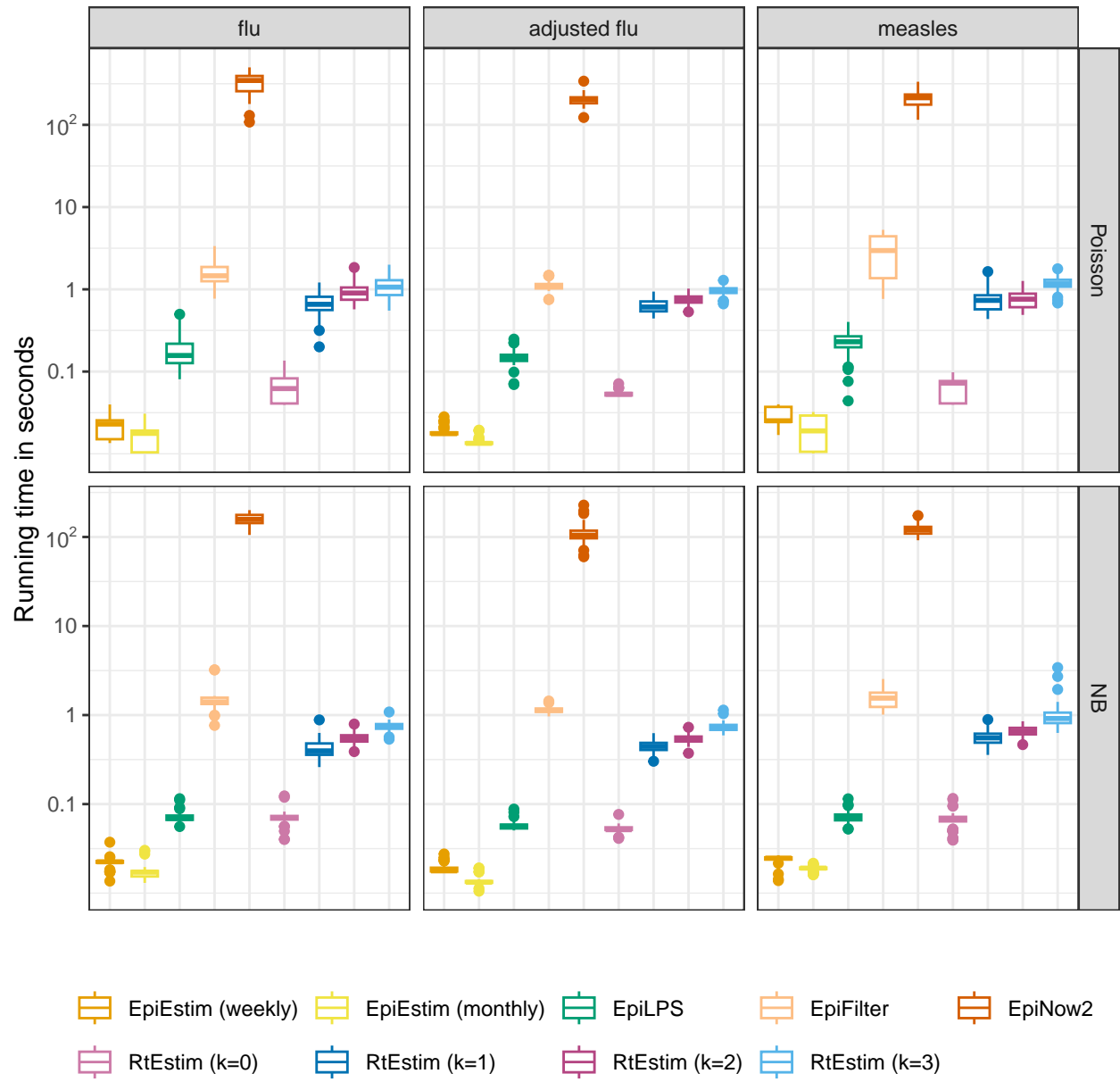


Figure A.5.5: Time comparisons of methods for short (flu) epidemics for piecewise linear Rt (Scenario 3) for different pairs of SI parameters (flu, adjusted flu, and measles) and incidence distributions in different panels. Y-axes are on a logarithmic scale.

A.6 Confidence interval coverage

A.6.1 Estimates and confidence intervals for sample epidemics

Fig 5 and Fig 6 in the manuscript provided \mathcal{R}_t estimates by all methods on sample **measles** epidemics with Poisson incidence and **SARS** epidemics with negative binomial incidence respectively. Figures A.6.1 and A.6.4 provide a clearer view of each method with its 95% confidence interval in a separate panel. The full display of sample epidemics for other settings are visualized in Figures A.6.2 and A.6.3.

All methods (except EpiEstim with the monthly sliding window) fit the epidemics with Poisson incidence well with estimate $\hat{\mathcal{R}}_t$ close to the true \mathcal{R}_t and 95% CI covering the true value at most timepoints. Under negative binomial incidence, RtEstim with $k = 0$ fails to recover the curvature in \mathcal{R}_t , especially in the exponential and periodic scenarios. EpiEstim with weekly sliding windows and EpiFilter are more wiggly, and EpiLPS has wider confidence intervals given negative binomial incidence compared to Poisson incidence. For large incidence under the negative binomial distribution, EpiFilter is extremely wiggly, and it is difficult for RtEstim ($k=0$) to recover many changepoints and the curvature especially in exponential and periodic scenarios. EpiLPS performs well overall, but returns large estimates at the beginning of the epidemics, estimates which remain inflated well after the first week. Overall, our method with different degrees can recover the changepoints and graphical curvature of \mathcal{R}_t in all scenarios, except in the case of the periodic \mathcal{R}_t curve with large incidence from negative binomial distribution, where EpiLPS has a clear advantage, ignoring the large estimates at the early stage. The accuracy across different settings by different methods generally coincides with the findings in the KL divergence estimates.

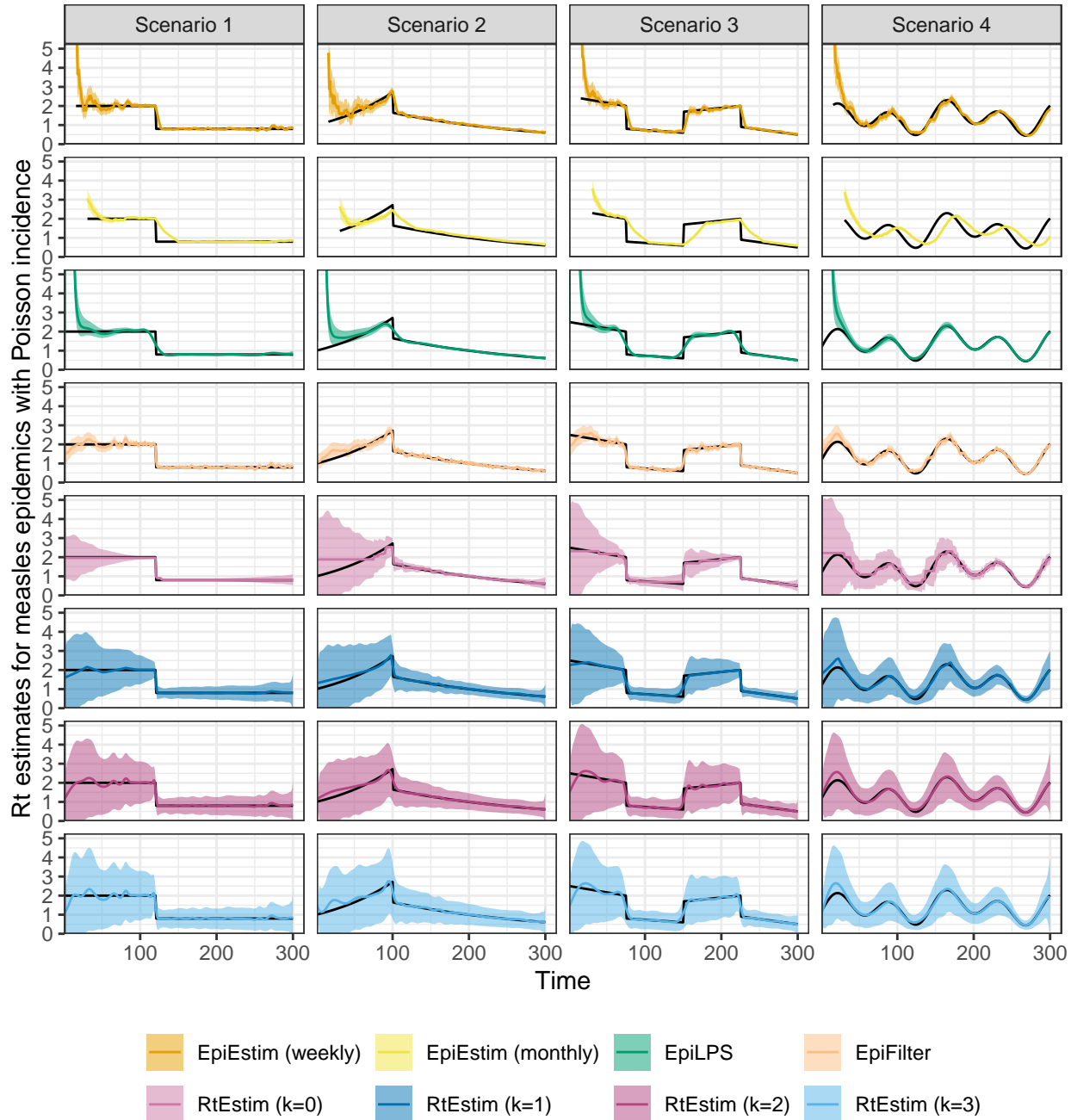


Figure A.6.1: Example measles epidemics with Poisson incidence. Y-axes beyond 5 are truncated for a better illustration of small values.

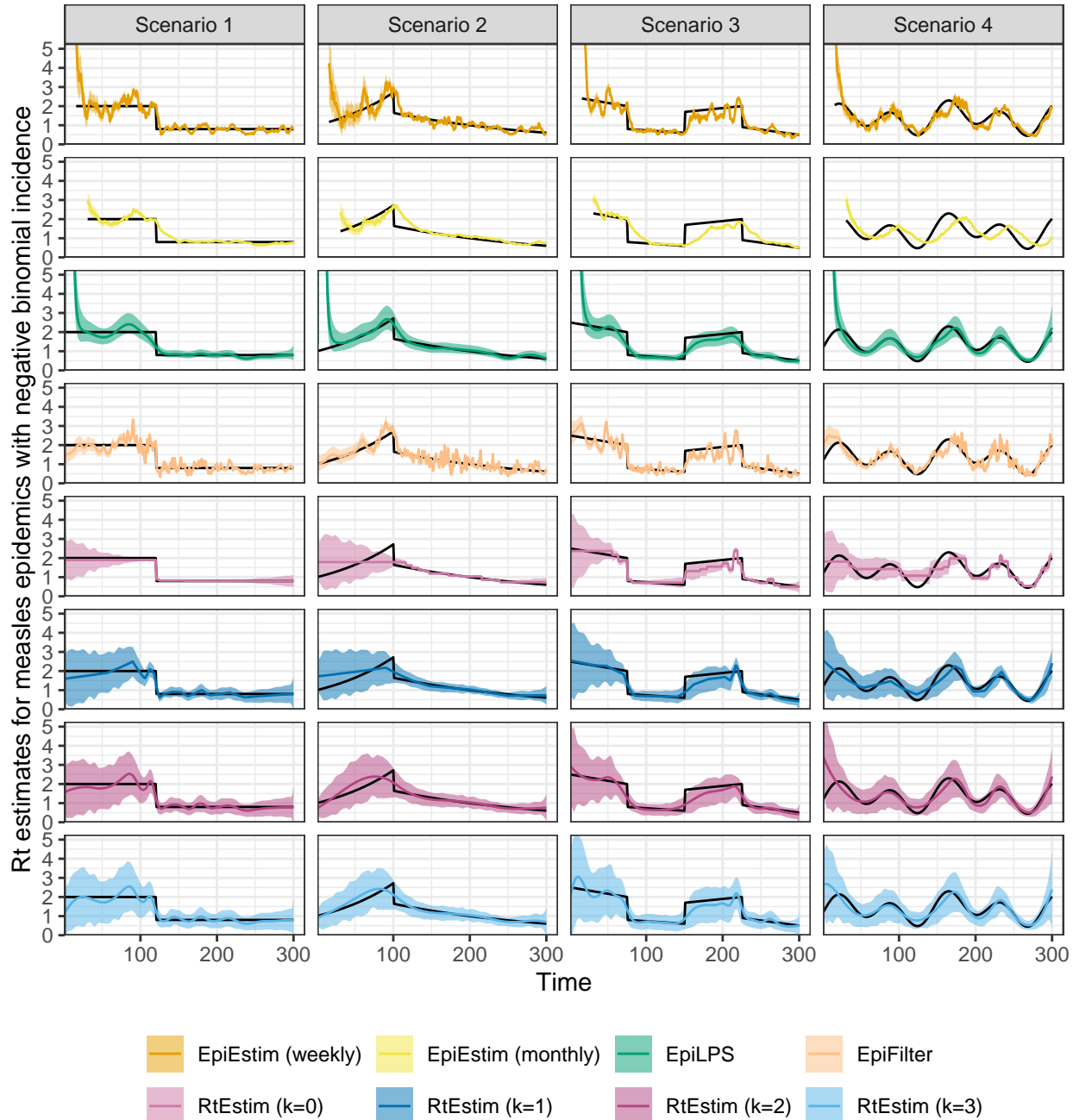


Figure A.6.2: Example measles epidemics with negative binomial incidence. Y-axes beyond 5 are truncated for a better illustration of small values.

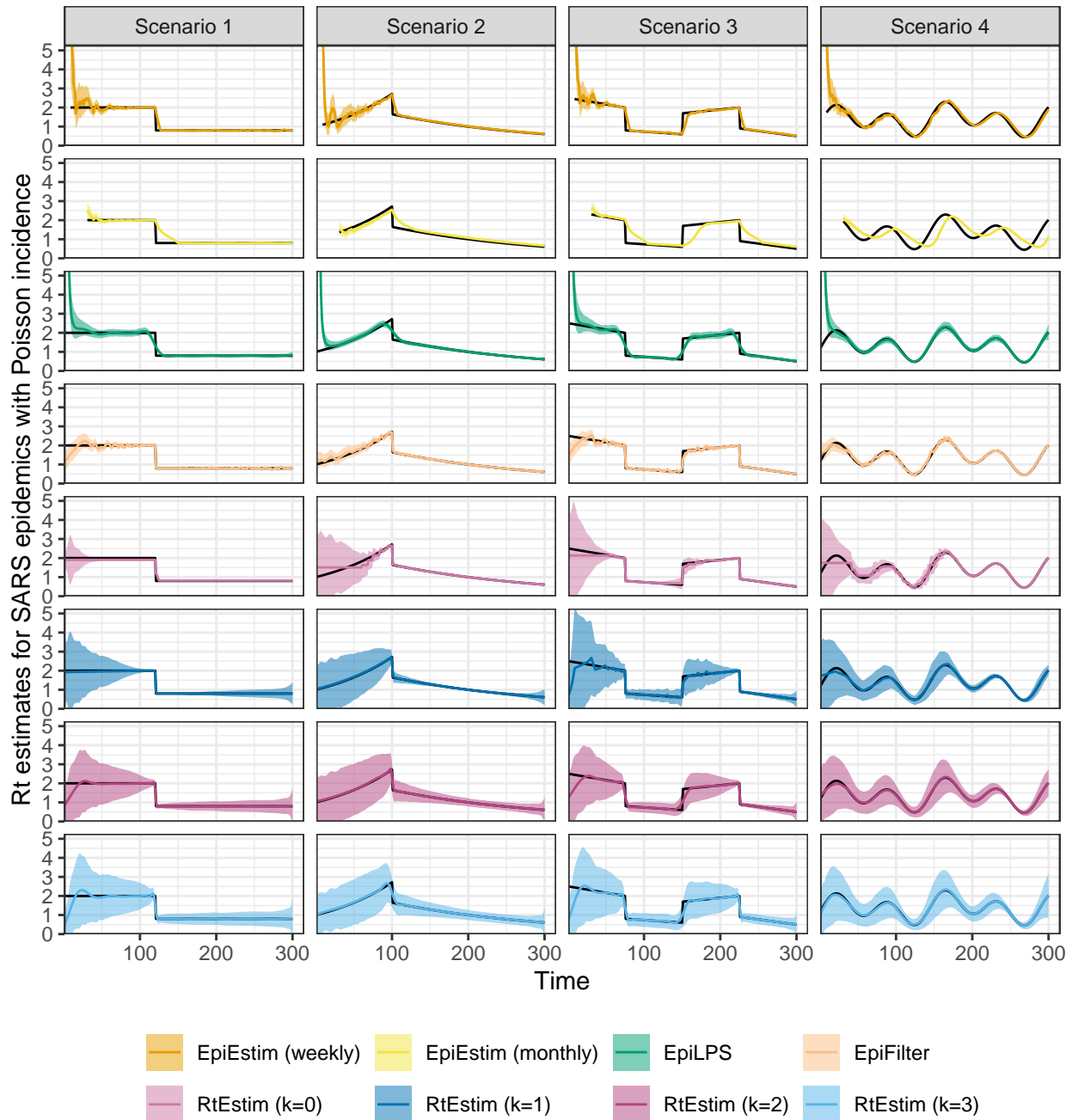


Figure A.6.3: Example SARS epidemics with Poisson incidence. Y-axes beyond 5 are truncated for a better illustration of small values.

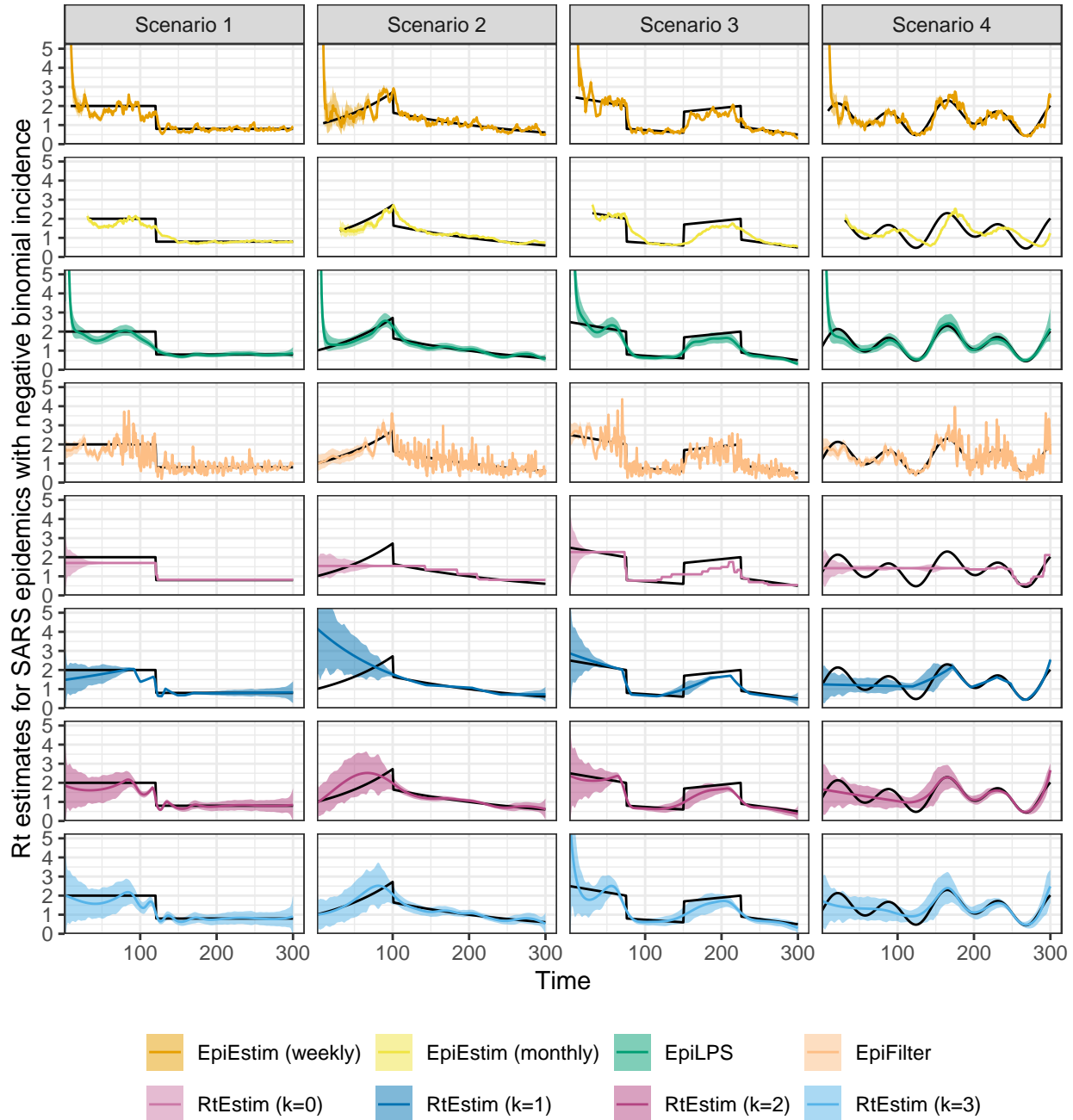


Figure A.6.4: Example SARS epidemics with negative binomial incidence. Y-axes beyond 5 are truncated for a better illustration of small values.

Table 2: Summary of experimental setting on coverage of confidence intervals

Length	SI	Rt scenario	Incidence	SI for modelling	Method
300	measles		3	Poisson, NB	measles 8 methods
300	SARS		3	Poisson, NB	SARS 8 methods

A.6.2 Experimental settings for coverage comparisons of confidence intervals

We focus on a specific \mathcal{R}_t scenario, the piecewise linear case, and only long epidemics to compare the coverage of 95% confidence intervals across all 8 methods. We use the true serial interval distributions, those used to generate the synthetic epidemics, in this case. Table 2 summarizes the experimental settings. For each setting, we generate 50 random synthetic epidemics.

We measure the coverage of 95% confidence intervals using three metrics:

1. percentage of coverage per coordinate (if available) across all synthetic data,
2. percentage of overall coverage for all available coordinates, and
3. interval score (Bracher et al. 2021) averaged over all available coordinates.

The first metric results in the percentage of coverage (across the 50 replicates) at each time point for each setting and method. In some cases, this is not available for every time point, for example, **EpiEstim** with weekly sliding window does not provide estimates for the first week. The second metric aggregates across all time and replications. The third metric, interval score (Bracher et al. 2021), is defined as

$$\text{IS}_\alpha(\mathcal{R}, u, l) = \frac{1}{n} \sum_{t=1}^n (u_t - l_t) + \frac{2}{\alpha} (l_t - \mathcal{R}_t) \mathbf{1}_{(\mathcal{R}_t < l_t)} + \frac{2}{\alpha} (\mathcal{R}_t - u_t) \mathbf{1}_{(\mathcal{R}_t > u_t)},$$

where $\alpha = 0.05$ is the significance level, l, u are the lower and upper bounds and $\mathbf{1}_X$ is the indicator function of the condition X . A confidence band that covers the true values more frequently with shorter interval widths will have a lower interval score.

A.6.3 Experimental results on interval coverage comparison

Figures A.6.5 and A.6.6 displays the percentages of coverage of 95% CI per coordinate over 50 random samples for **measles** and **SARS** epidemics respectively. Low Poisson incidence is the easiest for all methods, with coverage near 100% at most timepoints and 0 at the change point. Large negative binomial incidence is the hardest: **EpiLPS** does the best here with averaged coverage at all timepoints close to 1. This is consistent with the findings in the accuracy comparison (using KL values) and the illustration of sample epidemics in Figures A.6.1–A.6.4, where **EpiLPS** is the most accurate. **RtEstim** with degrees $k = 1, 2, 3$ has 100% coverage at most timepoints except the changepoints. The exception is the hardest case, where larger degrees tend to have higher percentages of converge at most timepoints. **RtEstim** with $k = 0$ tends to produce overly narrow intervals, leading to lower coverage. **EpiEstim** with weekly sliding windows fails to cover the true \mathcal{R}_t more frequently under negative binomial incidence compared to Poisson, and performs worse for larger incidence. Its point estimates are quite accurate, but since its 95% confidence band is overly narrow, and the estimated curves are quite wiggly, so it often fails to cover the true values. **EpiEstim** with monthly sliding windows has low percentages of interval coverage at more timepoints than other methods, especially under negative binomial noise. This is consistent with the findings in Section A.6.1, where the point estimates miss \mathcal{R}_t value frequently. It also has relatively narrow intervals. **EpiFilter** has lower percentages of coverage under negative binomial incidence than under Poisson incidence, which is consistent to its performance in accuracy of point estimation, and is to be expected given the misspecified data model.

Figures A.6.7 and A.6.8 displays the percent coverage of 95% CI averaged over all timepoints 50 random replications of **measles** and **SARS** epidemics respectively. CIs of **RtEstim** with $k = 1, 2, 3$ have nearly 100% coverage across all timepoints for all random samples except in the hardest problem, where the incidence is large and overdispersed. The coverage of **RtEstim** $k = 0$ is lower than for other degrees, similar to the above. **EpiFilter** has better coverage under Poisson incidence compared to negative binomial incidence. **EpiEstim** with weekly sliding windows has higher coverage compared to monthly windows, while the percent coverage is less than the nominal 95% in most cases. **EpiLPS** is the closest to nominal in most cases, and even in the hardest problem, its empirical coverage is quite accurate.

Figures A.6.9 and A.6.10 display the interval scores of 95% CI averaged over 50 random **measles** and **SARS** epidemics respectively. **RtEstim** always has the lowest or close to the lowest interval scores. For Poisson, **EpiFilter** has the lowest interval scores, and the scores of **RtEstim** are slightly higher. **EpiLPS** has very large interval scores due to its large estimates at the early stage of the epidemic. These large misses (much larger than the true values) are multiplied by $\frac{2}{\alpha}, \alpha = 0.05$ when computing the interval score, resulting in very poor performance on this metric.

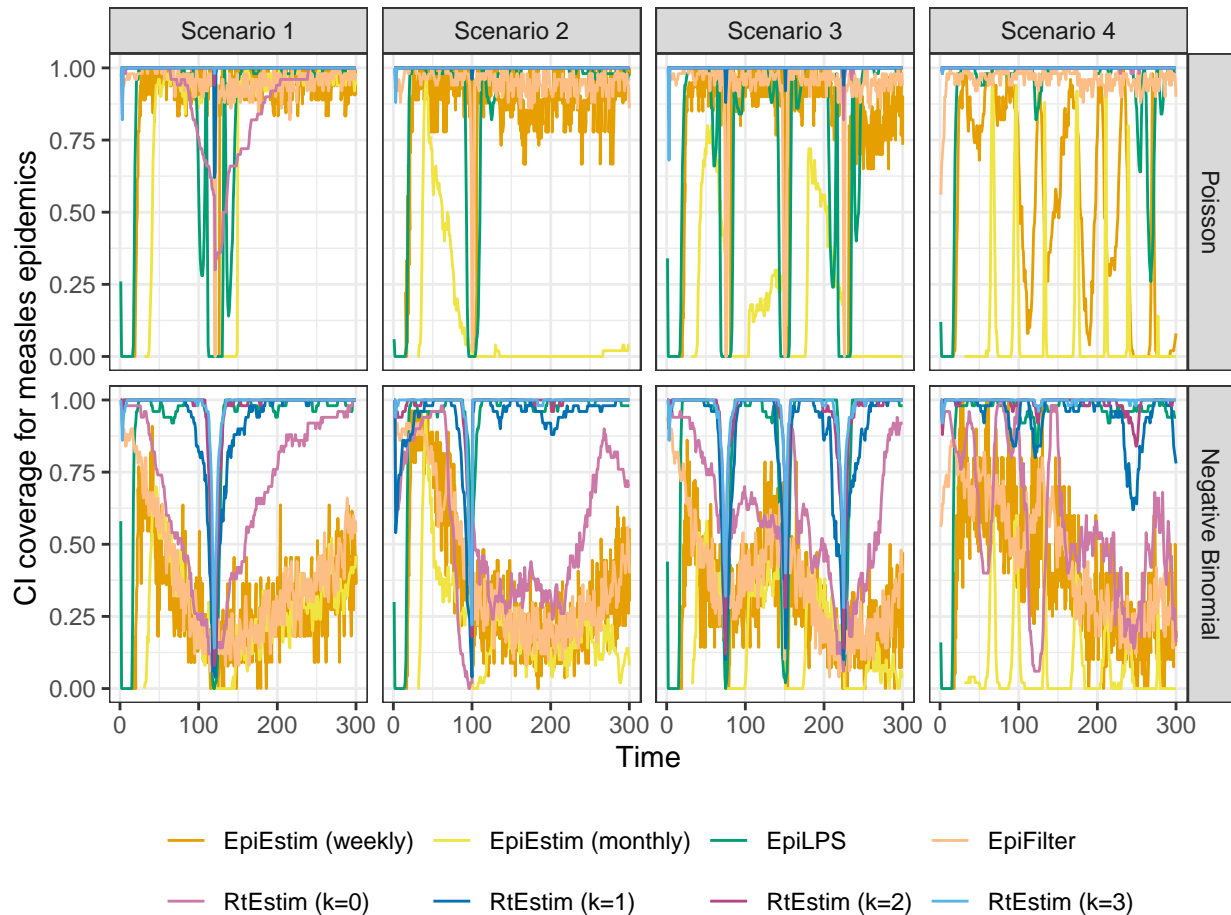


Figure A.6.5: Percent of CI coverage per coordinate across 50 synthetic measles epidemics.

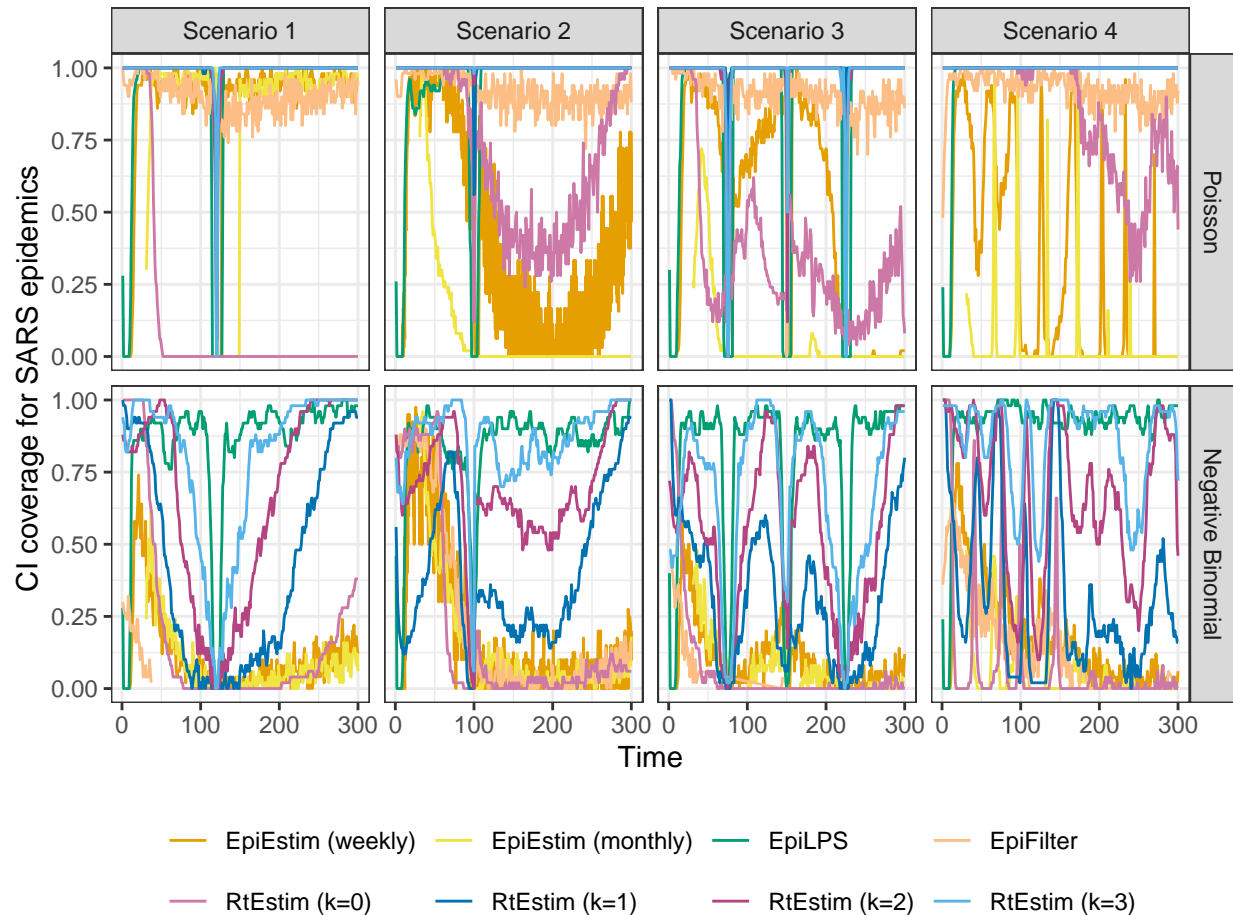


Figure A.6.6: Percent of CI coverage per coordinate across 50 synthetic SARS epidemics.

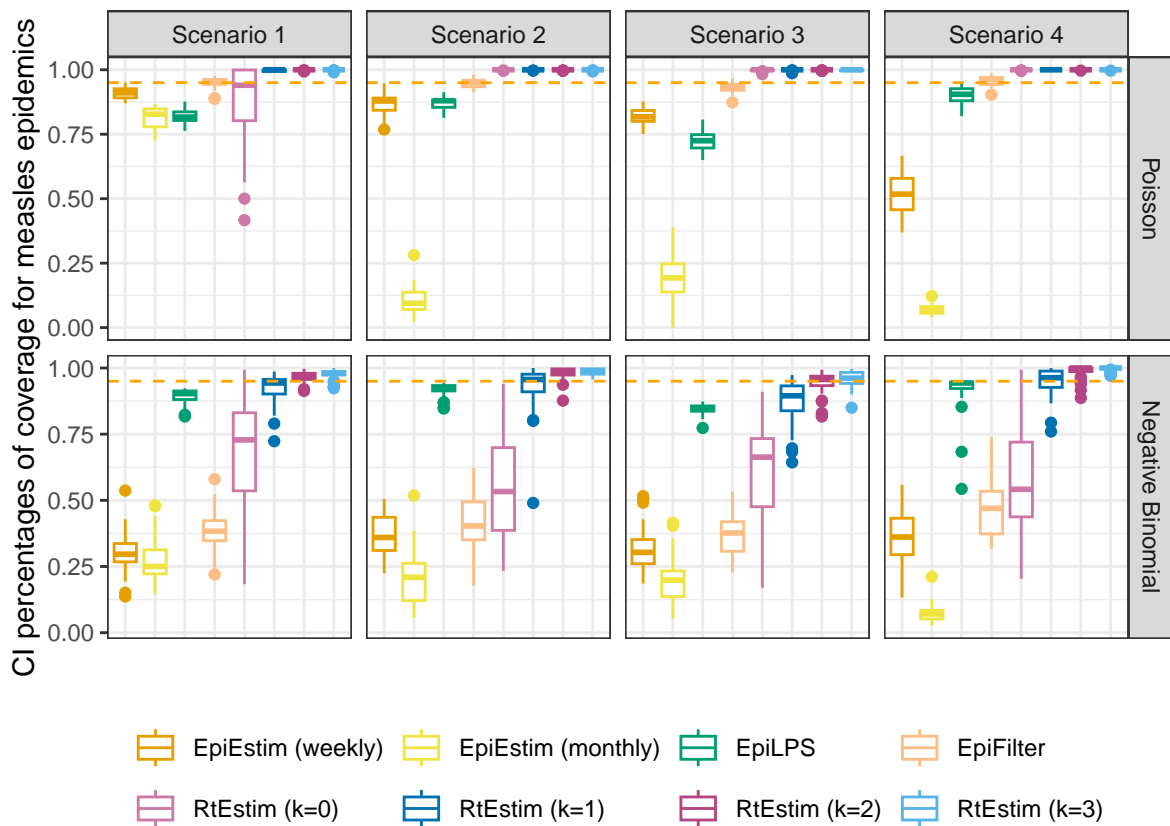


Figure A.6.7: Percentages of CI coverage over all timepoints for 50 synthetic measles epidemics. The orange dashed line represents 95% percentage of coverage across all timepoints.

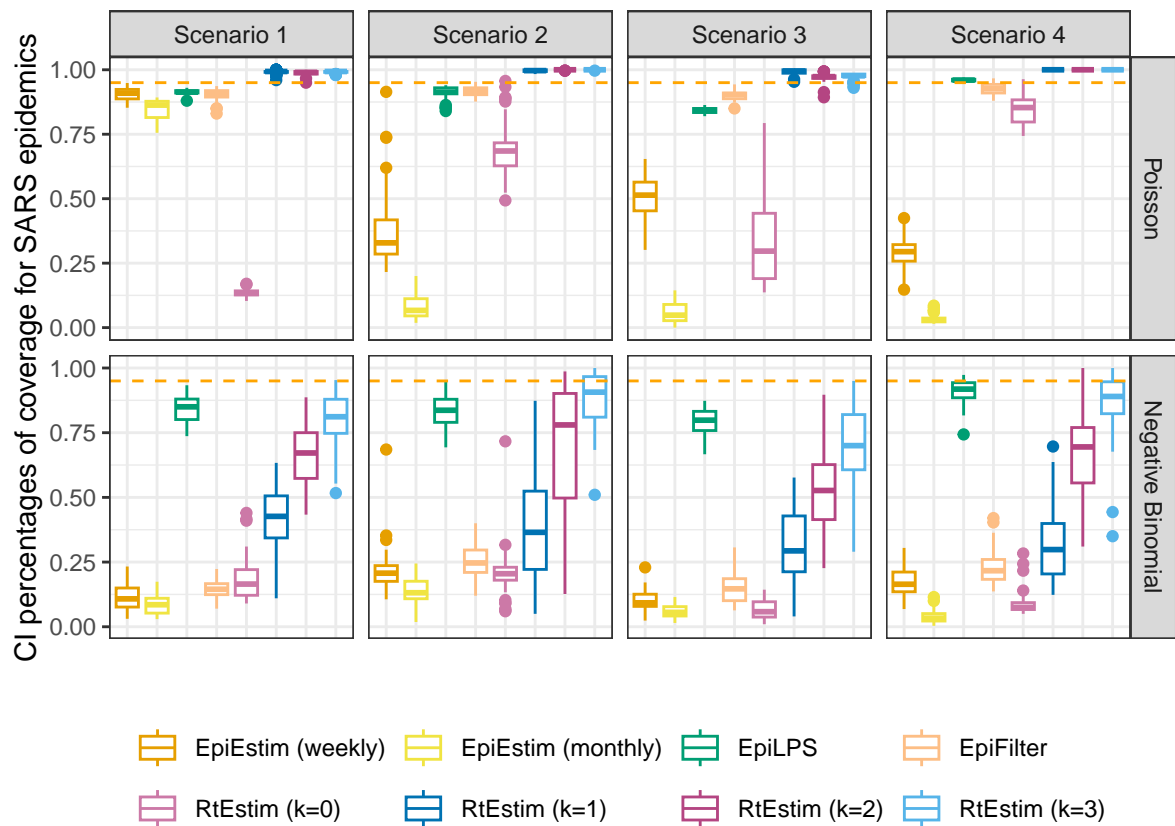


Figure A.6.8: Percentages of CI coverage over all timepoints for 50 synthetic SARS epidemics. The orange dashed line represents 95% percentage of coverage across all timepoints.

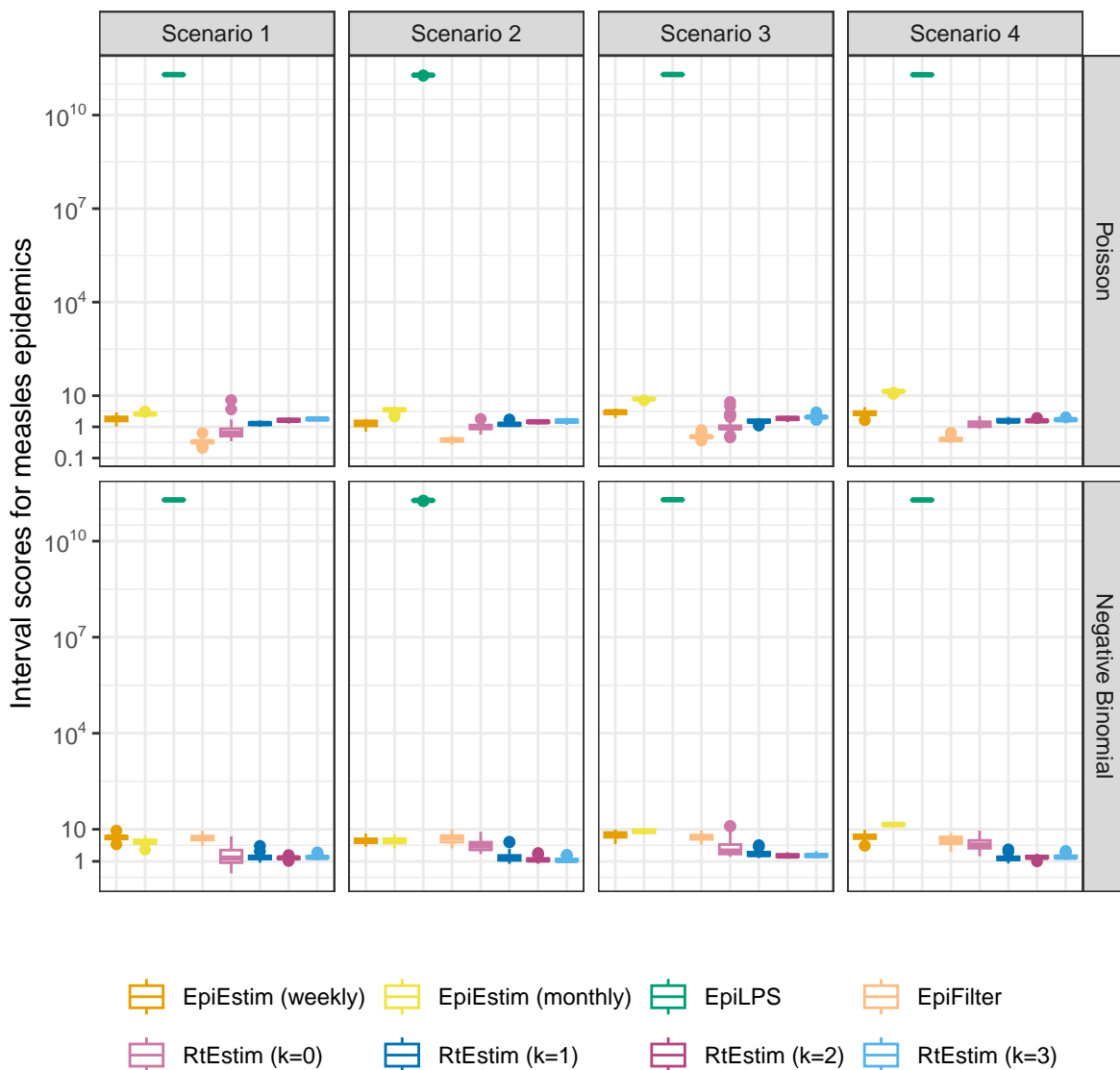


Figure A.6.9: Interval scores averaged over all coordinates for 50 synthetic measles epidemics.

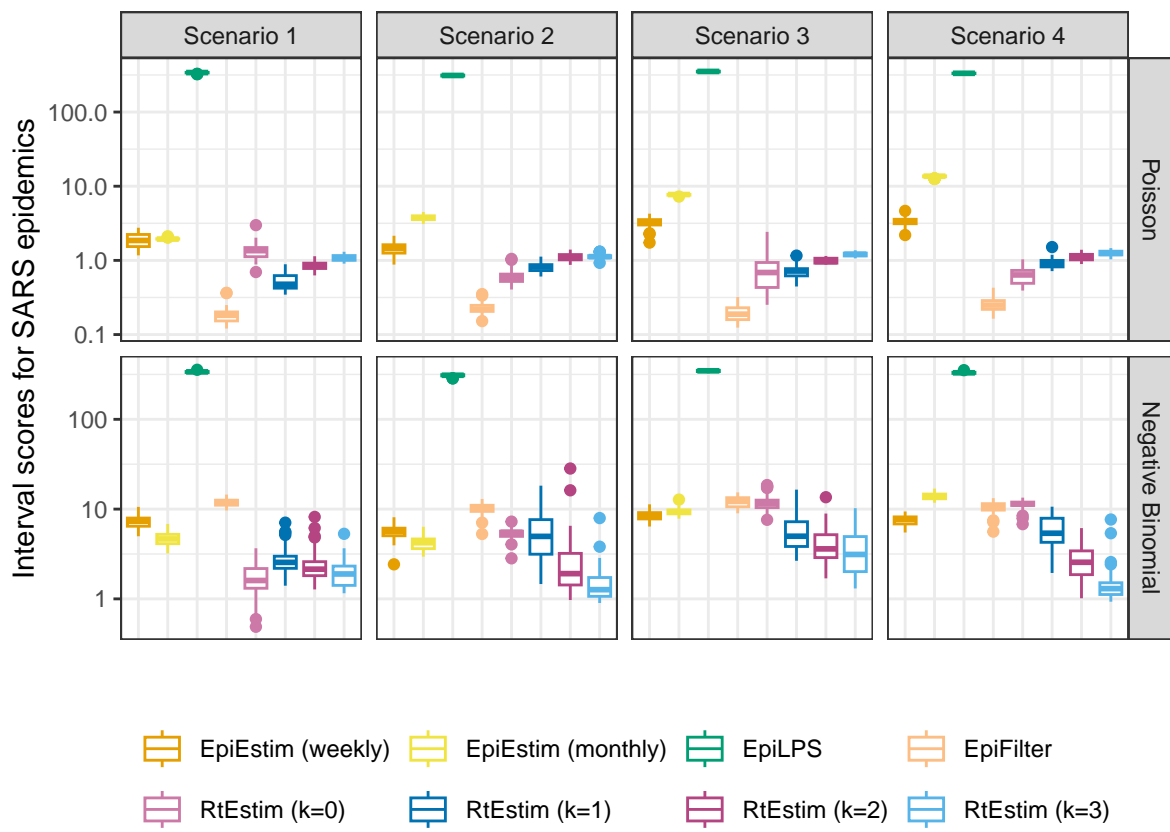


Figure A.6.10: Interval scores averaged over all coordinates for 50 synthetic SARS epidemics.

A.7 Data examples and alternative visualizations of Figs 5 and 6

A.7.1 More visualization of example epidemics

We generate `measles` and `SARS` epidemics using Poisson and negative binomial incidence distributions for each experimental setting. The condensed display of estimates for `measles` with Poisson incidence and `SARS` with negative binomial incidence are provided in Fig 5 and Fig 6 in the manuscript. A full visualization of each case is provided in Section A.6.1. Here, we provide the condensed visualization of the other cases in Figures A.7.1 and A.7.2. All methods provide accurate point estimates given large incidence from the Poisson distribution, while `EpiEstim` (with weekly sliding window) and `EpiFilter` are more wiggly under negative binomial incidence.

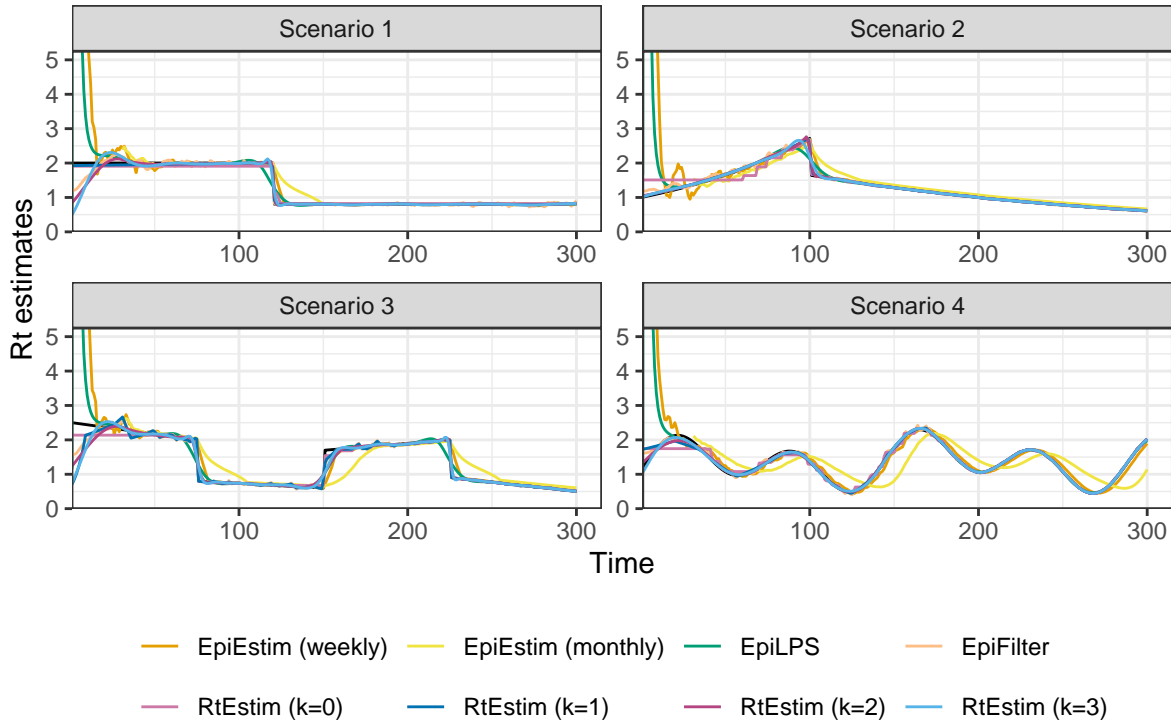


Figure A.7.1: Example of instantaneous reproduction number estimates for SARS epidemics with Poisson observations. Y-axes beyond 5 are truncated for a better illustration of small values.

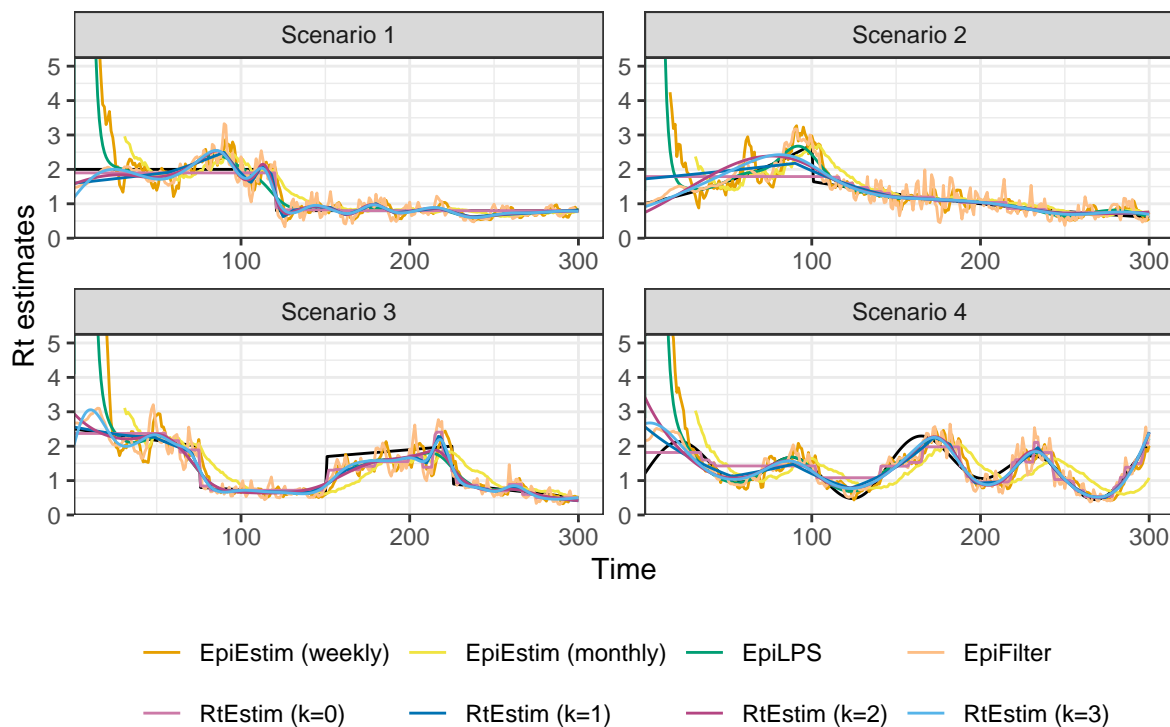


Figure A.7.2: Example of instantaneous reproduction number estimates for measles epidemics with negative binomial observations. Y-axes beyond 5 are truncated for a better illustration of small values.

A.7.2 Alternative view of the difference between fitted and true Rt estimates

We also provide an alternative view of Fig 5 & Fig 6 in the manuscript by plotting $\mathcal{R}_t - \hat{\mathcal{R}}_t$ in Figures A.7.3 and A.7.4 respectively. Figures A.7.5 and A.7.6 provide the alternative view of A.7.1 and A.7.2 respectively. As is to be expected, the difference is largest at the changepoints for most methods. In the sinusoidal periodic scenario, the difference also displays a periodic pattern. This makes sense since \mathcal{R}_t is sinusoidal, while most methods estimate curves to a fixed polynomial degree. Thus higher-order behaviour is missed.

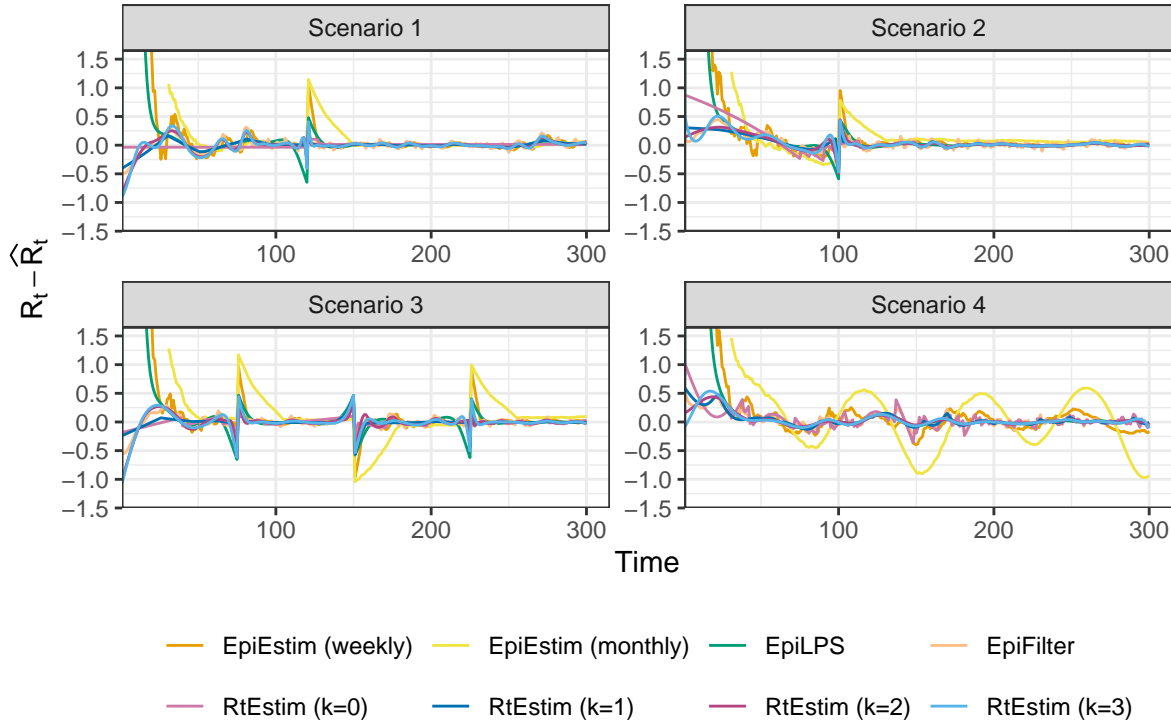


Figure A.7.3: Difference between the true and estimated instantaneous reproduction numbers for measles epidemics with Poisson observations. Y-axes beyond 1.5 are truncated for a better illustration of small values.

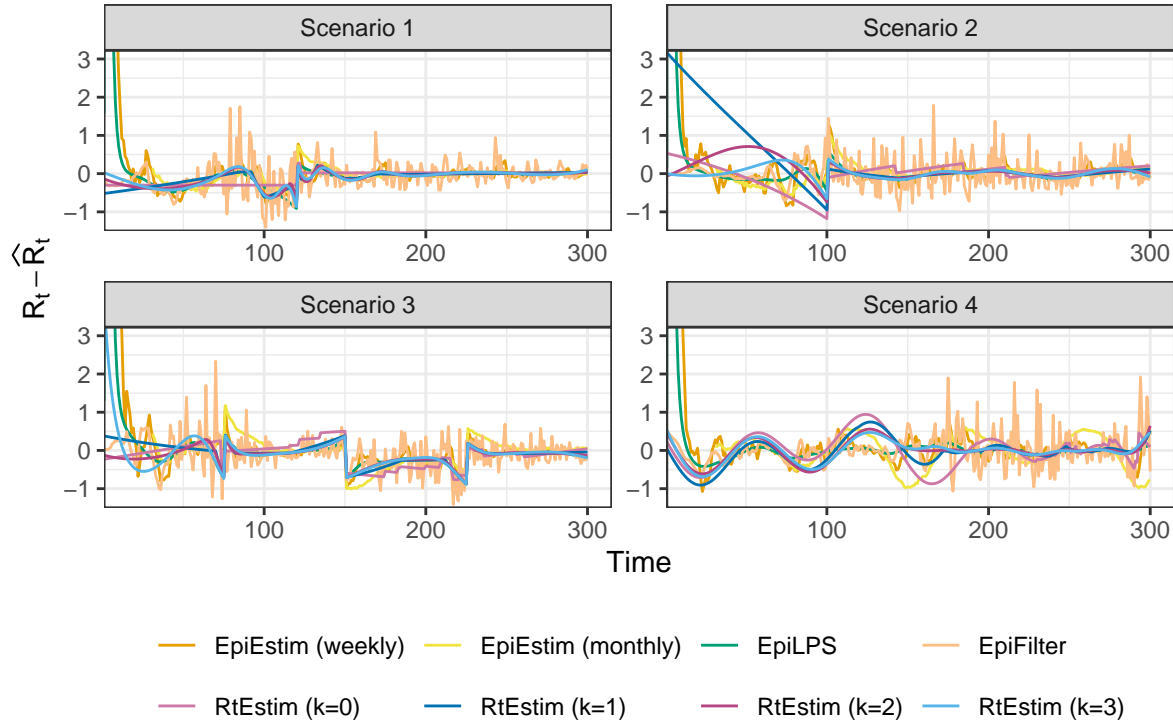


Figure A.7.4: Difference between the true instantaneous reproduction number and its estimation for SARS epidemics with negative binomial observations. Y-axes beyond 3 are truncated for a better illustration of small values.

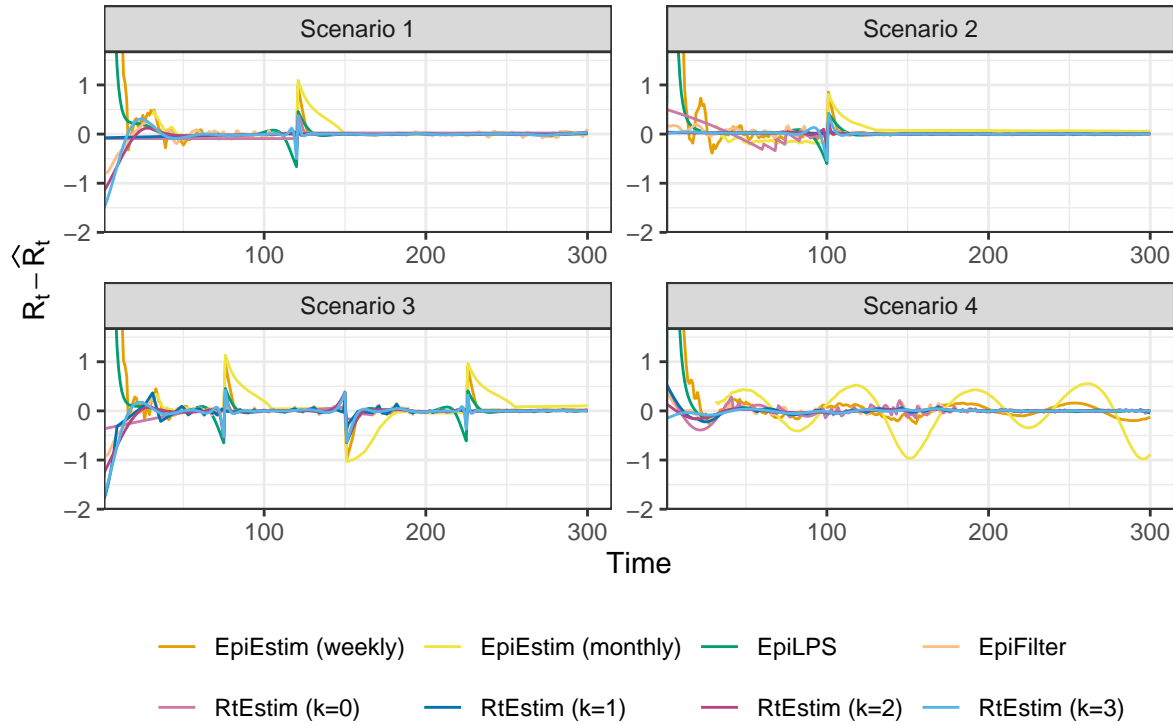


Figure A.7.5: Difference between the true and estimated instantaneous reproduction numbers for SARS epidemics with Poisson observations. Y-axes beyond 1.5 are truncated for a better illustration of small values.

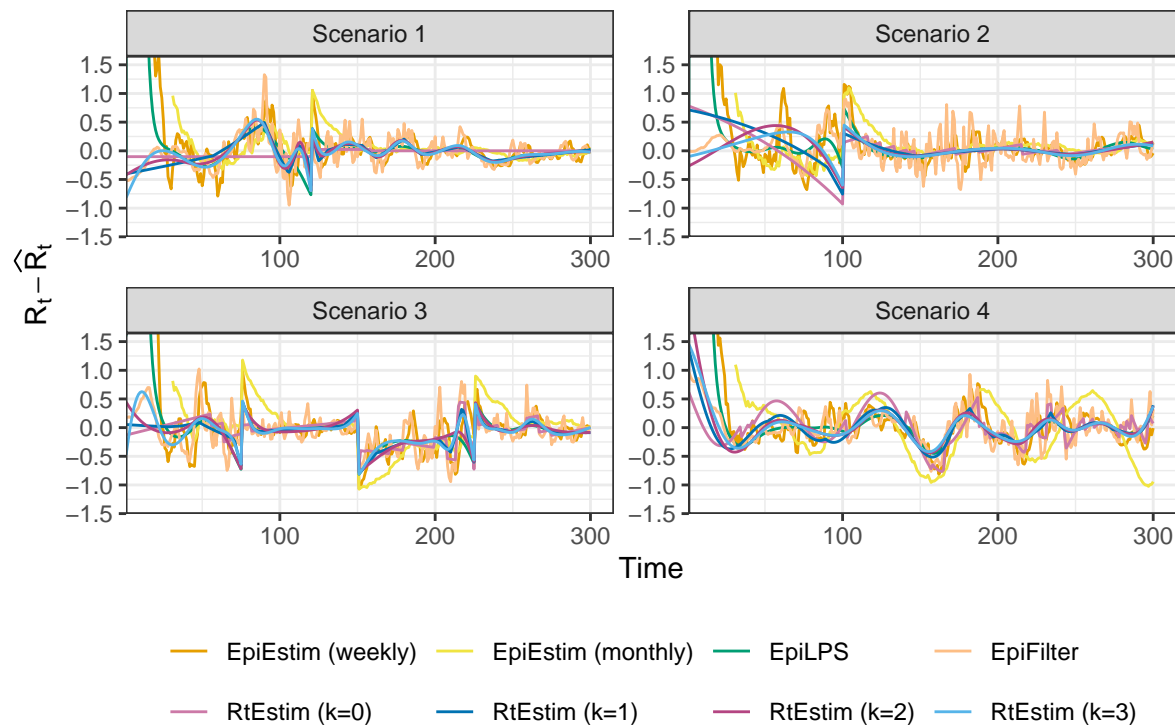


Figure A.7.6: Difference between the true and estimated instantaneous reproduction numbers for measles epidemics with negative binomial observations. Y-axes beyond 1.5 are truncated for a better illustration of small values.

A.8 Application of RtEstim and all competitors on real epidemics

We apply all methods on Covid19 incidence in Canada, and the estimates are displayed in A.8.1. An alternative display which plots all estimated curves in one panel for an easier comparison is provided in A.8.2. All methods provide similar \hat{R}_t curves beyond the early stage. Many methods, including **RtEstim** ($k = 1, 2$), **EpiLPS**, and **EpiEstim** (weekly sliding window), all have large estimates (larger than 3) at the early stage of the epidemic. **EpiFilter** is much more wiggly than other estimates. All methods agree that the instantaneous reproduction number of Covid19 in Canada decreases to below 1 near June 2021 and reaches a small peak afterwards, and then decreases slowly until an outbreak at the end of 2021.

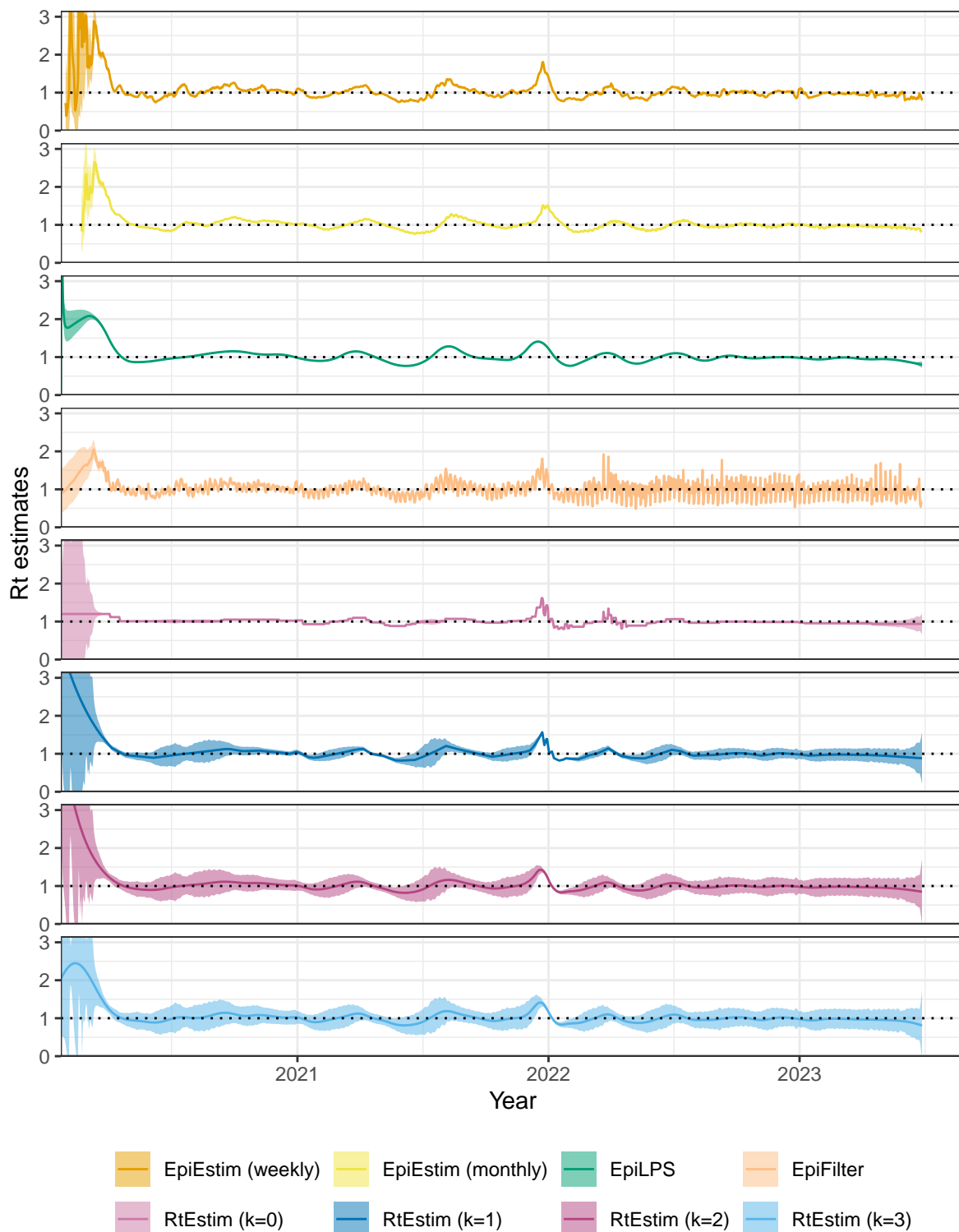


Figure A.8.1: Rt estimates with CIs for Covid19. Y-axes are truncated beyond 3 for a better display of the fluctuation in small values.

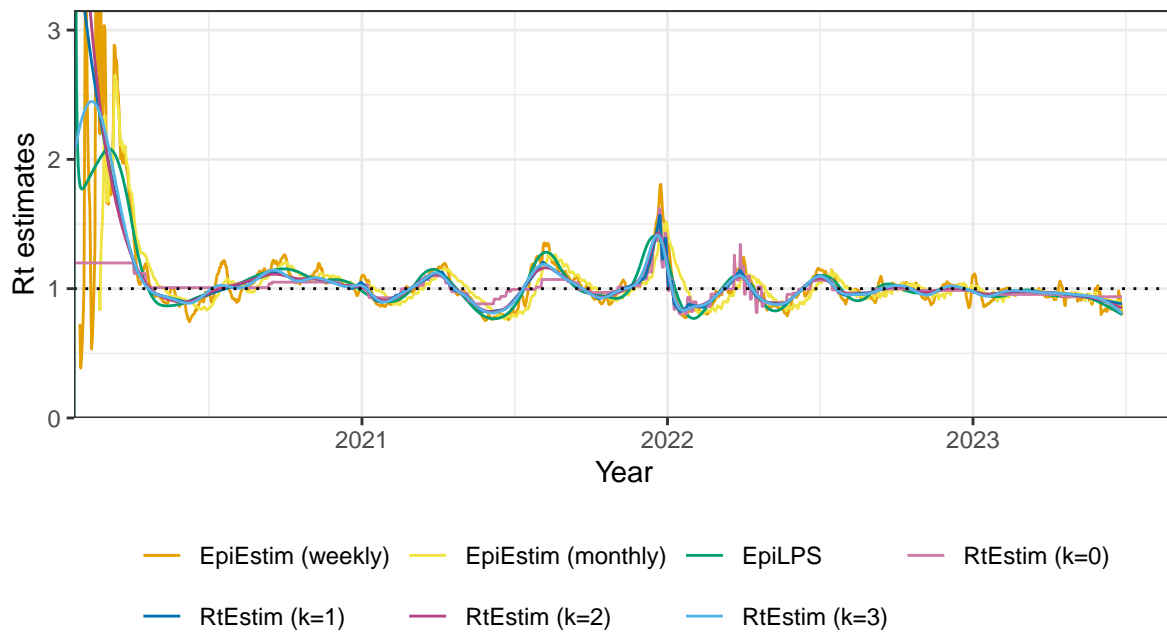


Figure A.8.2: Rt estimates for Covid19. Y-axis beyond 3 is truncated for a better display of the fluctuation in small values. EpiFilter is excluded here, because its estimates are too wiggly and make the plot less readable.

We also apply all methods on Flu in 1918. The results are visualized in Figures A.8.3 and A.8.4. `EpiEstim` with weekly sliding windows, `EpiFilter` and `RtEstim` ($k = 0$) capture the peak of \mathcal{R}_t (close to 3) at around day 30 since the start of the epidemic. While `EpiEstim` with monthly sliding windows, `EpiLPS`, `RtEstim` ($k = 2, 3$) captures the increase around day 30, but have smaller estimates otherwise. Most methods agree that after day 50, the instantaneous reproduction number decreases to, and remains below, 1.

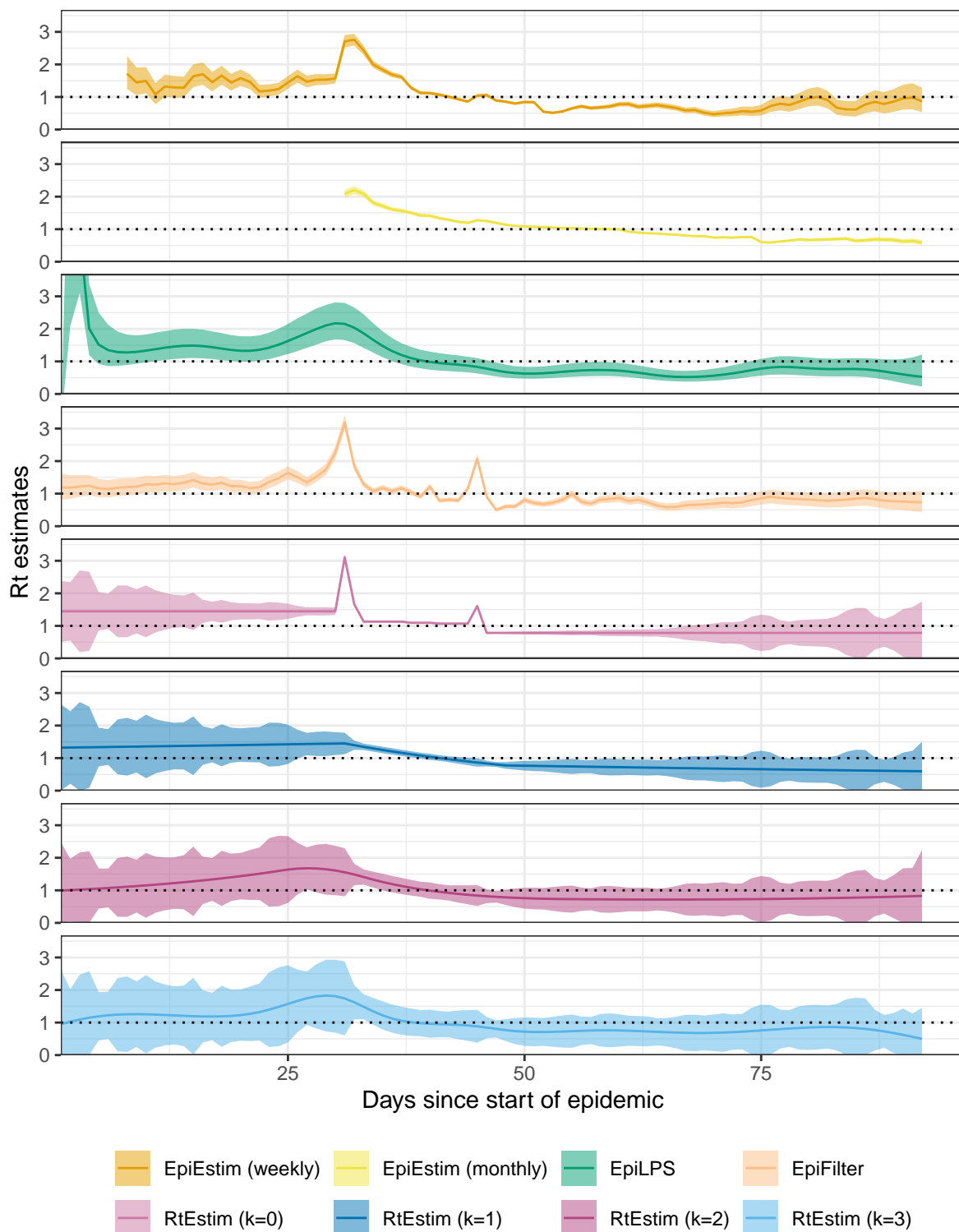


Figure A.8.3: Rt estimates with CIs for Flu 1918. Y-axes are truncated beyond 3.5 for a better display of the fluctuation in small values.

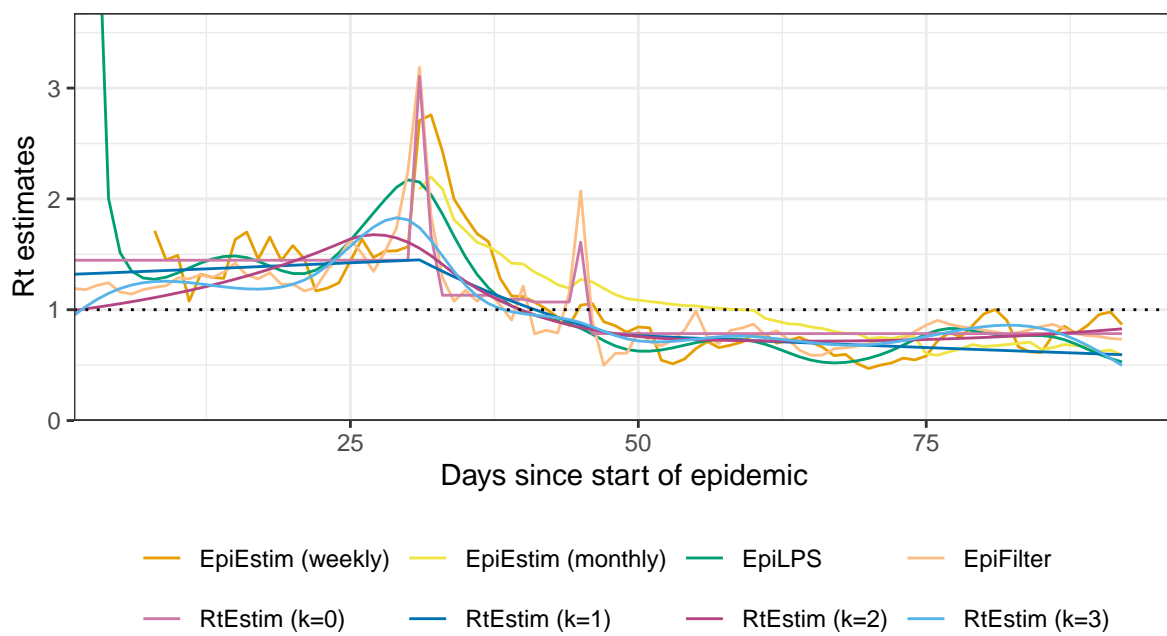


Figure A.8.4: Rt estimates for Flu 1918. Y-axis beyond 3.5 is truncated for a better display of the fluctuation in small values.

References

- Boëlle, Pierre-Yves, Severine Ansart, Anne Cori, and Alain-Jacques Valleron. 2011. “Transmission Parameters of the A/H1N1 (2009) Influenza Virus Pandemic: A Review.” *Influenza and Other Respiratory Viruses* 5 (5): 306–16.
- Bracher, Johannes, Evan L. Ray, Tilmann Gneiting, and Nicholas G. Reich. 2021. “Evaluating Epidemic Forecasts in an Interval Format.” Edited by Virginia E. Pitzer. *PLoS Computational Biology* 17 (2): e1008618. <https://doi.org/10.1371/journal.pcbi.1008618>.
- Cori, Anne, Neil M Ferguson, Christophe Fraser, and Simon Cauchemez. 2013. “A New Framework and Software to Estimate Time-Varying Reproduction Numbers During Epidemics.” *American Journal of Epidemiology* 178 (9): 1505–12.
- Ferguson, Neil M, Derek AT Cummings, Simon Cauchemez, Christophe Fraser, Steven Riley, Aronrag Meeyai, Sopon Iamsirithaworn, and Donald S Burke. 2005. “Strategies for Containing an Emerging Influenza Pandemic in Southeast Asia.” *Nature* 437 (7056): 209–14.
- Groendyke, Chris, David Welch, and David R Hunter. 2011. “Bayesian Inference for Contact Networks Given Epidemic Data.” *Scandinavian Journal of Statistics* 38 (3): 600–616.
- Lipsitch, Marc, Ted Cohen, Ben Cooper, James M Robins, Stefan Ma, Lyn James, Gowri Gopalakrishna, et al. 2003. “Transmission Dynamics and Control of Severe Acute Respiratory Syndrome.” *Science* 300 (5627): 1966–70.
- Wainwright, Martin J., and Michael I. Jordan. 2008. “Graphical Models, Exponential Families, and Variational Inference.” *Foundations and Trends in Machine Learning* 1 (1–2): 1–305. <https://doi.org/10.1561/2200000001>.